UNIVERSITÀ DEGLI STUDI DI PADOVA

Dipartimento di Ingegneria Industriale DII

Corso di Laurea Magistrale in Ingegneria dell'Energia Elettrica

New sensor design and characterisation for electromagnetic tracking in image-guided interventions

Relatore: Dr. Paolo Bettini
Supervisor: Dr. Padraig Cantillon-Murphy

Studente: Marco Cavaliere
matricola 1179780

Anno Accademico 2018/2019

Abstract

As the importance and prevalence of electromagnetic tracking (EMT) in medical and industrial applications increase, the need for customised sensor design has escalated. The thesis focuses on the study of magnetic tracking sensors, where off-the-shelf inductive sensors may not be optimal for many medical instrument tracking applications.

A repeatable approach for the design, optimisation and implementation of air-core and ferrite-core inductive sensors is presented.

Coil-based sensors were designed and tested in order to investigate the effect of the usual coil parameters – such as turn count, geometry and core material – on frequency response and sensor tracking accuracy and precision. The characterisation over frequency was performed with a custom Helmholtz coil. The use of the sensors for EMT was experimentally validated using the Anser EMT system.

Experimental performance was compared to commercial sensors. Static tracking errors of less than 2 mm were achieved and close correlation with theoretical design sensitivity was observed. As expected, errors are decreased by the use of sensors with increased sensitivities.

A first investigation for integration of magnetoresistive sensors in Anser EMT is presented. The basic AMR effect is explained and the main configurations that allow stabilisation and linearisation of AMR sensors are described.

Experimental work on AMR sensors corresponded with theoretical predictions, confirming the constant manufacturer-declared sensitivity at the frequencies of interest for Anser EMT.

Future work might look to overcome the main difficulties that prevent AMR sensors from being efficiently implemented in 3D magnetic tracking systems, such as the need for active supplies and the presence cross-field errors.

Sommario

Sistemi di localizzazione tramite campi elettromagnetici, o *electromagnetic tracking* (EMT) in inglese, trovano importanti applicazioni in ambiti sia medici che industriali. La tesi si concentra sullo studio e lo sviluppo di sensori magnetici per utilizzo in sistemi EMT.

Sensori magnetici ad induzione, basati su semplici avvolgimenti di filo di rame, sono stati progettati e realizzati, allo scopo di dimostrare la validità di elementari formule analitiche, che tuttavia si sono rivelate molto accurate e utili.

È stato studiato e viene presentato l'effetto dei principali parametri di un sensore ad induzione, come il numero degli avvolgimenti, la dimensione dell'area e il materiale del nucleo, che può essere in aria o in materiale ferromagnetico. Una bobina di Helmholtz è stata progettata e costruita per poter misurare la risposta in frequenza dei sensori studiati.

Un test di accuratezza del tracciamento della posizione è stato effettuato grazie ad Anser EMT, un progetto open-source che realizza un prototipo di sistema EMT. La performance è stata confrontata con i risultati forniti da sensori commerciali. Sono stati ottenuti errori di posizionamento statico minori di 2 mm.

Le misure sulla sensibilità hanno evidenziato una grossa corrispondenza con i valori supposti, dimostrando la validità del metodo utilizzato, che può risultare utile nel progetto di sensori da utilizzare in applicazioni specifiche.

Viene inoltre presentato un primo studio sull'utilizzo di sensori a magnetoresistenza come sonde per sistemi EMT. Sono esposti i concetti teorici e le tecnologie alla base del funzionamento di tali sensori e le principali problematiche da risolvere per una corretta implementazione in sistemi di localizzazione tridimensionale.

Sulla base dello stato dell'arte dei sistemi EMT e alla luce dei miglioramenti necessari per rendere questa tecnologia precisa ed affidabile, nell'ultimo capitolo vengono suggeriti alcuni possibili argomenti su cui fare ricerca in futuro.

Acknowledgements

I wish to thank everyone who have helped and contributed to my work.

I would like to thank my supervisor, Dr. Padraig Cantillon-Murphy for all the guidance and support he has provided. I would also like to thank Dr. Herman Alexander Jaeger who has been available to help me with explanations and advices, always ready to share his knowledge. I'm deeply grateful to Tim Fass who helped me in many situations.

A big thank you goes to Mick and Tim of the Mechanical Workshop for their assistance in constructing the mechanical components that I needed.

I would like to thank Manish, Aleksandr, Kilian and Danny, which have been working with me at the design of a new magnetic sensor.

My special thanks to all the members of the lab: Carlo, Emanuela, Miguel, Charu, Philip, Stephen, Rob, Jacopo, Jack, George, Brian, Mark and Sergi. Tea breaks and card games with you contributed to create a pleasant environment where to work and study.

I am very grateful to my friends from Italy for being always present, even if from a long distance, through messages and video-calls which kept us updated. Thanks also to Andrea, Francesco, Fabio and Daniele for the long calls and discussions we had together.

I wish to thank my family and parents for all their support and encouragement throughout my studies. Finally, I thank Giulia for her patience and motivation and for being always ready to help and advice me.

Many thanks to everyone.

Contents

List of Figures

List of Tables

Chapter 1

Introduction

This chapter wants to give an overview of the work presented in this thesis.

Computer-assisted interventions and image-guided interventions are introduced, with particular attention to electromagnetic tracking (EMT) systems.

The open-source project Anser EMT is presented and the main processes and technologies involved in the tracking procedure are explained. It is interesting to understand how the general concepts behind EMT are implemented in practice, to obtain a fully working research-level tracking system.

The last part of the chapter exposes the main problems that the thesis wants to address, the objectives, the work accomplished to reach them and the main results achieved.

Finally, a brief summary of the thesis structure and the chapters content is given.

1.1 Instrument tracking in image-guided interventions

Computer-assisted interventions refer to all those practices and methodologies that make use of computer-based tools to support medical interventions. Within this wide field are image-guided interventions [1][2], where the tracking of medical instruments, in conjunction with preoperative or intraoperative images, provides a navigation during to the procedure.

Modern image-guided interventions have been the subject of an increasing interest over the last decades. By providing novel alternative means of visualisation, they allow greater control of the procedure and real-time feedback on the effect of the intervention. The main benefits of the minimised invasiveness are the reduction of tissue trauma and faster recovery time.

The typical steps for image-guided interventions are: (1) the acquisition of preoperative images, (2) the registration of the patient anatomy to the acquired images and (3) the localisation and visualisation of the instrument on the image relative to the patient anatomy. The physician uses the virtual display to manipulate the instruments and all the images are available as postoperative data.

The tracking system, or localiser, is the essential component of any image-guided intervention procedure. There are three main types of tracking systems: optical videometric systems, active and passive optical/infrared systems, electromagnetic systems.

Videometric optical systems use one or more video cameras to detect and identify marker patterns, *e.g.* a chequered pattern on the instrument surface. An example of commercially available system is the MicronTracker (*Claron Technology Inc., Toronto, Canada*).

In optical active infrared systems, the markers emit near-infrared light, which is received by two or three linear units that form the camera module. In passive infrared systems, the markers reflect the infrared light emitted by illuminators mounted in the camera, and their position is recognised with a principle similar to videometric systems. The Polaris System (*Northern Digital Inc., Waterloo, Canada*) combines both the active and passive infrared approaches in a single optical tracking system.

The main limitation with optical systems is the requirement of rigid instruments and the necessity for the markers to be within line of sight of the tracking camera. This prevents optical systems from being efficiently used in crowded operating theatres and with those kinds of interventions that make use of flexible instruments, such as bronchoscopy.

Electromagnetic tracking (EMT) is the gold standard technology for tracking and navigation in image-guided interventions, when there is no line of sight to the target. Clinical applications which currently exploit EMT for virtual navigation include bronchoscopy [3][4], neurosurgery [5] and ear, nose and throat surgery [6]. Commercial systems that use EMT for navigation include the Medtronic superDimension [7], the Veran SPiN system [8] and the Fiagon system [9]. EMT is also increasingly common in visualisation systems used for surgical simulation and robotic surgery. A number of OEM EMT systems that have been developed are suitable for third-party use and research purposes. These include the NDI Aurora (*Northern Digital Inc., —*), the NDI Trakstar (*Northern Digital Inc., —*, formerly sold by *Ascension Technologies, St. Louis, Missouri*) and the Polhemus Fastrak (*Polhemus Inc., Colchester, Vermont*).

1.2 Electromagnetic Tracking

In general, an EMT system relies on two main components: a field generator, which generates a space dependant field, and a magnetic sensor, which, by field measurement, can determine its relative position and orientation with respect to the field generator. One of the two components is fixed (at known position), while the other needs to be tracked (the position is unknown). The following discussion will consider the case of a static field generator and a moving sensor, attached to the object to be tracked. The opposite case, with a field generator at an unknown position and a set of magnetic sensors at fixed positions, would also be possible.

The magnetic field at a general point (x, y, z) of the space is a vector with three components:

$$\mathbf{B}(x, y, z) = [B_x(x, y, z) \quad B_y(x, y, z) \quad B_z(x, y, z)] \tag{1.1}$$

The orientation of the magnetic sensor is identified by the unit vector $\mathbf{n}$:

$$\mathbf{n} = \mathbf{n}(\theta, \varphi) \tag{1.2}$$

where θ and φ are the pitch and the yaw angle respectively, as defined in Figure 1.1 for a

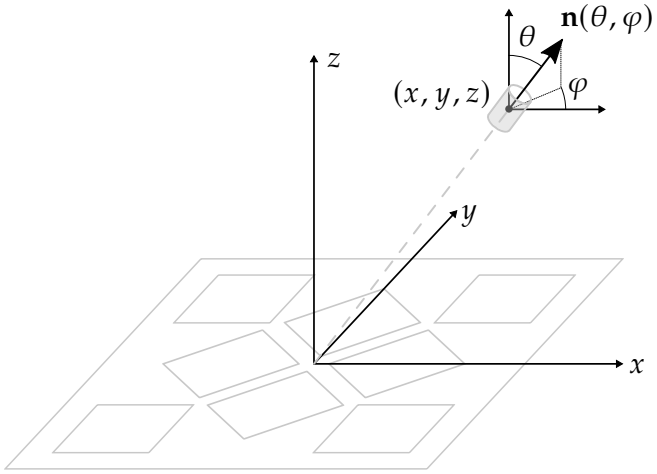

Figure 1.1: Reference system of coordinates adopted in the dissertation. The position is identified by x, y and z. The orientation is given by the unit vector $\mathbf{n}$, defined by the angles θ and φ in a spherical coordinate system. The shadowed cylinder and board represent a magnetic sensor and the field generator of Anser EMT (see paragraph 1.3.1).

spherical coordinate system.

If the sensor area is small, $\mathbf{B}$ can be assumed to not vary within the volume occupied by the sensor. Then, the voltage measurement, v_s, depends on the field at the sensor position and on the orientation of the sensor:

$$v_s = f(\mathbf{B}, \mathbf{n}) = f(x, y, z, \theta, \varphi) \tag{1.3}$$

The five unknowns of Equation 1.3 give the relative position and orientation between the field generator and the sensor.

To determine the five unknowns $(x, y, z, \theta, \varphi)$, at least five constraints in the form of Equation 1.3 are needed. This can be obtained by the use of multiple field generators, multiple sensors, or both. For example, three sensors at the same position (x, y, z) with three different orientations $\mathbf{n}_1$, $\mathbf{n}_2$ and $\mathbf{n}_3$ give a set of three independent equations:

$$\begin{cases} v_{s1} = f(\mathbf{B}_1, \mathbf{n}_1) = f_1(x, y, z, \theta, \varphi) \\ v_{s2} = f(\mathbf{B}_1, \mathbf{n}_2) = f_2(x, y, z, \theta, \varphi) \\ v_{s3} = f(\mathbf{B}_1, \mathbf{n}_3) = f_3(x, y, z, \theta, \varphi) \end{cases} \tag{1.4}$$

The addition of other orientations $(\mathbf{n}_4, \mathbf{n}_5, \dots)$ would not be independent of $\mathbf{n}_1$, $\mathbf{n}_2$ and $\mathbf{n}_3$. By the use of a second field generator, which generates a different field $\mathbf{B}_2(x, y, z)$, it is possible to have three more independent equations:

$$\begin{cases} v_{s4} = f(\mathbf{B}_2, \mathbf{n}_1) = f_4(x, y, z, \theta, \varphi) \\ v_{s5} = f(\mathbf{B}_2, \mathbf{n}_2) = f_5(x, y, z, \theta, \varphi) \\ v_{s6} = f(\mathbf{B}_2, \mathbf{n}_3) = f_6(x, y, z, \theta, \varphi) \end{cases} \tag{1.5}$$

Another possibility is to use only one magnetic sensor, and five or more field emitters

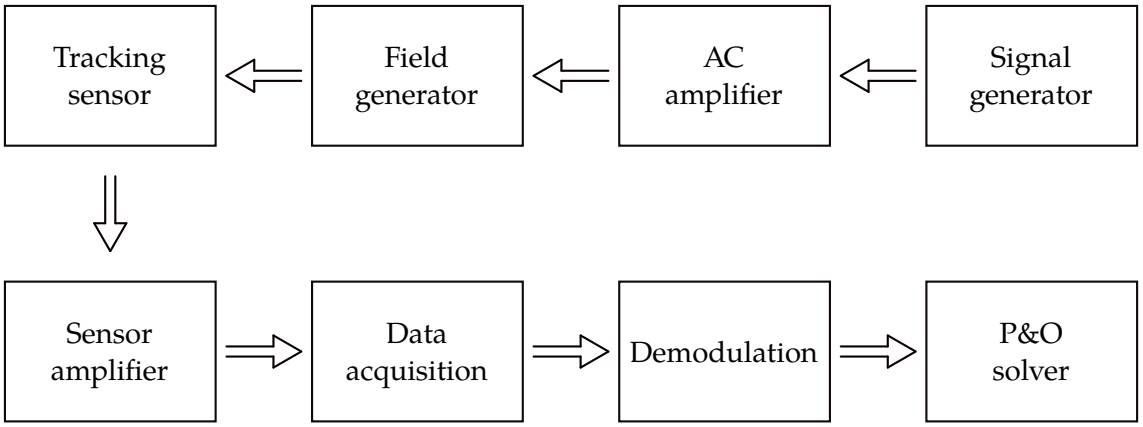

Figure 1.2: Main subsystems involved in the Anser EMT tracking procedure. Signal generators provide 8 reference sine waves to the closed-loop circuits of AC amplifiers, which supply the 8 emitter coils of the field generator. A pick-up coil sensor measures the magnetic field. The induced voltage is then amplified, sampled and demodulated. The amplitudes of the 8 fields are finally processed to obtain the position and orientation of the sensor.

with different positions and/or orientations. Since the sensor measures the total magnetic field, it is essential to distinguish the signal (v_{s1}, v_{s2}, ...) related to each emitter coil. This can be accomplished by transmitting subsequently one field at a time, or by the use of amplitude or frequency modulation. Typical is the case of each field transmitted at a specific frequency, with demodulation that consists in the Fourier analysis of the measured signal. Both the methods add latency to the system, due to the time needed to subsequently receive each signal in the first case and because of the integration involved in the Fourier analysis in the second case.

1.3 Anser EMT

Anser EMT is an open-source project that implements EMT [10]. It is developed at University College Cork in collaboration with IHU Strasbourg. The name of the system is inspired by the goose *Anser anser* [11], which uses the Earth magnetic field for navigation during its annual migration. While commercial tracking systems do not disclose the physical models and algorithms used (closed-source), the aim of Anser EMT project is to create an EMT platform for research and development use. All the design files are provided in the official Open Science Framework webpage [12] and the latest codes are available at the git repository of the project [13].

The system is composed of eight main subsystems which accomplish specific tasks of the tracking procedure. Figure 1.2 summarises the operation of the system from the generation of the signal to the measurement and the final solution for position and orientation of the sensor. A brief summary of the role of each subsystem is given below.

- The **signal generator** provides the source signal for the eight emitter coils of the field generator. Each coil is driven at a different frequency, in a range between 20 and

30 kHz. The sinusoidal waveforms are generated by a digital synthesiser (AD9833, *Norwood, Massachusetts*). A micro-controller (Arduino, *Ivrea, Italy*) is used to program the synthesiser.

- The **AC amplifier** increases the power gain of the generated sinusoidal signals and drives the current of the emitter coils to produce a time-varying magnetic field. Closed-loop control is used to achieve long-term stability and to minimise temperature drift and crosstalk interference between the coils.
- The **field generator** is an array of eight emitters coils, each one generating a magnetic field at a specific frequency. The purpose is to create an operating volume where every point and orientation is characterised by a specific set of eight magnetic field values.
- The **tracking sensor** is a coil that produces a time-varying voltage signal when placed in the working volume of the field generator. The signal is a superposition of the eight voltages induced by the time-varying magnetic fields emitted by the field generator.
- The **instrumentation amplifier** circuit conditions the signal before sampling. Typically, the induced sensor voltage has small amplitude (μV) and requires filtering and amplification.
- Once conditioned, the voltage signal is sampled by the **data acquisition** unit (NI-USB 6216 DAQ, *Texas Instruments, Dallas, Texas*). The maximum sampling rate is 400 kHz and Anser EMT currently uses a sampling frequency of 100 kHz. This allows three channels available for sensor signals and a channel dedicated to the emitter coils current acquisition, in order to determine the relative phase of the sensor voltage, as explained in paragraph 1.3.4.
- The tracked sensor signal is the superposition of the eight frequencies of the emitter coils. **Asynchronous demodulation** is needed to extrapolate the signal components and to allow the magnitude and phase of each frequency component to be measured.
- The magnitude and phase information of each frequency component is used by the **position and orientation (P&O) algorithm** to localise the tracking sensor. If the sensor has five degree of freedom (5DOF), the tracking procedure results in a 5-element vector $(x, y, z, \theta, \varphi)$, which comprises the position and orientation information.

In the following sections, some of the above mentioned subsystems are described in more detail, to give an overview of how the general concepts of EMT presented in section 1.2 are realised and implemented in the Anser EMT system.

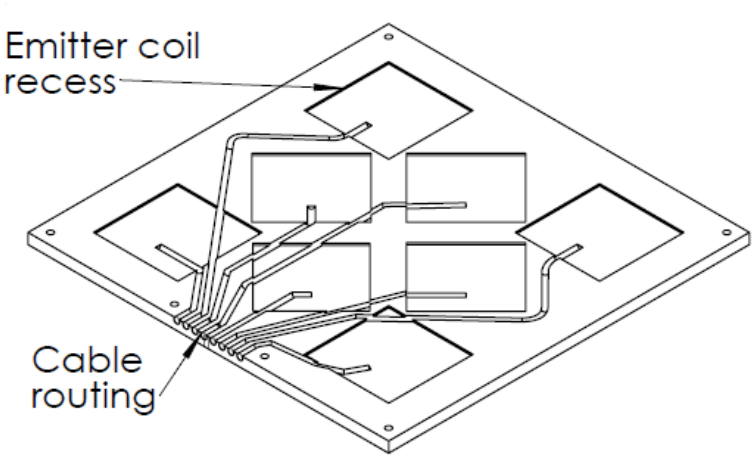

Figure 1.3: Field generator of Anser EMT. The board is composed by eight planar coils. *Image source: [15].*

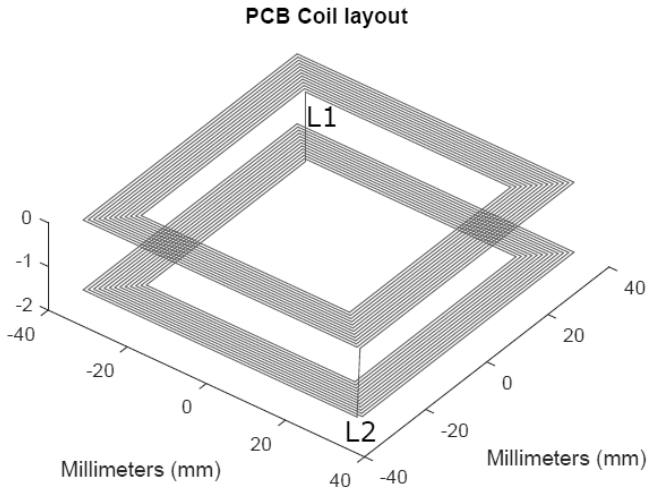

Figure 1.4: Design for a single PCB coil. L1 and L2 denote the PCB vias where the winding switches layer. *Image source: [16].*

1.3.1 Field generator

The field generator is composed of eight planar coils, as shown in Figure 1.3. The use of planar coils for position detection was first demonstrated by Plotkin *et al.* [14]. Each coil is at a known position from the centre of the field generator, has square shape, is PCB printed and contains a total of 25 turns on copper track, divided in 2 layers (Figure 1.4).

Each coil is driven with a sinusoidal current at a different low-frequency (< 100 kHz), usually in the range 20–30 kHz. The generated magnetic field covers a $25 \times 25 \times 25$ cm volume in which a sensor coil may be tracked.

The regular shape of the coils helps in the calculation of the exact magnetic field within the working volume. Each copper track is considered a filamentary conductor and the field that it generates can be analytically calculated by integration of the Biot-Savart law (see paragraph 1.3.2). The total field at every point of the space is given by the superposition of

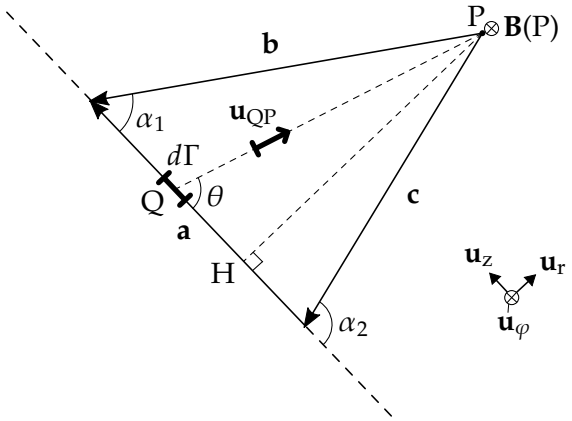

Figure 1.5: Magnetic field **B** due to a straight filament.

the contributions of 800 filaments (= 8 coils × 25 turns × 4 edges).

1.3.2 Magnetic field due to a straight filamentary conductor

For a filamentary current I along the path Γ, the Biot-Savart law, given by Equation 1.6, predicts the magnetic field **B** at any point P of the space, in a linear and homogeneous medium:

$$\mathbf{B}(\mathrm{P}) = \frac{\mu_0}{4\pi} \int_{\mathrm{Q}\in\Gamma} \frac{I\,\mathbf{u}_z \times \mathbf{u}_{\mathrm{QP}}}{\overline{\mathrm{QP}}^2}\, d\Gamma \tag{1.6}$$

where $\mathbf{u}_z$ and $\mathbf{u}_{\mathrm{QP}}$ are the unit vectors pointing in the direction of the current and in the direction $\overrightarrow{\mathrm{QP}}$ respectively.

Consider Γ to be a straight line. H is the projection of P on Γ, θ is the angle between the points $\mathrm{P\hat{Q}H}$, $\mathbf{u}_r$ and $\mathbf{u}_\varphi$ are the unit vectors defined in Figure 1.5. Noting that:

$$\Gamma = \overline{\mathrm{PH}} \frac{1}{\sin\theta} \tag{1.7}$$

$$\mathbf{u}_{\mathrm{QP}} = -\cos\theta\,\mathbf{u}_z + \sin\theta\,\mathbf{u}_r \tag{1.8}$$

$$\overline{\mathrm{QP}} = \overline{\mathrm{PH}} \frac{1}{\sin\theta} \tag{1.9}$$

then:

$$d\Gamma = -\overline{\mathrm{PH}} \frac{1}{\sin^2\theta} d\theta \tag{1.10}$$

$$\mathbf{u}_z \times \mathbf{u}_{\mathrm{QP}} = \sin\theta\,\mathbf{u}_\varphi \tag{1.11}$$

$$\frac{1}{\overline{\mathrm{QP}}^2} = \frac{\sin^2\theta}{\overline{\mathrm{PH}}^2} \tag{1.12}$$

and Equation 1.6 becomes:

$$\mathbf{B}(\mathrm{P}) = \frac{\mu_0 I}{4\pi\overline{\mathrm{PH}}} \int_{\alpha_1}^{\alpha_2} -\sin\theta\,\mathbf{u}_\varphi\, d\theta = \frac{\mu_0 I}{4\pi\overline{\mathrm{PH}}} (\cos\alpha_1 - \cos\alpha_2)\mathbf{u}_\varphi \tag{1.13}$$

The formula of Equation 1.13 is implemented in the code of Anser EMT in a vector form, already used in [17] and firstly proposed by [18]. The vector formulation is of faster computation for vector-based programs such as MATLAB. Moreover, it is of easier implementation because it uses directly the position vectors of the filaments and of the point P. If **a** is the current filament vector, **b** is the vector pointing from P to the end of the filamentary wire and **c** is the vector pointing from P to the start of the filament, the following relations are true:

$$\cos\alpha_1 = \frac{\mathbf{a}\cdot\mathbf{b}}{|\mathbf{a}||\mathbf{b}|}, \qquad \cos\alpha_2 = \frac{\mathbf{a}\cdot\mathbf{c}}{|\mathbf{a}||\mathbf{c}|} \tag{1.14}$$

$$\mathbf{u}_\varphi = \frac{\mathbf{c}\times\mathbf{a}}{|\mathbf{c}\times\mathbf{a}|} \tag{1.15}$$

$$\overline{\mathrm{PH}} = \frac{|\mathbf{c}\times\mathbf{a}|}{|\mathbf{a}|} \tag{1.16}$$

By substitution in Equation 1.13, the vector formulation is obtained:

$$\mathbf{B}(\mathrm{P}) = \frac{\mu_0 I}{4\pi}\frac{\mathbf{c}\times\mathbf{a}}{|\mathbf{c}\times\mathbf{a}|^2}\cdot\left(\frac{\mathbf{a}\cdot\mathbf{b}}{|\mathbf{b}|} - \frac{\mathbf{a}\cdot\mathbf{c}}{|\mathbf{c}|}\right) \tag{1.17}$$

When Equation 1.17 is used in the tracking procedure, the vector **a** is known for each of the 800 filaments composing the coils, while **b** and **c** depend on the position of the sensor and are initially unknown.

1.3.3 Tracking sensor

At present, the sensors implemented for use in Anser EMT are of inductive type. It is not excluded that in the future other possible magnetic sensor technologies will be considered. Chapter 4 will present a first investigation on AMR sensors.

Inductive sensors are based on the principle of electromagnetic induction, described by Faraday's law:

$$v_s(t) = -\frac{d\Phi(t)}{dt} \tag{1.18}$$

where v_s is the induced voltage in Volts and Φ is the sensor magnetic flux in Webers. Figure 1.6 shows the basic concept of a coil-based inductive sensor.

For a cross-sectional area A_c and N turns, Equation 1.18 is more specifically given by Equation 1.19, in terms of magnetic flux density **B** experienced by the sensor:

$$v_s(t) = -N\frac{d}{dt}\oint_{A_c}\mathbf{B}\cdot\mathbf{n}\,dA \tag{1.19}$$

where **n** is the unit vector normal to the coil's cross-sectional area A_c.

In EMT systems, **B** is typically provided by a planar transmitter board and it is spatially and temporally varying, with a number of unique frequency components which can be used to resolve the sensor position and orientation in the working volume around the transmitter board. For small sensors, the variation in flux density across the sensor cross

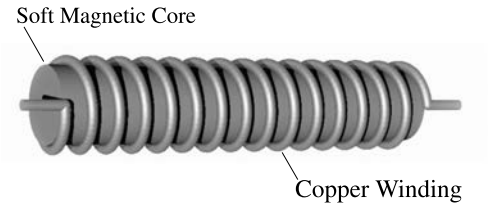

Figure 1.6: The typical electromagnetic inductive sensor consists of a copper winding of N turns. The coil may be air-cored or with a soft magnetic (ferrite) core, as shown here. A time-varying magnetic flux through the turns induces a voltage on the coil.

section is usually small, so that Equation 1.19 may be simplified to Equation 1.20:

$$v_s(t) = -N\frac{d\mathbf{B}}{dt} \cdot \mathbf{n}\, A_c \tag{1.20}$$

If d_i and d_o are the innermost and the outermost winding diameters respectively, A_c is given by Equation 1.21 or, considering the average winding diameter, can be approximated by Equation 1.22:

$$A_c = \frac{1}{d_o - d_i}\int_{d_i}^{d_o} \frac{\pi}{4}x^2\, dx = \frac{\pi}{12}(d_i^2 + d_i d_o + d_o^2) \tag{1.21}$$

$$\simeq \frac{\pi}{4}\left(\frac{d_i + d_o}{2}\right)^2 \tag{1.22}$$

The addition of a ferromagnetic core, as shown in Figure 1.6, can significantly increase the received sensor voltage v_s, particularly in the case of smaller sensor geometries. High-permeability materials tend to concentrate the magnetic flux lines and to increase the B field, resulting in a larger flux through the coil area.

The ferrite core permeability is related to the manufacturer-supplied relative permeability μ_r. It also depends on the geometry of the sensor, because demagnetisation can occur: some magnetic flux lines can find a closed path inside the core itself, which has low reluctance, adding a negative contribution to the flux linked to the coil. The parameter μ_a is defined as apparent magnetic permeability of the core and accounts for the global average increment of the magnetic flux inside the coil.

Ferromagnetic cores can dramatically increase the sensitivity of sensor, but this comes at the cost of linearity. All ferromagnetic materials are inherently non-linear in nature, hence the output of the sensor will exhibit some non-linear behaviour, which can depend on many factors, such as frequency, temperature, field strength, etc. [19]. Increased noise is also observed from ferromagnetic materials due to the Barkhausen effect [20].

Considering the possible presence of a ferromagnetic core, the sensor output voltage is:

$$v_s(t) = -\mu_a N\, \frac{d\mathbf{B}}{dt} \cdot \mathbf{n}\, A_c \tag{1.23}$$

where $\mu_a = 1$ in the case of air-core coils.

If the magnetic field applied to the sensor is sinusoidal with amplitude $\mathbf{B_0}$ (Equation 1.24), as is typically the case for EMT systems, Equation 1.23 can be further simplified into Equation 1.25, where ω is the received field angular frequency:

$$\mathbf{B} = \mathbf{B_0}(x, y, z)\ \sin(\omega t) \tag{1.24}$$

$$v_s(t) = -\mu_a N \omega \cos(\omega t)\, \mathbf{B_0} \cdot \mathbf{n}\, A_c \tag{1.25}$$

If only the magnitudes are considered (capital letters V_s and B_0) and the field is perpendicular to the area, the dependence on the magnetic induction may be made explicit and Equation 1.26 is obtained, where f is the frequency in Hertz and k_s is the sensitivity of the sensor in Volts per Tesla per Hertz ($\mathrm{V\,T^{-1}\,Hz^{-1}}$):

$$V_s = \mu_a N 2\pi f\, B_0\, A_c = k_s f B_0 \tag{1.26}$$

$$k_s = 2\pi N A_c \mu_a \tag{1.27}$$

Typical values for the sensitivities of commercial sensors, such as Aurora Sensors (*Northern Digital Inc.*, — [21]), are $0.1 - 0.2\,\mathrm{V\,T^{-1}\,Hz^{-1}}$ [22, Chap. 3].

1.3.4 Demodulation

As said, the signal of the inductive sensor is a superposition of the eight different frequencies of the emitter coils in the field generator. Each contribution needs to be extracted in order to provide the set of eight field strengths needed for position and orientation solving. After amplification and data acquisition, the demodulation process takes place in MATLAB. At the time of calculation, an acquisition frame of the sampled signal is processed, in contrast to real-time processing where samples are considered one-by-one in turn.

The voltage induced on the sensor, discretised through sampling, is in the form:

$$x[n] = \sum_{i=1}^{8} x_i[n] = \sum_{i=1}^{8} V_i \cos\left(\frac{2\pi f_i n}{f_s} + \varphi_i\right) \tag{1.28}$$

where f_s is the sampling frequency and V_i and φ_i are the amplitude and the phase shift of the component at frequency f_i. It results in a vector $\mathbf{X}$ containing the number p of samples processed together:

$$\mathbf{X} = \big[x[0], x[1], \ldots, x[p-1]\big] \tag{1.29}$$

To extract the information needed, a Fourier analysis of the 8 frequencies of interest is accomplished. If $x(t)$ is a generic continuous signal, of period T, the amount of energy that $x(t)$ stores on the frequency f is given by the integral:

$$x_\omega = \frac{1}{T} \oint_{[T]} x(t) \cdot e^{-j2\pi f t}\, dt \tag{1.30}$$

where $j = \sqrt{-1}$ is the imaginary unit.

Equation 1.30 can be extended to discrete signals, where the integral becomes a sum. If T_w is the time span of the p samples of $\mathbf{X}$, the amplitude of the component of $x[n]$ at frequency f_i is:

$$\overline{V_i} = V_i e^{j\varphi_i} = \frac{2}{p}\sum_{n=0}^{p-1} x[n]\cdot e^{-j\frac{2\pi f_i n}{f_s}} = \frac{2}{p}\sum_{n=0}^{p-1} x[n]\cdot e^{-j\frac{2\pi n}{p}k_i} \tag{1.31}$$

being $p = f_s T_w$ and where $k_i = f_i T_w$ is the frequency index and indicates how many periods of the component at frequency f_i are contained inside the acquisition frame period T_w. The factor $\times 2$ is needed because the cosine wave at frequency f_i includes both the exponential frequencies $+f_i$ and $-f_i$.

The formula of Equation 1.31 works properly only if the time T_w is a multiple of the sampling period $T_s = 1/f_s$ and of the period of the frequency of interest $T_i = 1/f_i$. In other words, p and k_i must be integers. In the reality this is not true, then more sophisticated signal processing methods, which make use of windowing functions [23][24], are implemented in the demodulation code.

To efficiently compute Equation 1.31 in MATLAB, a $[p\times 8]$ matrix of complex exponentials is created:

$$\mathbf{E} = \begin{bmatrix} \epsilon_1[0] & \dots & \epsilon_8[0] \\ \vdots & \ddots & \vdots \\ \epsilon_1[p-1] & \dots & \epsilon_8[p-1] \end{bmatrix} \tag{1.32}$$

where

$$\epsilon_i[n] = e^{-j\frac{2\pi n}{p}k_i} \tag{1.33}$$

The row vector of demodulated voltages is given by premultiplying $\mathbf{E}$ by the row vector $\mathbf{X}$ of p samples:

$$\mathbf{Y} = [\overline{V}_1, \dots, \overline{V}_8] = \frac{2}{p}\mathbf{X}\,\mathbf{E} \tag{1.34}$$

where $\overline{V_i}$ are complex values. The absolute value of each entry in $\mathbf{Y}$ is the amplitude V_i, while the argument is the phase φ_i of the component at the frequency f_i.

The procedure described assumes the eight frequencies to be known exactly and it is therefore a *synchronous demodulation*. This requires each of the eight coils currents to be individually sampled with an analogue to digital converter at a very high sampling frequency and the use of phase-locking techniques. However, it is more convenient to use simulated reference signals, which are not locked in phase with the signal to be demodulated. Such a technique is called *asynchronous demodulation*. The frequency mismatch results in a low frequency component present in the demodulated signal.

For example, let $\omega_i = 2\pi f_i$ be the angular frequency of interest present in the signal $x[n]$ and ω_{ri} be the reference angular frequency used for demodulation. Equation 1.31 provides:

$$\widetilde{V_i} = V_i e^{j(\omega_i-\omega_{ri})t+j\varphi_i} = V_i e^{j\Delta\omega_i t+j\varphi_i} = V_i e^{j\widetilde{\varphi_i}} \tag{1.35}$$

where, for simplicity, the signals are considered continuous. Note that $t = nT_s$ if the signals are discrete in time. The phase of the i^{th} demodulated signal varies with time, so it

is not possible to determine the orientation of the sensor.

The problem is solved by processing the currents of the field generator. A current amplifier (TL082, *Texas Instruments, Dallas, Texas*) is used to efficiently sum the currents of the emitter coil PCBs. The composite signal is demodulated in an identical manner to the sensor signal. The signal obtained in this way is:

$$\widetilde{I_i} = I_i e^{j\Delta\omega_i t + j\psi_i} = I_i e^{j\widetilde{\psi_i}} \tag{1.36}$$

From the two demodulated signals of Equation 1.35 and Equation 1.36 it is possible to recover the phase information:

$$\varphi_i - \psi_i = \widetilde{\varphi_i} - \widetilde{\psi_i} = \pm 90^\circ \tag{1.37}$$

As denoted by Equation 1.37, the voltage induced in the sensor can be 90° in advance or in delay with respect to the inductive field (and the associated generating current), depending on the axial orientation of the electromagnetic sensor with respect to the magnetic field.

The described double demodulation allows both the accurate retrieval of the amplitude and phase of each of the induced sensor voltages.

1.3.5 Sensor calibration

Calibration is a necessary procedure aimed to find the scaling factor between the sensor voltage measurement and the incident magnetic field, for each frequency of the emitter coils.

As described in paragraph 1.3.3, every inductive sensor has a typical sensitivity which indicates the magnitude of the induced voltage per unit incident magnetic field and unit frequency. The filament model described in paragraph 1.3.2 calculates the magnetic field at every point of the space, given the current of each emitter coil. However, in the system there are parameters, such as amplifiers gains and filters performances, that cannot be known to required precision solely through the system design. The result is that the measurement and the model of the magnetic field cannot be determined precisely through analytical means.

The procedure of calibration yields a scaling factor for each emitter coil, which encapsulates the otherwise difficult to determine circuit parameters. The sensor is subsequently placed at 49 test-points in a 7x7 grid and the voltage measurement is compared to the magnetic field predicted by model at the known position of the test-point.

Consider the magnetic flux measurements from the i^{th} emitter coil to be represented by Φ^i_{meas} and the associated modelled flux to be given by Φ^i_{model}. The objective function to be minimised (in a least-squares sense) is the error between the two fluxes and can be written as:

$$F_i(\kappa_i) = \sum_{j=1}^{49} \left(\Phi^i_{meas}(x_j, y_j, z_j, \theta_j, \varphi_j) - \kappa_i \Phi^i_{model}(x_j, y_j, z_j, \theta_j, \varphi_j) \right)^2 \tag{1.38}$$

where κ_i is the calibration scaling factor for a particular coil and $(x_j, y_j, z_j, \theta_j, \varphi_j)$ is the

known location and orientation of the sensor at test-point j (with a total of 49 test-points).

The function $\Phi^i_{model}(x, y, z, \theta, \varphi)$ can be described considering the coordinate system of Figure 1.1. The magnetic field at the point (x, y, z), modelled by Equation 1.17, is a vector with three components:

$$\mathbf{B}^i_{model}(x, y, z) = [B^i_x \; B^i_y \; B^i_z] \tag{1.39}$$

The orientation of the sensor is identified by the unit vector $\mathbf{n}$:

$$\mathbf{n}(\theta, \varphi) = [\sin\theta\cos\varphi \;\; \sin\theta\sin\varphi \;\; \cos\theta] \tag{1.40}$$

The magnetic flux due to the i^{th} emitter coil is proportional to the scalar product $\mathbf{B}^i \cdot \mathbf{n}$. The proportionality coefficient depends on the coil geometry (area, number of turns), on the core material and can be different for each emitter coil, because of non idealities of the system. It can be inherently included in the scaling factor κ_i, in which case the function Φ^i_{model} used in Equation 1.38 is:

$$\Phi^i_{model}(x, y, z, \theta, \varphi) = \mathbf{B}^i \cdot \mathbf{n} = B^i_x \sin\theta\cos\varphi + B^i_y \sin\theta\sin\varphi + B^i_z \cos\theta \tag{1.41}$$

The function $\Phi^i_{meas}(x, y, z, \theta, \varphi)$ is related to the voltage measured through the sensitivity of the sensor, which depends on frequency. Again, at a code level it is the same to include this value in κ_i. In this case, the measured voltage V^i_{meas} is directly used in Equation 1.38, in the place of Φ^i_{meas}.

The eight scaling factors κ_i map the magnetic field model of each transmitter coil to the domain of the sensor measurement.

1.3.6 Position and orientation solver

The position and orientation (P&O) solver takes the demodulated sensor data to resolve the position and angular orientation of the tracking sensor coil. The result is the array of values $(x, y, z, \theta, \varphi)$ which minimise the error between the measurements and the magnetic field model.

The P&O solver fulfils the opposite of calibration procedure. During calibration, a set of known test-points is used to produce a set of scaling factors, while the P&O solver utilises these scaling factors to minimise the same cost function for the unknown position and orientation.

The cost function of Equation 1.42 is minimised using non-linear least-squares solving methods (Levenberg-Marquardt [25]):

$$F(x, y, z, \theta, \varphi) = \sum_{i=1}^{8} \left(\Phi^i_{meas}(x, y, z, \theta, \varphi) - \kappa_i \Phi^i_{model}(x, y, z, \theta, \varphi) \right)^2 \tag{1.42}$$

Note that κ_i is the scaling factor for the i^{th} emitter coil and $(x, y, z, \theta, \varphi)$ is the unknown position and orientation of the tracking sensor.

1.4 Thesis Objectives

In the context of the research on electromagnetic tracking and, in particular, as a contribution to the project Anser EMT, this thesis focuses on the magnetic tracking sensor.

Electromagnetic modelling, theoretical investigation and experimental work were performed in order to obtain important results. The thesis describes in detail all the procedures followed and shows and comments the results.

The work contains novel knowledge and could be a relevant reference about the following topics:

- EMT principles, main difficulties of the method, state of art;
- Anser EMT project, overview of the system;
- Helmholtz coil theory, design procedures, advanced supply methods;
- Inductive sensor modelling, design, characterisation and integration in EMT systems;
- AMR effect theory, AMR sensor technologies, analysis of sinusoidal signals.

In the thesis, two main experimental works are of particular interest for EMT sensor research: the characterisation and positioning test of large-area inductive coil sensors and the characterisation of AMR sensors. The first was aimed to validate simple electrical models and analytical formulas useful in the design of novel geometry inductive sensors and to demonstrate the possibility of use of bespoke sensors within a tracking system. The purpose of the second work was to understand the operation and verify the expected behaviour of AMR sensors, for possible future integration in Anser EMT.

1.5 Thesis Structure

The dissertation is composed by five chapters:

1. *Chapter 1* gives an overview of electromagnetic tracking for use image-guided interventions, describes Anser EMT project, presents the arguments developed, the objectives of the work and the structure of the thesis.

2. *Chapter 2* focuses on the design and construction of a custom Helmholtz coil. The instrument was subsequently used to generate the magnetic field needed to characterise magnetic sensors. This work was preparatory for the experimental work subject of the following chapters.

3. *Chapter 3* describes in detail the measurement setup used to perform the characterisation over frequency of inductive sensors, shows and comments the results. Static accuracy test of the same sensors provided the average positional errors committed. The results are compared to the sensitivity obtained from the characterisation.

4. *Chapter 4* begins with a first overview of magnetoresistive effect, followed by a detailed study of AMR theory and sensor technology, with some considerations on the possible integration in EMT systems. Finally, the characterisation of an AMR sensor is presented.

5. *Chapter 5* discusses the topics for future work on electromagnetic tracking and presents some novel ideas that could be possibly investigated. In the end, the key results of the thesis are reviewed and final comments are given.

Bibliography

[1] K. Cleary and T. M. Peters, 'Image-Guided Interventions: Technology Review and Clinical Applications', *Annual Review of Biomedical Engineering*, vol. 12, no. 1, pp. 119–142, Jul. 2010, ISSN: 1523-9829. DOI: 10.1146/annurev-bioeng-070909-105249. [Online]. Available: http://www.annualreviews.org/doi/10.1146/annurev-bioeng-070909-105249.

[2] T. M. Peters and C. A. Linte, 'Image-guided interventions and computer-integrated therapy: Quo vadis?', *Medical Image Analysis*, vol. 33, pp. 56–63, Oct. 2016, ISSN: 13618423. DOI: 10.1016/j.media.2016.06.004. [Online]. Available: https://linkinghub.elsevier.com/retrieve/pii/S1361841516300780.

[3] J. P. Díaz-Jimenez and A. N. Rodriguez, *Interventions in pulmonary medicine*, J. P. Díaz-Jimenez and A. N. Rodriguez, Eds. Cham: Springer International Publishing, 2017, pp. 1–645, ISBN: 9783319580364. DOI: 10.1007/978-3-319-58036-4. [Online]. Available: http://link.springer.com/10.1007/978-3-319-58036-4.

[4] K. A. Khan, P. Nardelli, A. Jaeger, C. O'Shea, P. Cantillon-Murphy and M. P. Kennedy, *Navigational Bronchoscopy for Early Lung Cancer: A Road to Therapy*, Apr. 2016. DOI: 10.1007/s12325-016-0319-4. [Online]. Available: http://link.springer.com/10.1007/s12325-016-0319-4.

[5] E. J. Hermann, H.-H. Capelle, C. A. Tschan and J. K. Krauss, 'Electromagnetic-guided neuronavigation for safe placement of intraventricular catheters in pediatric neurosurgery', *Journal of Neurosurgery: Pediatrics*, vol. 10, no. 4, pp. 327–333, Oct. 2012, ISSN: 1933-0707. DOI: 10.3171/2012.7.PEDS11369. [Online]. Available: https://thejns.org/view/journals/j-neurosurg-pediatr/10/4/article-p327.xml.

[6] F. Kral, E. J. Puschban, H. Riechelmann, F. Pedross and W. Freysinger, 'Optical and electromagnetic tracking for navigated surgery of the sinuses and frontal skull base', *Rhinology*, 2011, ISSN: 03000729. DOI: 10.4193/Rhino10.177.

[7] E. E. Folch, M. R. Bowling, T. R. Gildea, K. L. Hood, S. D. Murgu, E. M. Toloza, M. M. Wahidi, T. Williams and S. J. Khandhar, 'Design of a prospective, multicenter, global, cohort study of electromagnetic navigation bronchoscopy', *BMC Pulmonary Medicine*, vol. 16, no. 1, p. 60, Dec. 2016, ISSN: 1471-2466. DOI: 10.1186/s12890-016-0228-y. [Online]. Available: http://bmcpulmmed.biomedcentral.com/articles/10.1186/s12890-016-0228-y.

[8] D. H. Yu and D. Feller-Kopman, 'Interventional bronchoscopy in adults', *Expert Review of Respiratory Medicine*, vol. 12, no. 3, pp. 239–248, Mar. 2018, ISSN: 1747-6348. DOI: 10.1080/17476348.2018.1429922. [Online]. Available: https://www.tandfonline.com/doi/full/10.1080/17476348.2018.1429922.

[9] K. Lam, J.-L. Bigcas, A. Luong, W. Yao and M. J. Citardi, 'Flexible Microsensor Technology for Real-Time Navigation Tracking in Balloon Sinus Ostial Dilation', *Allergy & Rhinology*, vol. 8, no. 1, ar.2017.8.0193, Jan. 2017, ISSN: 2152-6567. DOI:

10.2500/ar.2017.8.0193. [Online]. Available: http://journals.sagepub.com/doi/10.2500/ar.2017.8.0193.

[10] *OpenEMT*. [Online]. Available: https://openemt.org.

[11] H. A. Jaeger, 'Creating an open source electromagnetic tracking platform', PhD thesis, 2018.

[12] *Anser EMT (Open Science Framework)*. [Online]. Available: https://osf.io/47q8q/.

[13] *AnserEMT (git repository)*. [Online]. Available: https://github.com/BioDesignUCC/AnserEMT.

[14] A. Plotkin, O. Shafrir, E. Paperno and D. M. Kaplan, 'Magnetic Eye Tracking: A New Approach Employing a Planar Transmitter', *IEEE Transactions on Biomedical Engineering*, vol. 57, no. 5, pp. 1209–1215, May 2010, ISSN: 0018-9294. DOI: 10.1109/TBME.2009.2038495. [Online]. Available: http://ieeexplore.ieee.org/document/5415595/.

[15] *Bottom plate*. [Online]. Available: https://openemt.org/images/9/9f/Bottomplate.PNG.

[16] *Coil diagram*. [Online]. Available: https://openemt.org/images/0/0b/Coildiagram.png.

[17] C. L. W. Sonntag, M. Sprée, E. A. Lomonova, J. L. Duarte and A. J. A. Vandenput, 'Accurate Magnetic Field Intensity Calculations for Contactless Energy Transfer Coils', *Proceedings of the 16th International Conference on the Computation of Electromagnetic Fields, Achen, Germany*, pp. 1–4, 2007.

[18] H. A. Haus and J. R. Melcher, *Electromagnetic fields and energy*. Prentice Hall Englewood Cliffs, NJ, 1989, vol. 107.

[19] C. Coillot and P. Leroy, 'Induction Magnetometers Principle, Modeling and Ways of Improvement', in *Magnetic Sensors - Principles and Applications*, K. Kuang, Ed., InTech, Mar. 2012, ch. 3, ISBN: 978-953-51-0232-8. DOI: 10.5772/1361. [Online]. Available: http://www.intechopen.com/books/magnetic-sensors-principles-and-applications.

[20] S. Tumanski, 'Induction coil sensors - A review', *Measurement Science and Technology*, 2007, ISSN: 13616501. DOI: 10.1088/0957-0233/18/3/R01.

[21] Northern Digital Inc., *Aurora 5DOF Sensor 0.5 mm x 8 mm, Part Number: 610099*. [Online]. Available: https://www.ndigital.com/medical/products/tools-and-sensors/.

[22] K. O'Donoghue, 'Electromagnetic tracking and steering for catheter navigation', PhD thesis, 2014. [Online]. Available: https://cora.ucc.ie/handle/10468/2025.

[23] F. Harris, 'On the use of windows for harmonic analysis with the discrete Fourier transform', *Proceedings of the IEEE*, vol. 66, no. 1, pp. 51–83, 1978, ISSN: 0018-9219. DOI: 10.1109/PROC.1978.10837. [Online]. Available: http://ieeexplore.ieee.org/document/1455106/.

[24] S. S. Haykin and B. Van Veen, 'Fourier Representations of Signals and Linear Time-Invariant Systems', in *Signals and Systems*, Wiley, 2002, ch. 3, p. 802, ISBN: 0471164747.

[25] J. E. Dennis Jr and R. B. Schnabel, 'Nonlinear Least Squares', in *Numerical methods for unconstrained optimization and nonlinear equations*, vol. 16, 1996, ch. 10, ISBN: 1611971209.

Chapter 2

Helmholtz coil

The Helmholtz coil is an instrument used to generate a highly uniform magnetic field. It is a simple configuration of two paired coils (Figure 2.1). If the current flowing in the two coils is given, the magnetic field in the centre is known with high precision. To perform the characterisation of magnetic field sensors, it is very important for the known magnetic field to be quite uniform around the sensor position, for two main reasons: in this way the exact placement of the sensor is less restrictive and because the sensor, which has a finite area, links the field at different positions of the space.

In this chapter, an overview of the theory behind the Helmholtz coil configuration is given, the experimental setup of the Helmholtz coil that will be used to characterise the sensors is presented and, finally, the possible ways to supply the Helmholtz coil are investigated.

2.1 Helmholtz coil theory

2.1.1 Magnetic field due to a single loop

Consider a loop Γ of current I and a point P placed on the axis z of the loop, as in Figure 2.2.

Every infinitesimal segment of current $I\,dl$ placed at a generic point Q of the loop gives a contribution to the field in P, described by Biot-Savart law. The total field is given by the integral:

$$\mathbf{B}(\mathrm{P}) = \oint_{\Gamma} \frac{\mu_0 I}{4\pi(R^2+z^2)}\,\mathbf{u}_{\varphi} \times \mathbf{u}_{\mathrm{QP}}\,dl \tag{2.1}$$

where R is the radius of the loop, z is the distance between the point Q and the centre of the loop, $\mathbf{u}_{\varphi}$ is the azimuthal unit vector pointing in the direction of the current and $\mathbf{u}_{\mathrm{QP}}$ is the unit vector pointing in the direction $\overrightarrow{\mathrm{QP}}$. Noting that:

$$\mathbf{u}_{\mathrm{QP}} = \frac{-\mathbf{u}_{\mathrm{r}}R + \mathbf{u}_{\mathrm{z}}z}{\sqrt{R^2+z^2}} \tag{2.2}$$

$$\mathbf{u}_{\varphi} \times -\mathbf{u}_{\mathrm{r}} = \mathbf{u}_{\mathrm{z}} \tag{2.3}$$

$$\mathbf{u}_{\mathrm{QP}} \times \mathbf{u}_{\mathrm{z}} = \mathbf{u}_{\mathrm{r}} \tag{2.4}$$

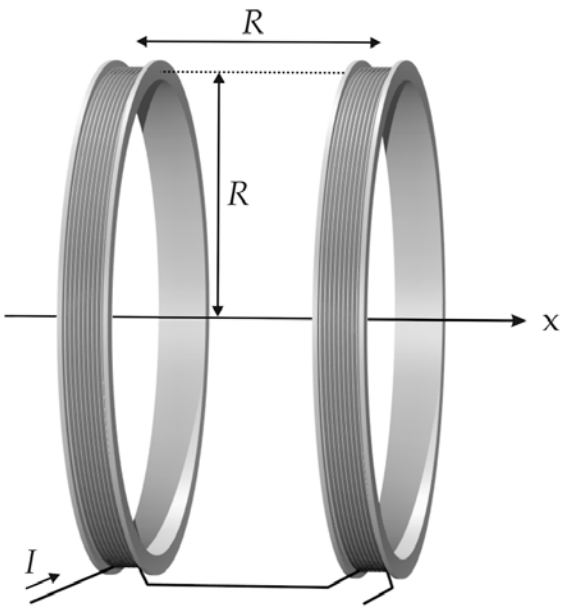

Figure 2.1: The Helmholtz coil configuration is realized when two equal coils are placed on the same axis, at a distance equal to their radius. *Image source: [1].*

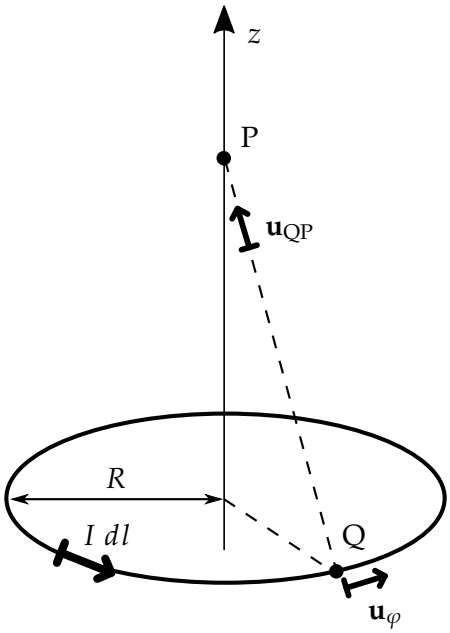

Figure 2.2: Magnetic field due to a circular loop.

and since, by symmetry, the radial component $\mathbf{u}_\mathrm{r}$ gives null contribution to the integral, Equation 2.5 is obtained:

$$\mathbf{B}(\mathrm{P}) = \frac{\mu_0 I}{4\pi} \int_0^{2\pi} \frac{1}{R^2 + z^2} \frac{R\mathbf{u}_\mathrm{z}}{\sqrt{R^2 + z^2}}\, d\theta \tag{2.5}$$

Therefore, $\mathbf{B}$ on the axis has only the z component and its value is:

$$B_z = \frac{\mu_0 I R^2}{2(R^2 + z^2)^{\frac{3}{2}}} \tag{2.6}$$

2.1.2 Magnetic field in the Helmholtz coil configuration

The Helmholtz coil system consists of two parallel identical coils, on the same axis and carrying the same current. In a linear and homogeneous medium, such as air, the field on the axis z is the sum of the fields generated by the two coils. At the centre between the two coils, all the odd derivatives of the field with respect to z are null. This conclusion can be easily reached if the origin of the axis z is set at the centre of the system. In this case, the field is an even function, by symmetry, and then its Taylor expansion on z does not contain odd terms. Then the odd derivatives are null when $z = 0$. By arranging the coils so that the second order derivative is null in $z = 0$, a very homogeneous field is obtained, where the first non-constant term is of fourth order. Figure 2.3 shows how the magnetic field on the axis changes when the two coils are moved.

The first and second order derivatives of the field generated by a single coil, expressed by Equation 2.6, are:

$$\begin{aligned} \frac{\partial B_z}{\partial z} &= -\frac{3}{2} \frac{\mu_0 I R^2}{(z^2 + R^2)^{5/2}}\, z \\ \frac{\partial^2 B_z}{\partial^2 z} &= \frac{15}{2} \frac{\mu_0 I R^2}{(z^2 + R^2)^{7/2}}\, z^2 - \frac{3}{2} \frac{\mu_0 I R^2}{(z^2 + R^2)^{5/2}} \end{aligned} \tag{2.7}$$

The condition of null second order derivative is reached when:

$$\frac{15}{2} \frac{\mu_0 I R^2}{(z^2 + R^2)^{7/2}}\, z^2 = \frac{3}{2} \frac{\mu_0 I R^2}{(z^2 + R^2)^{5/2}} \rightarrow z = \pm \frac{R}{2} \tag{2.8}$$

In conclusion, the field at the centre is uniform up to the fourth order when the two coils are arranged at a separation distance equal to their radius R (Figure 2.1).

2.2 Design of the Helmholtz coil

2.2.1 Geometrical dimensions

In the Helmholtz coil configuration, the on-axis field at the centre of the two coils is computed by Equation 2.6 with $z = \pm R/2$ and doubling the result, to consider the

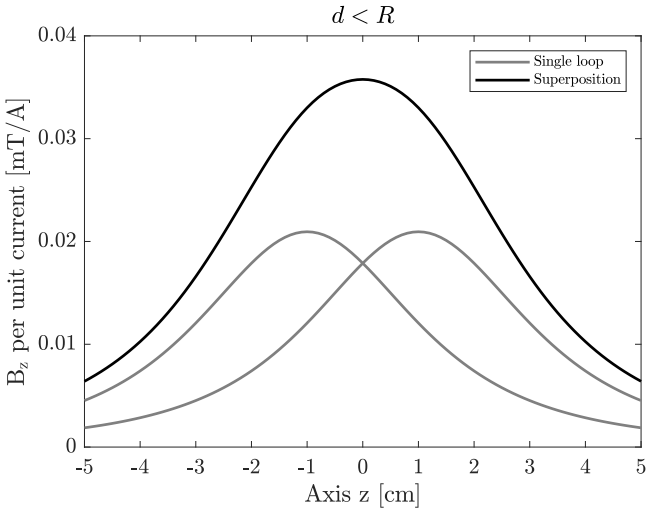

(a) Distance lower than the coil radius.

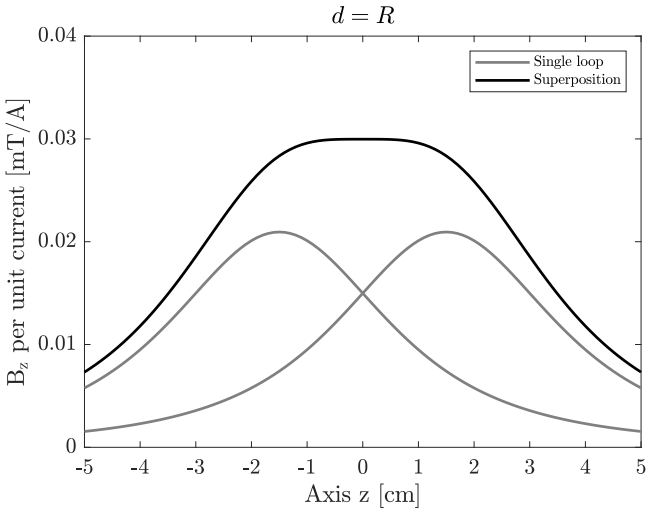

(b) Distance equal to the coil radius.

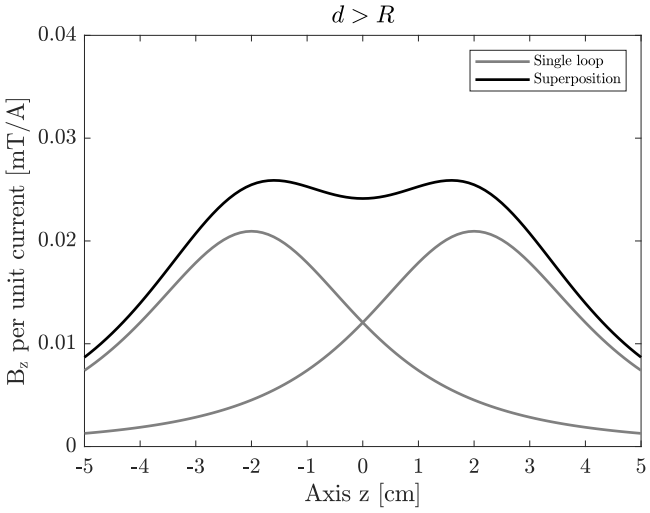

(c) Distance bigger than the coil radius.

Figure 2.3: Magnetic field (z direction) on the axis z. In gray: the one generated by the current of each coil; in black: the total magnetic field (superposition).

contribution of the two coils [2]. Then B_z is related to the current by:

$$\frac{B_z}{I} = \left(\frac{4}{5}\right)^{3/2} \frac{\mu_0 N}{R} = \frac{1.80\times10^{-6}}{D} \cdot N \quad \left[\frac{\mathrm{T}}{\mathrm{A}}\right] \tag{2.9}$$

where $D = 2R$ is the diameter of the coils and N is the number of turns of each coil.

The smaller the Helmholtz coil is, the larger the field per unit current is. Therefore, it is convenient to choose the smallest dimension possible, in accordance with the dimension of the sensors that are to be characterised. The sensor should be "small" with respect to the Helmholtz coil, in order to measure only the "local" field at the centre. For the custom Helmholtz coil used in this work, a distance d and a radius R of 3 cm were chosen.

2.2.2 Inductance

The inductance of the Helmholtz coil was predicted using numerical approaches. The mutual inductance between two coaxial parallel loops is [3, Chap. 4] (see also Equation 5.37 of [4]):

$$M_{12} = \mu_0 \sqrt{R_1 R_2} \left[\left(\frac{2}{k} - k \right) K(k) - \frac{2}{k} E(k) \right] \quad [\mathrm{H}] \tag{2.10}$$

where R_1 and R_2 are the radii of the two loops (Figure 2.4) and $K(k)$ and $E(k)$ are the elliptic integrals of first and second kind of modulus k:

$$E(k) = \int_{\theta=0}^{\pi/2} \frac{d\theta}{\sqrt{1 - k^2 \sin^2\theta}} \tag{2.11}$$

$$K(k) = \int_{\theta=0}^{\pi/2} \sqrt{1 - k^2 \sin^2\theta}\, d\theta \tag{2.12}$$

$$k^2 = \frac{4R_1R_2}{(R_1 + R_2)^2 + d^2} \tag{2.13}$$

The numerical solution, implemented in MATLAB, computes the flux that every turn links to any other, as shown in Figure 2.5. Considering that air permeability μ_0 is constant, superposition of effects can be used and the relation between the currents and the voltages of each turn is expressed in matrix form by Equation 2.14.

$$\begin{pmatrix} v_{A1} \\ \vdots \\ v_{An} \\ v_{B1} \\ \vdots \\ v_{Bn} \end{pmatrix} = \begin{bmatrix} \begin{bmatrix} M_{A1A1} & \dots & M_{A1An} \\ \vdots & \ddots & \vdots \\ M_{AnA1} & \dots & M_{AnAn} \end{bmatrix} & \begin{bmatrix} M_{A1B1} & \dots & M_{A1Bn} \\ \vdots & \ddots & \vdots \\ M_{AnB1} & \dots & M_{AnBn} \end{bmatrix} \\ \begin{bmatrix} M_{B1A1} & \dots & M_{B1An} \\ \vdots & \ddots & \vdots \\ M_{BnA1} & \dots & M_{BnAn} \end{bmatrix} & \begin{bmatrix} M_{B1B1} & \dots & M_{B1Bn} \\ \vdots & \ddots & \vdots \\ M_{BnB1} & \dots & M_{BnBn} \end{bmatrix} \end{bmatrix} \cdot \frac{d}{dt} \begin{pmatrix} i_{A1} \\ \vdots \\ i_{An} \\ i_{B1} \\ \vdots \\ i_{Bn} \end{pmatrix} \tag{2.14}$$

Since the turns of each coil are all in series, then $i_A = i_{A1} = i_{A2} = \cdots = i_{An}$ for the current and $v_A = v_{A1} + v_{A2} + \cdots + v_{An}$ for the voltage of Coil A; the same consideration applies to

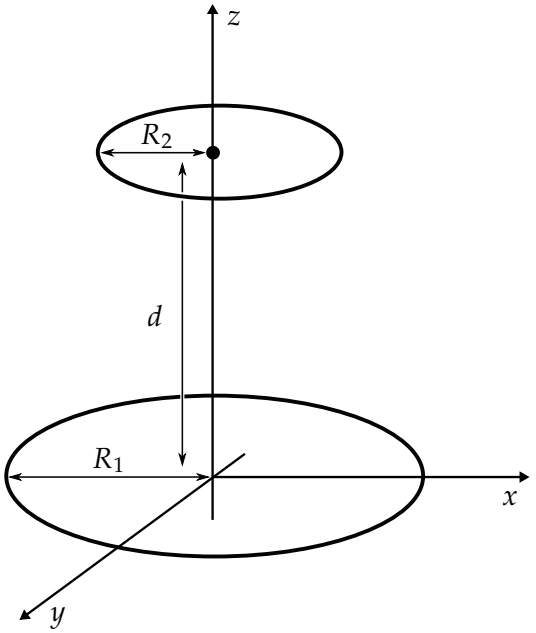

Figure 2.4: Two parallel and coaxial loops, at a distance d.

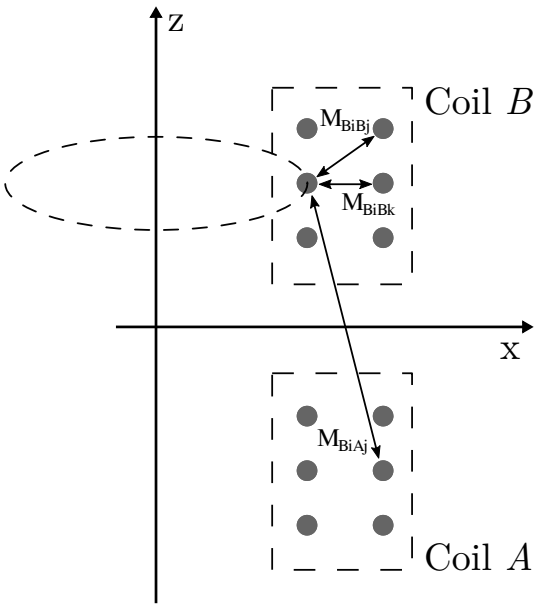

Figure 2.5: Any turn of the two coils is mutually coupled to any other turn, of the same coil and of the other.

self inductance of the single coil	$L_{coil} = 1.1280\times10^{-7} \cdot N^2$ [H]
mutual inductance between two coils	$M = 1.4874\times10^{-8} \cdot N^2$ [H]
coupling coefficient	$k = \sqrt{\frac{L_A L_B}{M^2}} = \frac{L_{coil}}{M} = 0.1319$
total inductance of the series	$L_{total} = 2L + 2M = 2.5535\times10^{-7} \cdot N^2$ [H]

Table 2.1: Results of the numerical simulation to predict the inductance of the Helmholtz coil.

Coil B. So the matrix relation becomes:

$$\begin{pmatrix} v_A \\ v_B \end{pmatrix} = \begin{bmatrix} L_A & M_{AB} \\ M_{BA} & L_B \end{bmatrix} \cdot \frac{d}{dt} \begin{pmatrix} i_A \\ i_B \end{pmatrix} \tag{2.15}$$

where L_A and L_B are obtained by the sum of all the mutual inductances inside the same coil and $M_{AB} = M_{BA} = M$ is the sum of the mutual inductances between turns of different coils. It should be noted that the two coils are built identically, so $L_A \approx L_B \approx L_{coil}$. Finally, the two coils are put in series, so that the current and the voltage of the Helmholtz coil are: $i_{HC} = i_A = i_B$ and $v_{HC} = v_A + v_B$. Then:

$$\begin{aligned} v_{HC} = v_A + v_B &= L_A \frac{d}{dt} i_A + M_{BA} \frac{d}{dt} i_A + M_{AB} \frac{d}{dt} i_B + L_B \frac{d}{dt} i_B \\ &= (L_A + M_{BA} + M_{AB} + L_B) \frac{d}{dt} i_{HC} \\ &= (2L_{coil} + 2M) \frac{d}{dt} i_{HC} \quad \text{[V]} \end{aligned} \tag{2.16}$$

and the total inductance is:

$$L_{total} = 2(L_{coil} + M) \quad \text{[H]} \tag{2.17}$$

leading to:

$$v_{HC} = L_{total} \frac{d}{dt} i_{HC} \quad \text{[V]} \tag{2.18}$$

Inductance computed by simulation increased quite correctly with the square of the number of turns N. This may be expected, since N counts two times in the definition of inductance: one for the field generated, at equal current, and one for the total flux linked to the coils, that is the sum of the flux linked to each turn. Disparities from the ideal N^2 dependence come from the self and mutual coupling, depending on the spatial position of the turns. For example Table 2.1 shows the results obtained with 6 turns per coil and a cross sectional area for winding of width $b = 4.5\,\text{mm}$ and height $h = 3\,\text{mm}$. The values reported are per unit turn and will be used in the following analysis.

The comparison with the analytical formula proposed by Wheeler [5] is comparable to

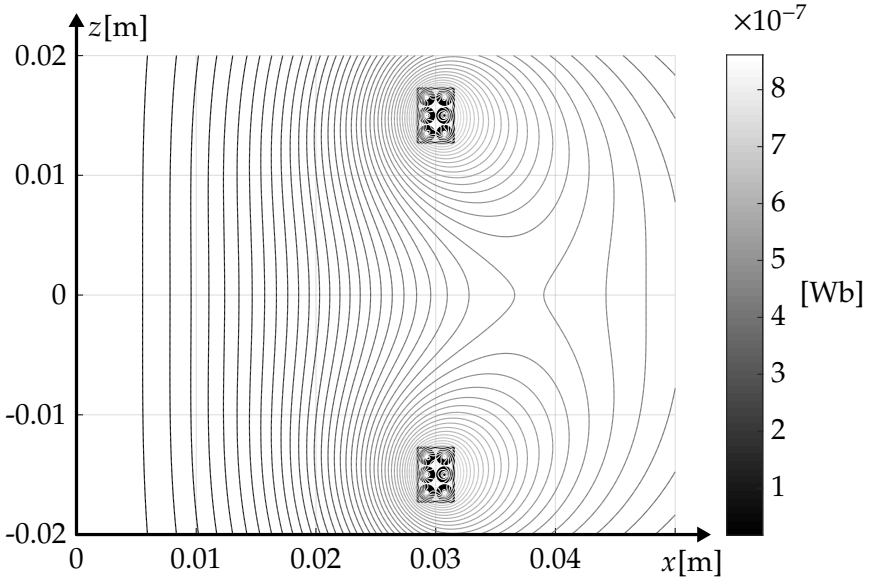

Figure 2.6: Axisymmetric flux map resulting from the numerical simulation for unit current in each coil.

the results of the MATLAB simulation:

$$L_{wheeler} = \frac{0.8N^2R^2}{6R+9b+10h}\left[\cdot 39.3701\frac{\text{inch}}{\text{m}}\right] = 1.1316\times10^{-7}\cdot N^2 \quad [\text{H}]$$
$$\text{to be compared with } L_{coil} = 1.1280\times10^{-7}\cdot N^2 \quad [\text{H}] \tag{2.19}$$

The limit with this formula is that it can only predict the single coil self inductance and not the mutual coupling between the two coils.

Using bespoke numerical investigation it is also possible to visualize the flux density map for the two coils, as shown in Figure 2.6. The 2D axial-symmetric domain is filled by a grid of points, representing fictitious loops, in which the magnetic flux given by every turn, considered with unitary impressed current, is calculated; the contours of this set of data are the lines of the **B** field.

2.2.3 Circuit model

The Helmholtz coil can be represented by a lumped parameter circuit model consisting in a series connected resistance and inductance. Parasitic capacitances can be modelled as a shunt capacitor. The final simplified circuit is the one of Figure 2.7. During preliminary design procedure, the self resonance frequency (SRF) $f_0 = 1/2\pi\sqrt{LC}$ was expected to be well over the frequencies of operation, so in subsequent analysis the presence of the capacitor was neglected.

The case of direct supply of the Helmholtz coil was firstly considered. The supply circuit consisted in a waveform generator (33500B Series, *Keysight Technologies, Santa Rosa, California* [6]) and a power amplifier (SPA1010, *Siglent, Helmond, Netherlands* [7]). The series

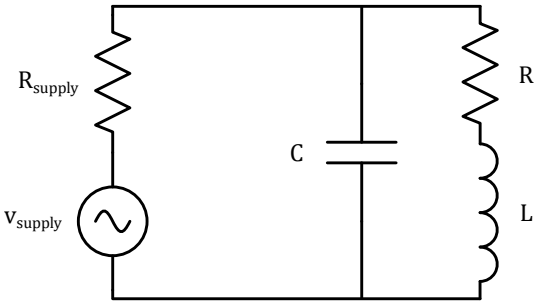

Figure 2.7: Simplified circuit for the Helmholtz coil.

output resistance of the power amplifier is less than 2 Ω. The internal DC resistance of the Helmholtz coil was expected to be much lower, around 0.1 Ω, so in the following analysis a total series resistance of 2 Ω was considered.

2.2.4 Limits of the power supply

The main problem in the use of the Helmholtz coil to generate an alternating magnetic field is that the impedance of the circuit increases with the frequency. The increment is linear when DC resistive effects can be neglected, at frequencies approximately a decade over the cut-off point $R/2\pi L$, hereafter referred as f_{RL}. To obtain the same current and magnetic field across frequencies, the supply voltage should increase linearly with frequency. The power amplifier used in this work has a limit on the maximum voltage that can be generated: $V_{limit} = \pm 13\,\text{V}$ [7]. Then, over a certain frequency the supply voltage has to be considered constant. If this is the case, the maximum field available at the centre is proportional to N^{-1}:

$$Z \propto N^2 \text{ (see Table 2.1), so } I = \frac{V}{Z} \propto N^{-2} \tag{2.20}$$

$$B \propto N \cdot I \text{ (see Equation 2.9)} \propto N^{-1} \tag{2.21}$$

Therefore, in order to maximise current over a wide frequency range, the number of turns and the inductance should be minimized.

However, there is also a limit on the maximum power deliverable through the power amplifier: $P_{limit} = \pm 10\,\text{W}$ [7]. A small value of coil inductance increases the frequency f_{RL} below which the impedance of the system may be considered resistive. In this situation, the current is limited (constant) and the maximum field in the centre is proportional to N:

$$I_{limit} = \sqrt{\frac{P_{limit}}{R}} = \text{ const.} \tag{2.22}$$

$$B \propto N \cdot I \text{ (see Equation 2.9)} \propto N \tag{2.23}$$

The value of inductance also affects the frequency where one constraint becomes more strict than the other, as shown in Figure 2.8. The same figure reveals that, starting from low frequencies, the impedance is almost only resistive, constant over frequency, and the voltage is limited by the maximum power. Around the frequency f_{RL}, the impedance

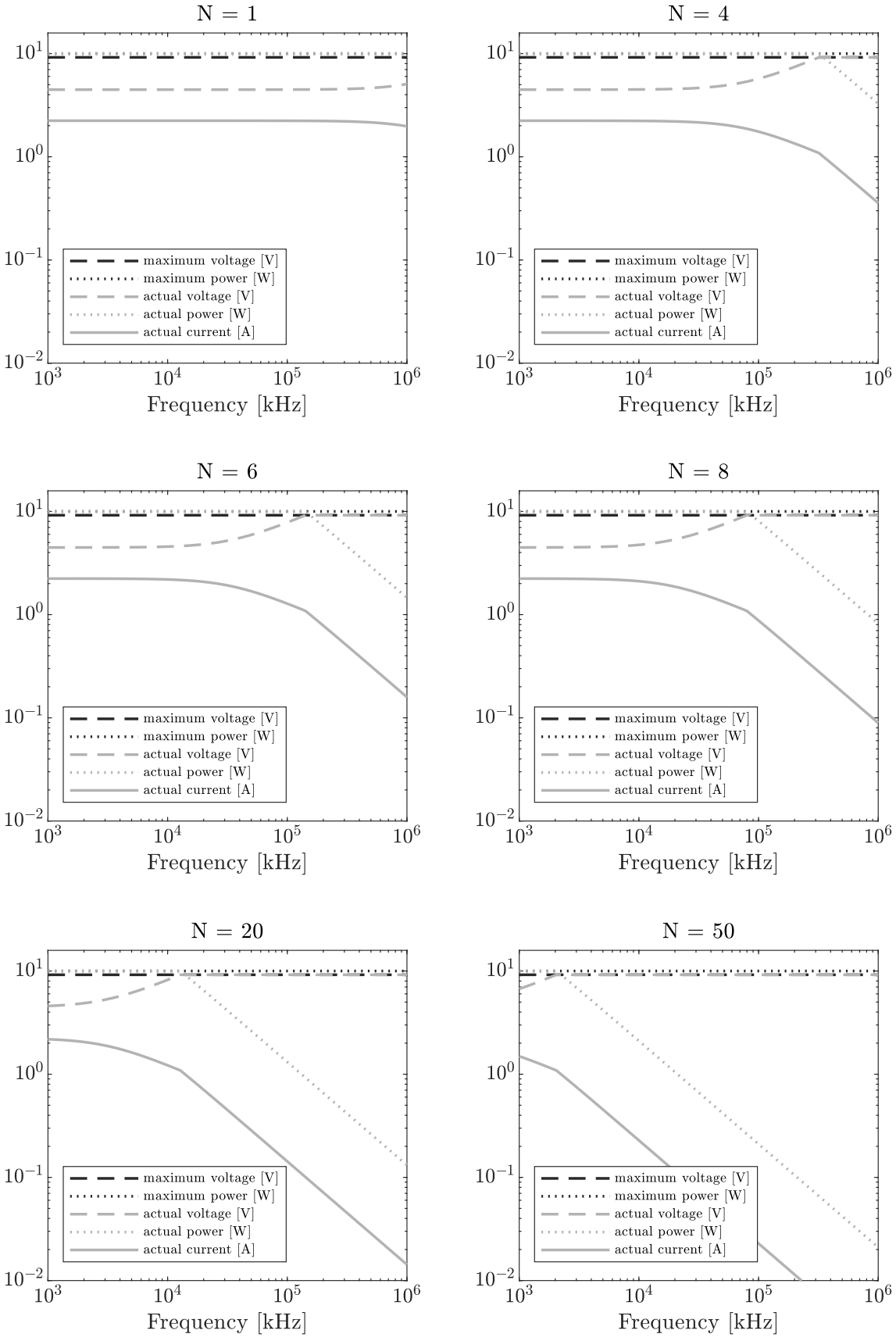

Figure 2.8: Actual values (in gray) of voltage, current and power, using the Helmholtz coil at the limit (in black) of actual operation.

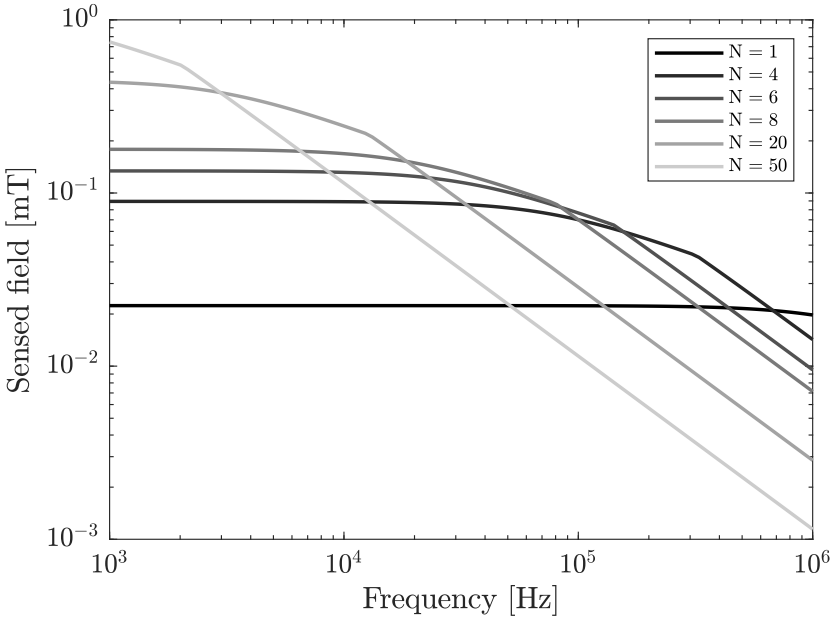

Figure 2.9: Maximum field that can be obtained at the centre of the coils, over the frequency.

starts to increase, due to the inductive contribution to coil impedance, such that the voltage increases with $\sqrt{f}$ and the current has to decrease with $1/\sqrt{f}$ to maintain the same power. A point is reached where the voltage cannot increase further because it hits its limit, so the voltage remains constant and the current decreases with $1/f$, since now the impedance is almost only inductive. This point in frequency will be denoted as f_L.

The optimum number of turns is therefore a trade-off and depends on the frequency range in which the magnetic field is to be maximized. Figure 2.9 shows the maximum field obtainable for every frequency, for different values of N. The sensors presented in this work were characterised in the frequency range 1 kHz – 1 MHz. However, frequencies under 100 kHz are relevant for Anser EMT application. With reference to Figure 2.9, a good compromise between an high field under 100 kHz and an acceptable field up to 1 MHz is reached with a number of 6 – 8 turns per coil.

2.3 Mechanical design of the Helmholtz coil

The analysis of section 2.2 determined a Helmholtz coil composed of two coils of 6 turns, with a radius of 3 cm. The support for the wire was designed using Solidworks (*Dassault Systèmes, Vélizy-Villacoublay, France*). A copper wire of 1.5 mm of diameter was used. The relatively thick diameter assures a low resistance, which limits ohmic heating, considering also that the resistance value may increase at high frequencies due to skin effect. The winding cross-sectional area was dimensioned to host two rows of three turns each (Figure 2.10).

The support was 3D printed and the wire was hand-wound on it. The internal DC resistance of the manufactured Helmholtz coil was measured with a true-rms multimeter

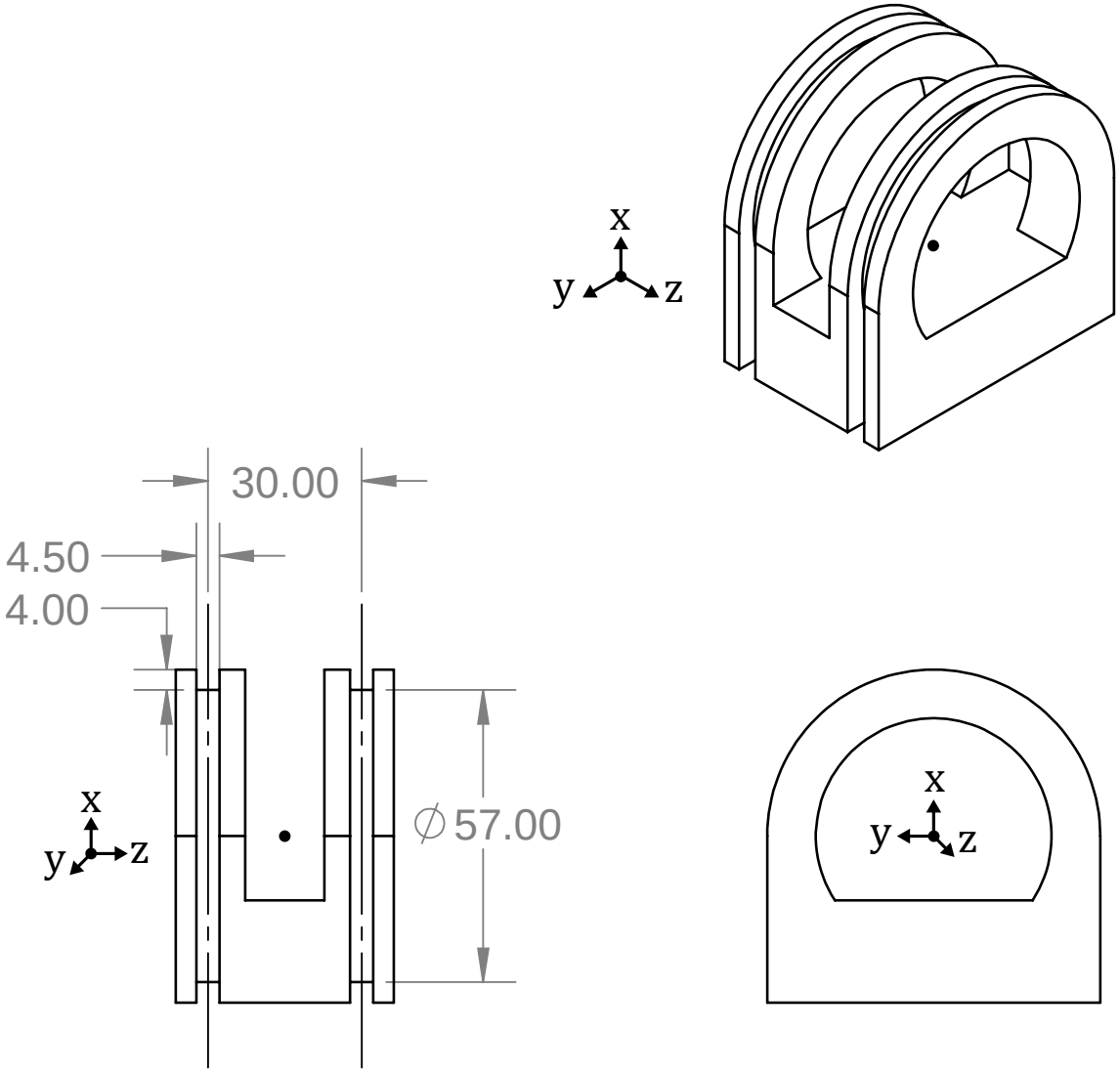

Figure 2.10: Measures of the support for the wire of the Helmholtz coil (Solidworks sketch).

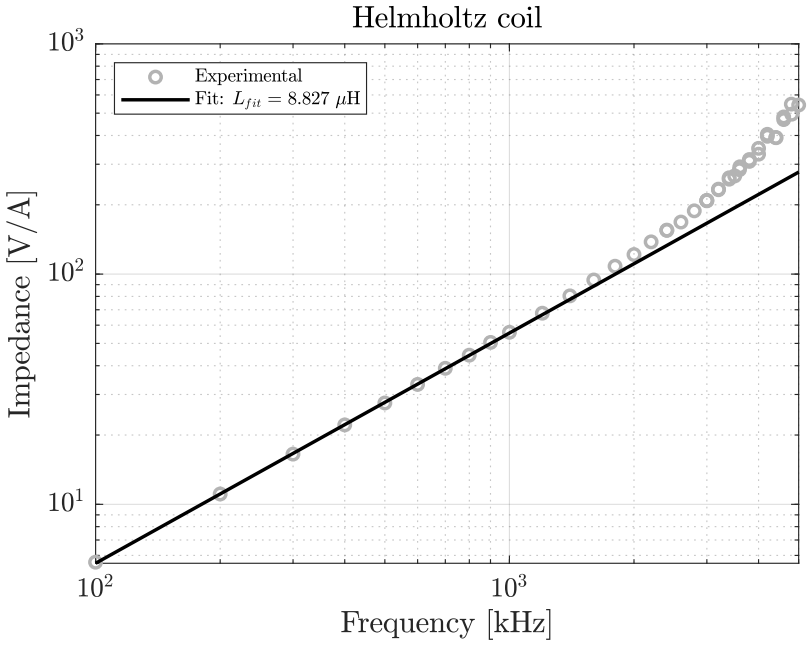

Figure 2.11: Characterisation of the Helmholtz coil impedance over frequency.

(Fluke 289, *Fluke Corporation, Eindhoven, Netherlands*). It resulted of 0.12 Ω, confirming that it is negligible with respect to the less-than-2 Ω series output resistance of the power amplifier, as assumed in paragraph 2.2.3.

The inductance was determined with an LCR Meter (4284A, *Keysight Technologies, —*). The measurement at 25 kHz provided a value of 8.90 µH. It is remarkable to note that the basic analytical calculation predicted a total inductance of 9.19 µH, as expressed in Table 2.1 for $N = 6$ turns. This demonstrates the goodness of the simplified design procedure described in previous sections.

The high frequency effects of parasitic capacitances were investigated through an impedance analysis over frequency. In paragraph 2.2.3 the SRF was assumed to be larger than the frequencies of interest (from 1 kHz to 1 MHz), allowing to consider the Helmholtz coil as an inductive load. Volt-amperometric measurements were performed up to 5 MHz, resulting in the impedance characteristic of Figure 2.11. Inductive behaviour can be noted at lower frequencies and the inductance value obtained by fitting, in a least squares sense, is 8.827 µH. High frequency effects start to become remarkable between 2 and 3 MHz. The data are quite noisy over 3 MHz because at those frequencies the measured current was very small (~ 5 mA), due to the higher value of impedance.

The analysis demonstrated that under 1 MHz parasitic effects can be neglected. In this case, all the current driven into the Helmholtz coil flows through the inductance and generates magnetic field. The magnetic field at the centre is determined analytically by Equation 2.9 and is approximately 180 µT A^{-1}.

2.4 Alternative power supply options for Helmholtz coils

The main challenge when using an Helmholtz coil to produce a high frequency magnetic field is that the impedance increases with frequency. For a given voltage amplitude (*e.g.* the maximum that the power supply can provide) the current decreases linearly with the frequency and also the field, from Equation 2.9. As previously shown in Figure 2.9, for acceptable current at higher frequencies, the value of the inductance L must be lowered by decreasing the number of turns N, but this also affects the field at the lower frequencies.

To overcome this problem, different possibilities to supply the current were considered and the results were compared with the performance of the direct supply. Some of these approaches are listed in [8].

2.4.1 Direct supply

The simplest method consists in the connection of the Helmholtz coil directly to the power supply. With the instruments used in this work, the maximum voltage available is ±13 V (see paragraph 2.2.4). In the worst case scenario of a generated field frequency $f = 1\,\text{MHz}$, with a resistance $R = 2\,\Omega$ and an inductance $L = 2.55{\times}10^{-7} \cdot 6^2 \approx 10\,\mu\text{H}$ (Table 2.1), the maximum current is:

$$I_{min} = \frac{13/\sqrt{2}}{R + j2\pi fL} \rightarrow |I_{min}| = \frac{13/\sqrt{2}}{\sqrt{2^2 + (2\pi 1{\times}10^6\, 10{\times}10^{-6})^2}} = 146\,\text{mA} \tag{2.24}$$

From Equation 2.9, with a current $I = 146\,\text{mA}$, a diameter $D = 6\,\text{cm}$ and 6 turns, the magnetic field produced is:

$$B_z = \frac{1.8{\times}10^{-6}}{6{\times}10^{-2}} 6 \cdot 146{\times}10^{-3} = 26.3\,\mu\text{T} \tag{2.25}$$

The maximum field is obtained in DC, when the Helmholtz coil has a negligible impedance and the circuit resistance is the $2\,\Omega$ output resistance of the power supply:

$$I_{max} = \sqrt{\frac{P_{max}}{Z_{min}}} = \sqrt{\frac{10}{2}} \rightarrow B_z = \frac{1.8{\times}10^{-6}}{6{\times}10^{-2}} 6 \cdot \sqrt{5} = 402\,\mu\text{T} \tag{2.26}$$

The point in frequency f_L when the power limit equals the voltage limit is:

$$\frac{(13/\sqrt{2})^2}{\sqrt{2^2 + (2\pi f_L 10{\times}10^{-6})^2}} = 10 \rightarrow f_L = 130.66\,\text{kHz} \tag{2.27}$$

In this condition, the field is $B_z = 196\,\mu\text{T}$ and it starts to decrease linearly as the frequency increases beyond 131 kHz.

If the sensor that measures the field is of inductive type, the output voltage is proportional to the frequency and to the amplitude of the field:

$$V_{out} = k_s f B_z \quad [\text{V}] \tag{2.28}$$

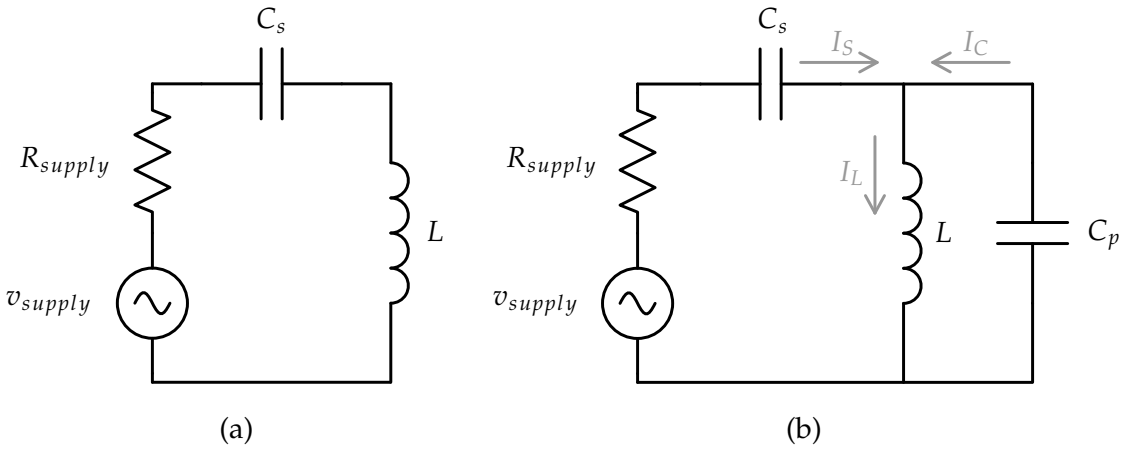

Figure 2.12: Two solutions for the supply circuit, which make use of a resonance point to: (a) increase the voltage on the Helmholtz coil and (b) double the current coming from the power supply.

where k_s is the sensitivity of the sensor, as explained in paragraph 1.3.3. As said, a typical value for the sensitivity of a commercial sensor used for electromagnetic tracking is of approximately $0.1\,\mathrm{V\,T^{-1}\,Hz^{-1}}$. The minimum voltage is measured at the minimum frequency of 1 kHz considered in this work. Being B_z approximately 400 µT from Equation 2.26, it results an induced voltage of:

$$|V_{out}| = k_s f B_z = 0.1 \cdot 1{\times}10^{3} \cdot 400{\times}10^{-6} = 40\,\mathrm{mV} \tag{2.29}$$

which is acceptable with respect to the typical noise.

An xMR sensor follows a different principle to measure the field (see chapter 4 for more details) and its ideal gain does not depend on frequency. For example, the sensitivity of the Sensitec AFF755B [9] is around $60\,\mathrm{V\,T^{-1}}$ and the output voltage at 1 MHz is then $V_{out} = 60 \cdot 26.3{\times}10^{-6} = 1.5\,\mathrm{mV}$. To measure such a low signal, the use of a signal amplifier or of more sophisticated supply methods are required.

2.4.2 Series resonant capacitor

It is possible to obtain supply voltage higher than the one that the power amplifier can provide by taking advantage of the resonance between the Helmholtz coil, pretty much inductive, and an external capacitor, C_s, added in series (Figure 2.12a). Even if the supply voltage is low, the actual voltage dropping on C_s and L can be higher, in a limited band around the resonance frequency of the $C_s - L$ series. For any given L, C_s has to be tuned for resonance at the frequency of interest f_0:

$$C_s = \frac{1}{(2\pi f_0)^2 L} \quad [\mathrm{F}] \tag{2.30}$$

The main disadvantage with this solution is that, to perform a characterisation of a sensor over frequency, C_s has to be changed for each frequency (at least at higher frequencies, when the voltage becomes the main limitation, as explained in paragraph 2.2.4). It has to

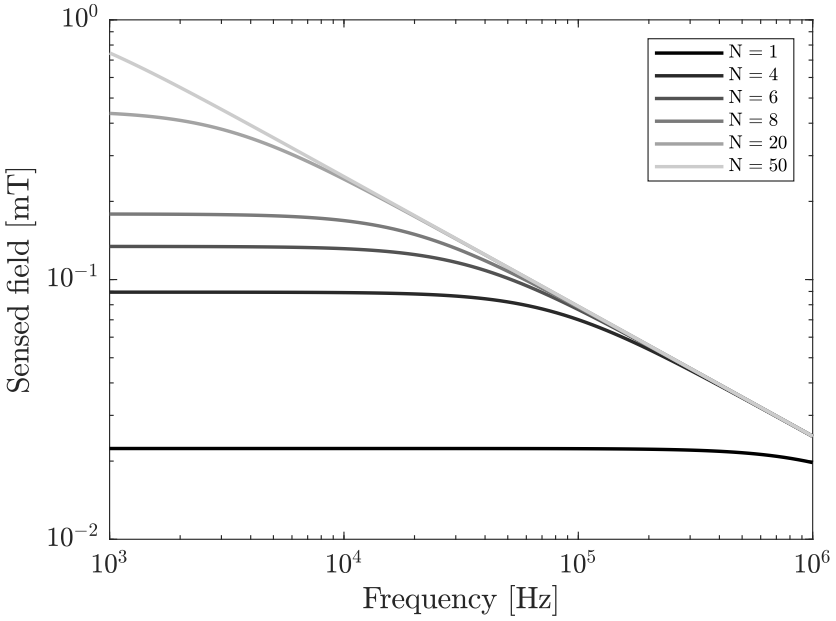

Figure 2.13: Maximum field that can be obtained using a series resonant capacitor C_s.

be noted that the actual voltage present in the circuit is high, due to resonance, so all the needed safeguard should be taken and the capacitor may be specified for that high voltage.

The same analysis described in paragraph 2.2.4 was accomplished and Figure 2.13 shows the maximum field attainable at any frequency, when voltage is not a limit of the system. At high frequencies, the field does not depend on the number of turns because the impedance is almost only inductive and proportional to N^2. The maximum current is then proportional to N^{-1}, where $Z \cdot I_{max}^2 = P_{limit} = \text{const.}$, and the field ($\propto N \cdot I$) is independent of N.

At lower frequencies, the impedance is almost only resistive, so the maximum current is constant and the field is linearly dependent on N. However, for larger N (and L) the voltage present in the circuit is higher and the frequency at which the series capacitor starts to be needed is lower, with consequences for insulation requirements, for capacitor dimensioning and for the number of capacitors used to cover the characterisation frequency range.

2.4.3 Current-amplified resonance

A modification of the approach of paragraph 2.4.2 is proposed in [10]. Another capacitance C_p is added in parallel to L (Figure 2.12b) and the second resonance point is used to double the current on the Helmholtz coil. At resonance frequency ω_0, the imaginary part of the circuit is null:

$$\frac{1}{j\omega_0 C_s} + \frac{1}{\frac{1}{j\omega_0 L} + j\omega_0 C_p} = 0 \tag{2.31}$$

From Equation 2.31, if the two capacitors are equal ($C_s = C_p = C$), it is possible to find ω_0:

$$\omega_0 = \frac{1}{\sqrt{2}\sqrt{LC}} \tag{2.32}$$

The two equal capacitors C are chosen for the required resonance frequency.

Kirchhoff's voltage law is applied in the parallel resonant loop $L - C$, such that:

$$I_C \frac{1}{j\omega C} + I_L \, j\omega L = 0 \rightarrow I_L = \frac{I_C}{\omega^2 LC} \tag{2.33}$$

At frequency $\omega = \omega_0 = \frac{1}{\sqrt{2LC}}$, from Equation 2.33 and considering that $I_L = I_S + I_C$, the current I_L becomes:

$$I_L = 2I_C = 2I_L - 2I_S \tag{2.34}$$

which directly gives:

$$I_L = 2I_S \tag{2.35}$$

It is so demonstrated that, at the resonance frequency ω_0, the current flowing in the Helmholtz coil I_L (and so the field generated) is two times the current provided by the power supply.

2.4.4 Helmholtz coil connection in parallel

Since the two coils of the Helmholtz array are build identically, they may be placed in parallel and the current through them would be the same. Small differences in the current do not significantly change the field at the centre of the coils. The impedance of the Helmholtz coil becomes four times smaller than the series connected case and the total current is four times larger, if the same supply voltage is applied.

In the range of frequencies in which the power available is the limiting condition, the supply voltage has to be reduced to halve the current. The total current then splits in half between the two coils. Therefore, the current in each coil is the same of the series configuration, so there is no advantage for the production of the field. Instead, for frequencies in which the inductive impedance dominates and the leading limitation is the maximum supply voltage, there is no necessity to halve the voltage and the field is actually doubled. Finally, from the point of view of the circuit, changing the connection from series to parallel has the same effect of halving the number of turns N (refer to Figure 2.9). For example, a Helmholtz coil composed of two coils of 6 turns connected in series has the same behaviour of a Helmholtz coil of two coils of 12 turns connected in parallel.

It is possible to take advantage of this stratagem to get an adjustable turn count N: using the series configuration when the frequency (and the impedance) is low and moving to the parallel connection when the high inductive impedance is limiting the current. Figure 2.14 shows the maximum field that can be obtained with this method, for the instrumentation used in this work.

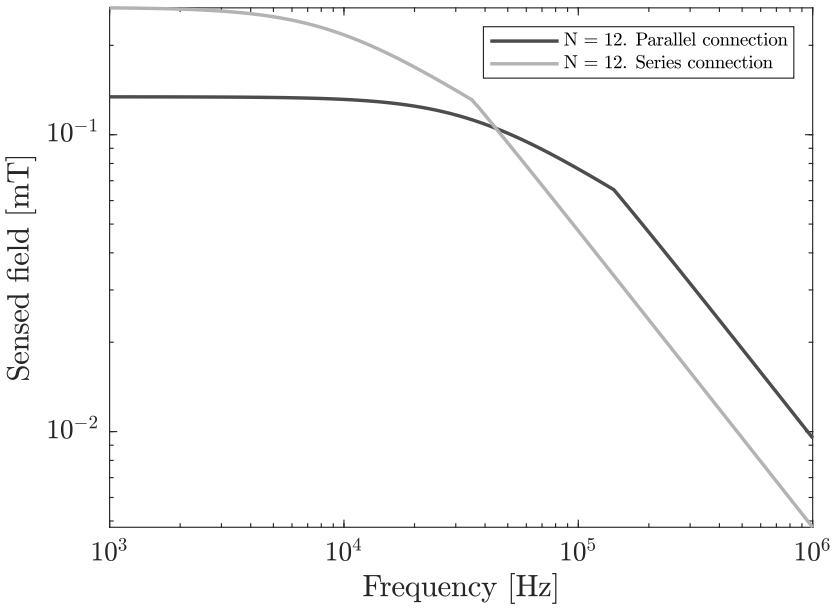

Figure 2.14: Maximum field that can be obtained if the connection of the two coils is switched from series to parallel.

2.5 Summary

The characterisation of magnetic field sensors needs an instrument capable of generating an analytically known and highly homogeneous magnetic field. It was chosen to use two coils paired in a Helmholtz coil configuration.

This chapter gave an overview of the electromagnetic theory at the basis of Helmholtz coil operational principle. The configuration is of easy realisation, so it was chosen to build a custom Coil. The desired performances and the constraints of the power supply circuit were considered in the design procedure, which was aimed to find the best configuration for the specific application.

The custom Helmoltz coil was 3D printed and hand wound. Measurements confirmed the values of resistance and inductance expected. Inductive behaviour at the frequencies of interest was also demonstrated.

The final part of the chapter presented other possibilities for the supply circuit of the Helmholtz coil. These methods were considered but eventually not used, in favour of the less performant, but simpler, direct supply.

Bibliography

[1] Wikimedia Commons, *Helmholtz coils*, 2005. [Online]. Available: https://commons.wikimedia.org/wiki/File:Helmholtz_coils.png.

[2] M. Zahn, 'Chapter 5: the magnetic field', in *RES.6-002 Electromagnetic Field Theory: A Problem Solving Approach*, Spring, Massachusetts Institute of Technology: MIT OpenCourseWare, 2008, pp. 313–392. [Online]. Available: https://ocw.mit.edu.

[3] C. R. Paul, *Inductance*. Hoboken, NJ, USA: John Wiley & Sons, Inc., Dec. 2009, pp. 1–379, ISBN: 9780470561232. DOI: 10.1002/9780470561232. [Online]. Available: http://doi.wiley.com/10.1002/9780470561232.

[4] J. D. Jackson and R. F. Fox, 'Classical Electrodynamics, 3rd ed .', *American Journal of Physics*, vol. 67, no. 9, pp. 841–842, 1999, ISSN: 0002-9505. DOI: 10.1119/1.19136. [Online]. Available: http://aapt.scitation.org/doi/10.1119/1.19136.

[5] H. A. Wheeler, 'Simple Inductance Formulas for Radio Coils', *Proceedings of the Institute of Radio Engineers*, vol. 16, no. 10, pp. 1398–1400, 1928.

[6] Waveform, *Keysight Technologies 33500B Series Waveform Generators*. [Online]. Available: https://literature.cdn.keysight.com/litweb/pdf/5991-0692EN.pdf.

[7] Siglent, *Power Amplifier SPA1010*. [Online]. Available: https://www.siglent.eu/spa1010-10watt-power-amplifier.html.

[8] *High frequency Helmholtz coils generate magnetic fields*. [Online]. Available: https://passive-components.eu/high-frequency-helmholtz-coils-generates-magnetic-field/ (visited on 30/05/2019).

[9] Sensitec, *AFF755B*, 2015. [Online]. Available: https://www.sensitec.com/fileadmin/sensitec/Service_and_Support/Downloads/Data_Sheets/AFF700_800/SENSITEC_AFF755B_DSE_06.pdf.

[10] *AC Magnetic Field Generator Uses New Resonant*. [Online]. Available: https://www.accelinstruments.com/Applications/WaveformAmp/Magnetic-Field-Generator.html (visited on 30/05/2019).

Chapter 3

Inductive sensor design

Inductive sensors operate on the principle of Faraday's law, where the induced voltage in a coil is proportional to the negative time derivative of the flux linked by that coil. If the geometrical and physical parameters are known, it is possible to use the measured voltage to determine the average flux perpendicular to the sensor area.

To date, EMT sensors, such as those shown in Figure 3.1, are commercially manufactured to specified sensitivities in fixed geometries. However, with the increasing prevalence of EMT across image-guided interventions, the need for flexible sensor geometries and sensitivities has become more important. In some applications, such as laparoscopic instruments and endoscope tracking, the large instrument diameter (6-12 mm) allows new ergonomic sensor geometries, based on a coil wound around the instrument itself.

A number of inductive sensors were designed, built, tested and integrated in Anser EMT system. The aim was to demonstrate that a custom inductive sensor can be easily built by winding a coil, to verify some simple equations useful to the design of bespoke sensors and to determine what are the main parameters affecting inductive sensor sensitivity and accuracy.

This chapter presents the materials and dimensions of the sensors developed, the measurement setup, the results of sensitivity over frequency and of static accuracy testing.

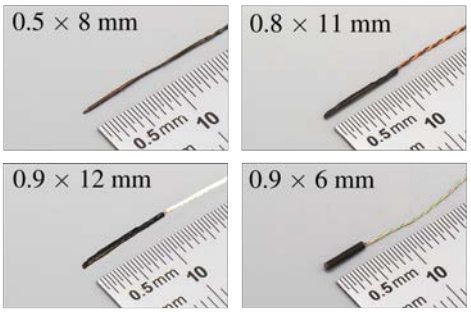

Figure 3.1: Commercially available EMT inductive sensors (Aurora Sensors [1]).

Coil	N	l_c [mm]	d_i [mm]	d_o [mm]	d_w [mm]	R [Ω]	L [μH] (Air)
A	321	12	9	12.5	0.19	7.4	604
B	319	12	11	14.1	0.19	8.6	804
C	120	12	9	12.2	0.32	0.8	91
D	216	12	9	11.4	0.19	9.4	425
E	417	12	9	12.0	0.15	14.3	1018

Table 3.1: Properties of EMT sensor coils designed and tested in this work.

3.1 Sensor design

A series of five inductive sensors were wound on custom Delrin formers. The parameters of each coil are summarised in Table 3.1, where N is the turn count, l_c is the coil length, d_i and d_o are respectively the inner and outer coil diameters, referred to the innermost and the outermost winding, and d_w is the wire diameter.

As stated in paragraph 1.3.3, the coil sensitivity k_s is expressed by Equation 3.1:

$$k_s = 2\pi N A_c \mu_a \quad \left[\frac{\mathrm{V}}{\mathrm{T\,Hz}}\right] \tag{3.1}$$

and has typical values for commercial inductive sensors of $0.1-0.2\,\mathrm{V\,T^{-1}\,Hz^{-1}}$. Considering an air-core coil with an average diameter of 10 mm, a sensitivity k_s of $0.15\,\mathrm{V\,T^{-1}\,Hz^{-1}}$ is obtained with about 300 turns. With Coil *A* as a baseline, Coil *B* increases the average area, while Coils *C*, *D* and *E* investigate changes in the number of turns. The characterisation of Coil *B* over frequency was also performed with the insertion of a ferrite core. The static accuracy of Coils *C*, *D* and *E* was also tested with a ferrite core. The aim was to investigate how the parameters N, A_c and μ_a affect the sensor sensitivity and verify the simplifications of Equation 3.1. For comparison, a commercial sensor with ferrite core [1], manufactured by NDI (*Northern Digital Inc., Waterloo, Canada*) was also tested.

Each coil was carefully hand wound, with visual inspection and photography used to confirm turn count upon completion of each layer. Figure 3.2 shows a typical completed winding layer. One turn of magnet tape was used to fix each layer upon winding. Each former could facilitate the insertion of a ferrite rod core. The final wound sensor coil was terminated with a twisted-pair cable. Ferrite cylinders were investigated as magnetic cores. They measured 12 mm in length and 6 mm in diameter and were made of 3C90 grade ferrite, with a relative permeability of $\mu_r = 2300$ [2].

3.2 Sensor characterisation

3.2.1 Instrumentation

An overview of the instruments used and the measurements taken to characterize the sensors is given.

The instruments used to generate a sinusoidal field and their main specifications are

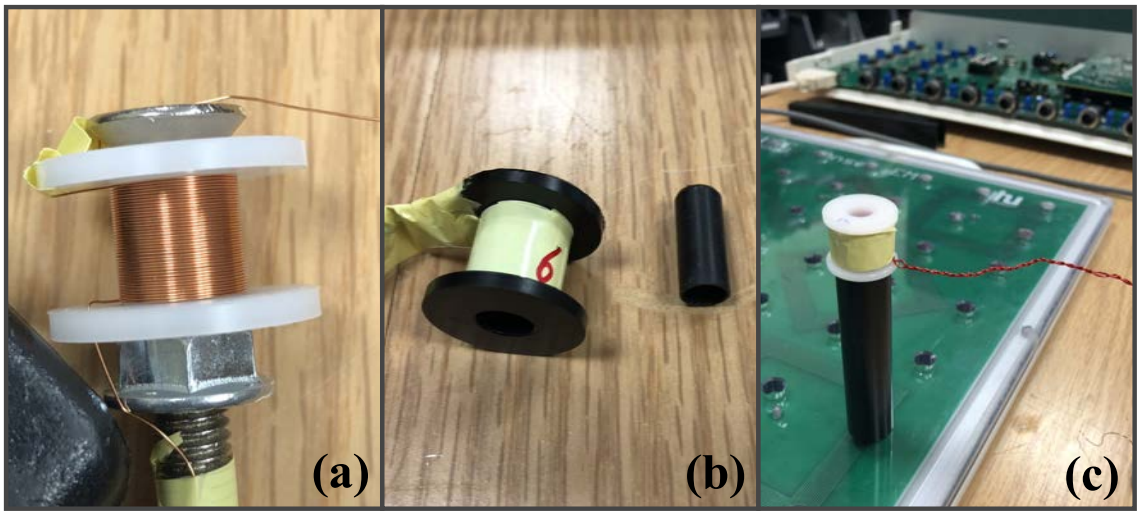

Figure 3.2: **(a)** Enamelled copper wire wound on the Delrin coil former.
(b) Each completed winding layer was secured with magnet tape. The removable ferrite core is also shown. The core may be inserted into the former lumen.
(c) The wound coil is located above the Anser EMT calibration board using the Delrin former during calibration and testing.

summarised here:

- A **waveform generator** (33500B Series, *Keysight Technologies, Santa Rosa, California* [3]) generated the sinusoidal voltage to supply the current to the Helmholtz coil. The maximum frequency is 20 MHz, well over the range of frequencies in which the sensors were analysed. Each of the two channels has an output resistance of 50 Ω, which is large compared to the internal impedance of the Helmholtz coil, so a power amplifier was necessary to drive the coil. The maximum waveform generator output voltage is of 20 Vpp (peak to peak).

- A **power amplifier** (SPA1010, *Siglent, Helmond, Netherlands* [4]) amplified the signal of the waveform generator. The high input impedance of 15 kΩ allows for full voltage amplification to get all the signal generated and to absorb few current. The linear operating limit input voltage is between ±6.5 V, a larger input voltage may also cause damage to the instrument. The output impedance is less than 2 Ω and the range of output voltage is limited to ±13 V. The bandwidth that assures no attenuation or distortion is above 1 MHz. There is a maximum output power of 10 W, over which the power amplifier short circuits and has to be turned off and electrically disconnected.

- The custom-designed **Helmholtz coil** described in chapter 2 generated the required field. The coil parameters are: diameter of 6 cm and 6 turns per coil, made of 1.5 mm width wire, hand wound and taped. The impedance is the series of a 0.12 Ω resistance and a 9 μH inductance.

- It was not possible to use a classical multimeter to measure the current because of the limited bandwidth of these instruments. A **current probe** (I-prober 520, *Thurlby*

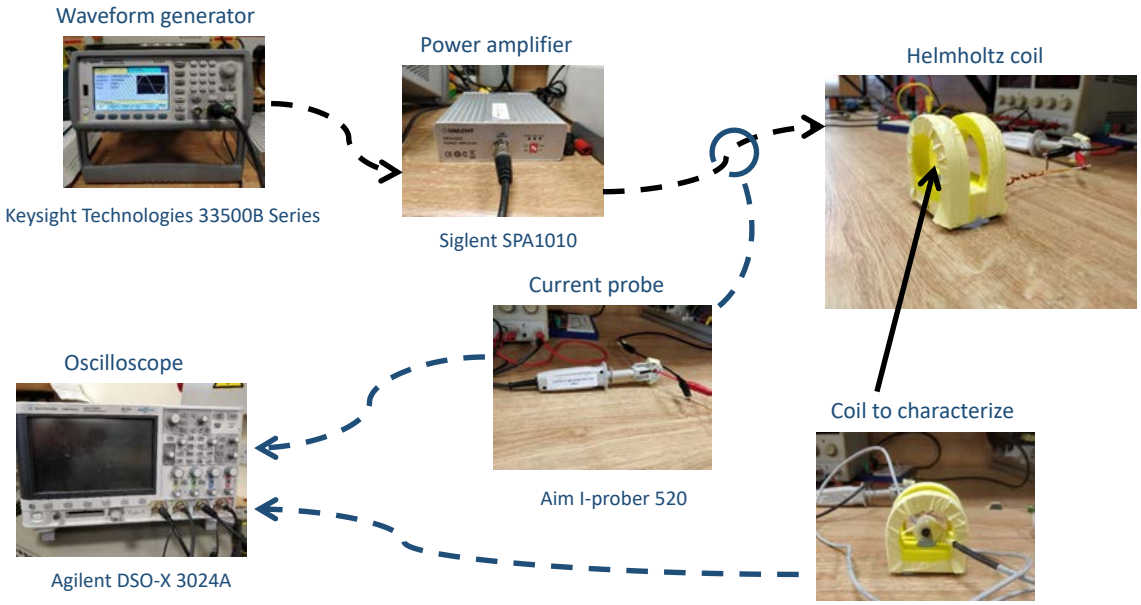

Figure 3.3: Conceptual diagram of the setup of the instruments used for the characterisation.

Thandar Instruments Ltd., Huntingdon, United Kingdom [5]) was chosen, with a wide bandwidth of DC to 5 MHz. The main disadvantage was that the measurement was not totally independent of the position and the orientation of the wire inside the closed-loop of the probe. To address this challenge, the current probe and the wire were fixed with tape to get a stable setting and the current was measured with the probe and with a multimeter (Fluke 45, *Fluke Corporation, Eindhoven, Netherlands* [6]) from 1 to 10 kHz (bandwidth of the multimeter). This calibration exercise identified a correction factor of 0.9805 to the raw current probe output across frequencies, which was used for all successive measurements with the probe.

- The sensor was connected to the oscilloscope (DSOX3024A, *Keysight Technologies, —* [7]) through a shielded cable, to reduce the disturbance noise and to avoid other magnetic fields linked to the wires from changing the measurement. The cable terminated in a miniXLR connector (RT5FC-B, *Neutrik, Schaan, Liechtenstein* [8]), for connection to the Anser EMT main system.

Figure 3.3 displays a sketch of the circuit used to generate and measure the field and the current.

3.2.2 Measurements

Both the voltage signals coming from the current probe and the sensor were visualized with the oscilloscope. The channels were coupled in AC, the trigger was in auto mode and the acquire mode was set to averaging with 16 points to remove the high frequency noise, affecting mostly the signal of the coil sensor. The waveforms obtained in this manner were very clean and undistorted, so the average RMS measured by the oscilloscope was taken as a measurement of the magnitude of the current and of the sensor output voltage.

From the measurement of the current, the field B_z at the position of the sensor at the centre of the Helmholtz coil was analytically known: see Equation 2.9. Changing the frequency from 1 kHz to above 1 MHz, the gain of the sensor was calculated by the ratio between the output signal in Volts and the magnetic field measured in Tesla, obtaining the experimental points of Figures 3.7 and 3.8.

Measurements were performed by the oscilloscope and saved to an external USB drive. A MATLAB script was used to grab the needed data from the resulting *.txt* files. The main commands used in the script are reported in Listing 3.1.

Listing 3.1: MATLAB script to read the data of the oscilloscope.

```
numFiles = 62;              % number of files to analyze
freq=zeros(numFiles+1,1);   % Inizialize vectors
...
for ff=0:numFiles
    fclose('all');
    nnf=ff;                 % to fit the number on the file name
    fid = fopen(['scope_data\scope_',num2str(nnf),'.txt'],'r');
                            % read the txt file
    while ~feof(fid)
        line = fgetl(fid);
        if contains(line,'Frequency(1)')
        % find the correct line corresponding to a measurement
            Cur = strfind(line,'Cur');   % find the data on that line
            Cur = Cur(1);
            freqarr = textscan(line(Cur+4:Cur+9),'%f');
        % select the number (measurement)
            freq(ff+1) = freqarr{1};     % fill the vector

        elseif contains(line,'Std Dev(1)')
        % do the same for other measurements
        ...
        end
    end
end

%% before saving check the vectors (units of measure can scale)
D=[freq field etc.];    % all vectors in a table
D=sortrows(D,1);        % in order of frequency
csvwrite('data.csv',D)  % all the data collected in a .csv file
```

3.2.3 Inductive sensor model

An inductive magnetic sensor is the series of many turns, each one introducing a series resistance. The self inductance of every turn and the mutual inductances between near turns can be modelled as distributed inductors, with an inductance value that takes into account the self and the mutual effects. Overall, any turn is the series connection of a resistor R_t and an inductor L_t, whose values are obtained by the total self resistance and inductance of the sensor divided by the number of turns. Between the turns exists parasitic capacitance C_t. In a simplified distributed circuit this effect can be modelled by shunt

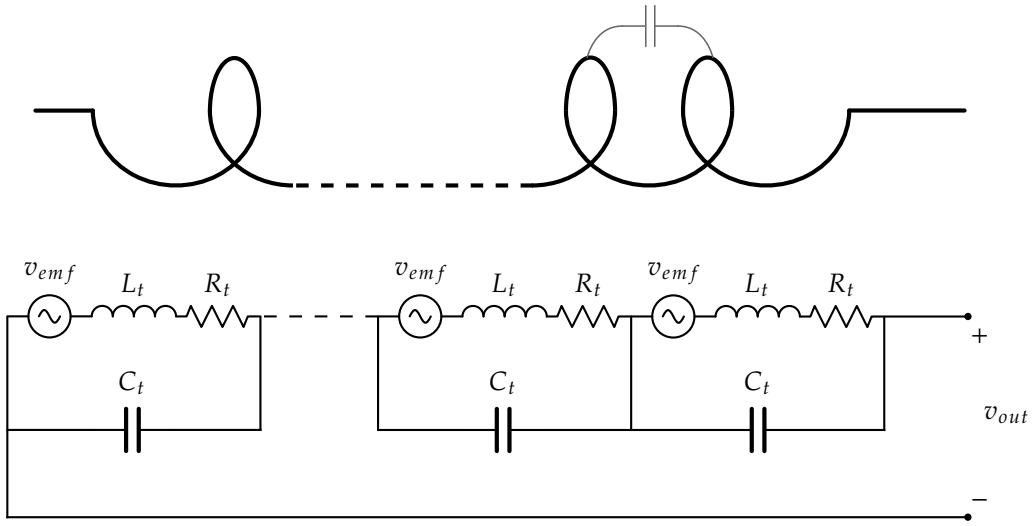

Figure 3.4: Schematic representation of an inductive sensor and consequent circuit model with distributed parameters.

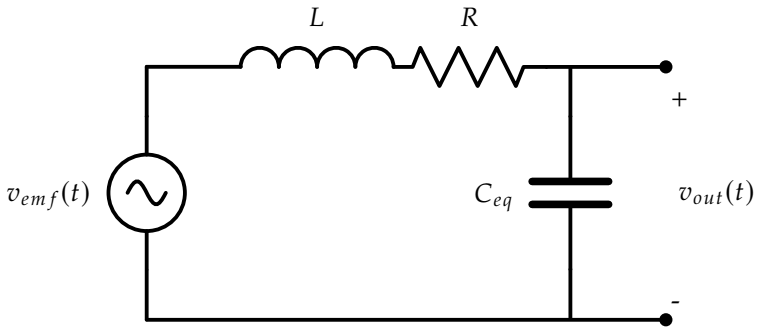

Figure 3.5: Lumped parameters circuit for an inductive sensor. v_{emf} is the voltage induced by the time-varying magnetic field, L and R are the sensor series inductance and resistance, C_{eq} is an equivalent lumped capacitor that takes into account the parasitic capacitance effects.

capacitors in parallel with each turn. Figure 3.4 shows the schematic representation of the coil and the described distributed parameters circuit.

At lower frequencies, more or less from DC to the first self-resonance frequency (SRF), it is possible to neglect the distributed effects of the parasitic capacitances and to consider a unique lumped shunt capacitance. The lumped parameters circuit then becomes an $L - R$ series with a shunt capacitor C_{eq}, as in Figure 3.5. C_{eq} is sometimes referred to as DC capacitance. It has to be remarked that C_{eq} is neither the series nor any combination of the capacitances of the distributed model. It is rather an equivalent capacitance valid to model the circuit up to the SRF. C_{eq} has to be chosen in the model so that the single resonance frequency f_0 of the lumped circuit, as defined in Equation 3.2, is equal to the first SRF of the distributed model:

$$f_0 = \frac{1}{2\pi\sqrt{LC_{eq}}} \quad [\text{Hz}] \tag{3.2}$$

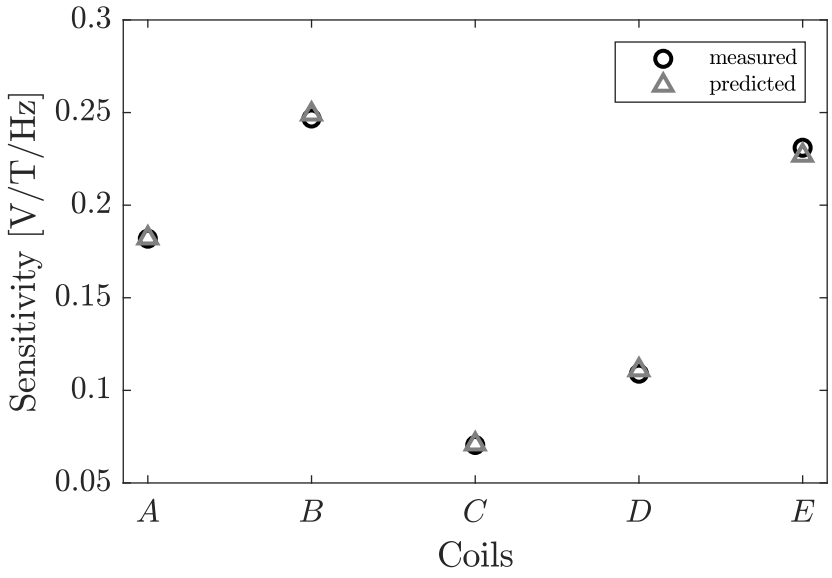

Figure 3.6: Comparison between the experimental sensitivity k_s and the one predicted by Equation 3.1.

As explained in paragraph 1.3.3, the induced voltage V_{emf} is proportional to the external sinusoidal field perpendicular to the coil area:

$$V_{emf} = -jk_s f B_\perp \quad [\text{V}] \tag{3.3}$$

where V_{emf} and B are phasor quantities. With reference to Figure 3.5 and considering Equation 3.3, the output voltage of the sensor is expressed by Equation 3.4, with $\omega = 2\pi f$:

$$V_{out} = \frac{-jk_s f B_\perp}{1 - \omega^2 LC + j\omega RC} \quad [\text{V}] \tag{3.4}$$

3.2.4 Results

The measurements were fitted in a least-squares sense at low frequency to $|V_{out}| \approx |V_{emf}| = k_s f |B_\perp|$, to determine the value of the sensitivity k_s. The results for each coil are reported in Tables 3.3 and 3.4 of paragraph 3.3.2. Figure 3.6 compares the sensitivities measured to those predicted by Equation 3.1.

With reference to the model of Figure 3.5, R and L were measured for each coil with an impedance analyser, the SRF f_0 was identified by the maximum output voltage of the measured points and C_{eq} was consequently defined by Equation 3.5:

$$C_{eq} = \frac{1}{(2\pi f_0)^2 L} \quad [\text{F}] \tag{3.5}$$

This procedure was used to identify all the parameters of Equation 3.4 and to fit the experimental data, for the five custom-wound sensor coils and for the NDI sensor presented in section 3.1. Coil B was also tested with ferrite core.

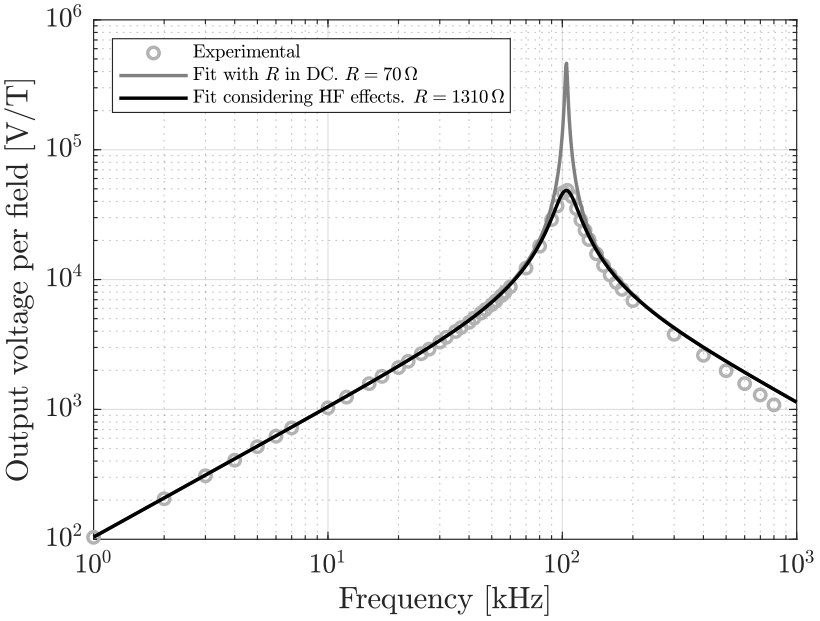

Figure 3.7: Ratio between the measured voltage and the input field, over the frequency, for the NDI sensor. The resulting sensitivity is $k_s = 0.1040\,\mathrm{V\,T^{-1}\,Hz^{-1}}$. Comparison between the fit using the values of R and L measured in DC and the fit where the correction for skin and proximity effect were considered.

For the NDI sensor, Figure 3.7 shows that the mathematical model can accurately predict the behaviour of the sensor over frequency. The resulting sensitivity is $k_s = 0.1040\,\mathrm{V\,T^{-1}\,Hz^{-1}}$. The overshoot at the SRF is higher in the curve obtained by fitting than in the experimental data, because the resistance used in the model was measured at DC, but at higher frequencies its value is bigger, due to skin and proximity effects. Figure 3.7 shows also the fit where the resistance which better fitted the data was considered. Formulas for skin and proximity effects could not completely explain all the increment of the value of the resistance at higher frequency. However, in the design of inductive sensors only the linear behaviour at lower frequencies is of interest, so further investigation on how to predict the peak at SRF was not made.

Similar results were obtained for the other coils and are presented in Figure 3.8, which shows the experimental data and the fitting curves for all five coils with air core and for Coil B also with ferrite core. All these plots present an initial straight line, where the output voltage is proportional to the frequency (slope of +20 dB/dec) and the vertical shift depends on the coil sensitivity k_s. A resonance peak is clearly seen, where the output voltage has a maximum because of the resonance between the inner inductance of the sensor and the parasitic capacitances. Beyond the SRF, the fitting curve begins to deviate from the measured data, due to the approximations in the lumped model, which is not accurate at frequencies over the SRF. This characteristic is typical for any inductive sensor. The behaviours of the coils over frequency were compared using the curves obtained by fitting.

Figure 3.9 shows Coils A and B, with almost the same number of turns N but different

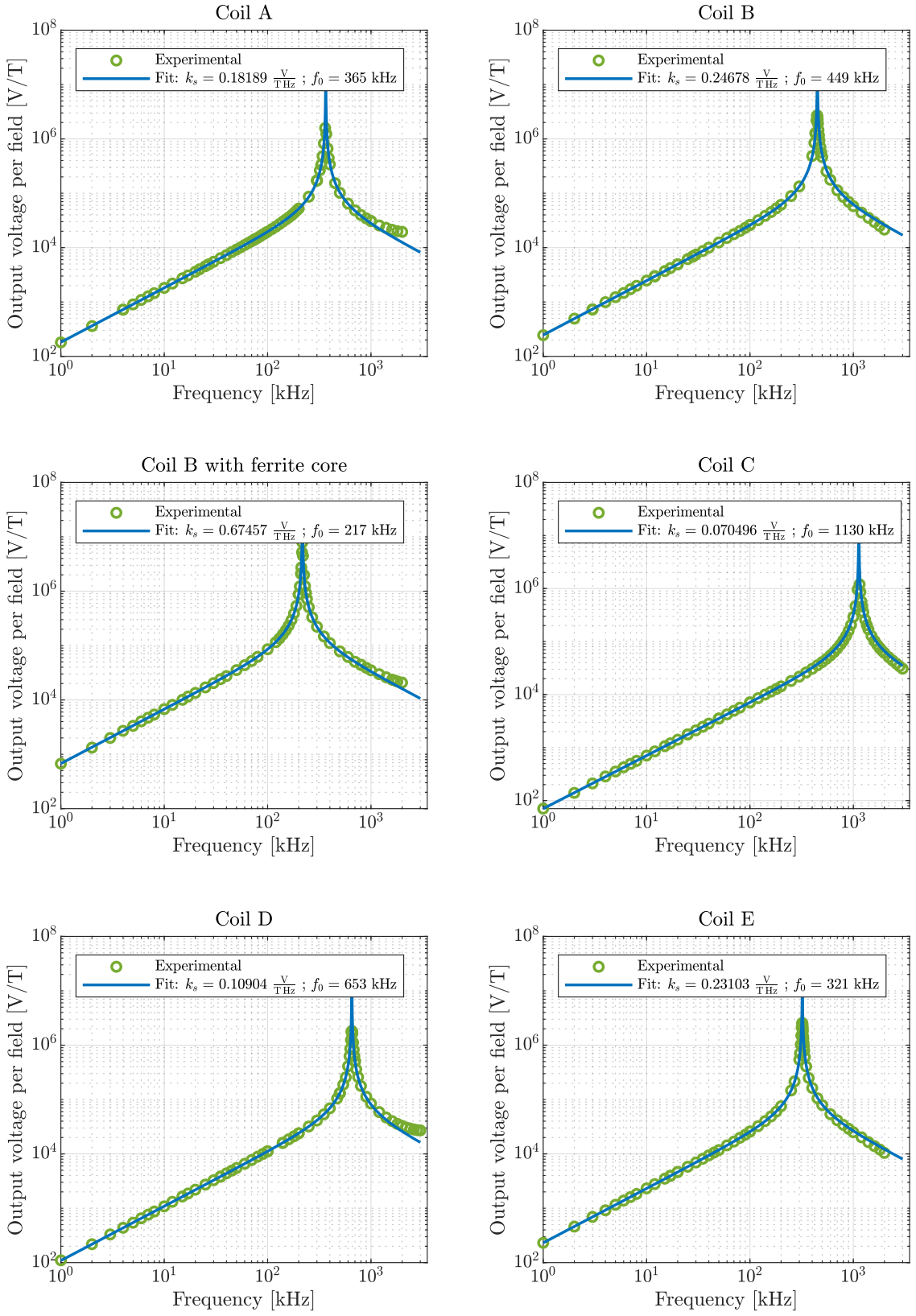

Figure 3.8: Characterisation of the five coils and of Coil *B* with a ferrite core. The experimental points (green circles) are fitted (blue line) with the model described by Equation 3.4.

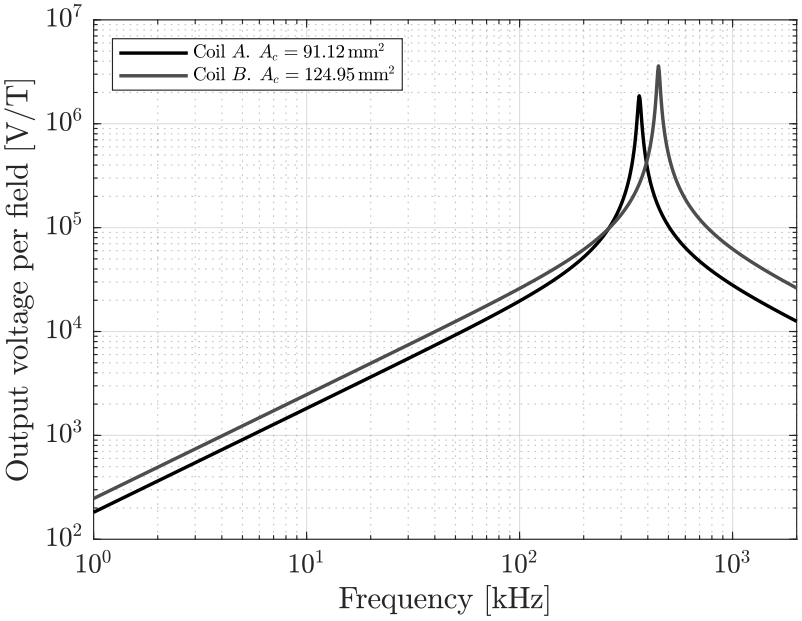

Figure 3.9: Behaviour of Coils A and B over frequency. Varying parameter: A_c.

areas. Considering Coil A as a reference, Coil B, with larger area, has an increased sensitivity k_s. The SRF (Equation 3.2) is higher for Coil B, due to a smaller value of parasitic capacitance, since L is very similar, as stated in Table 3.1. It should be noted that, for graphing in a logarithmic scale, a larger value of k_s results in a translation of the straight line and the slope is always of +20 $^{dB}/_{\mathrm{dec}}$.

Figure 3.10 shows Coils A, C, D and E, where the turns N (refer to Table 3.1) are changed. In this case, when N increases the sensitivity k_s increases too and the SRF decreases, due to a larger value of inductance.

The characterisation of Coil B was performed with and without the presence of a ferrite core. The resulting sensitivities were of $k_s = 0.2468\,\mathrm{V\,T^{-1}\,Hz^{-1}}$ in the case of air core and of $k_s = 0.6746\,\mathrm{V\,T^{-1}\,Hz^{-1}}$ in the case of magnetic core. The insertion of the core increased the apparent permeability μ_a (see paragraph 1.3.3) by a factor of 2.73. This can be observed also in Figure 3.11, with a gap between the two graphs of approximately 10 dB.

3.2.5 Effect of ferrite core

The effect of ferrite core on the apparent permeability μ_a described in paragraph 1.3.3 was further investigated.

Analytical expressions to predict μ_a are found in literature. In [9] the following formula is reported:

$$\mu_a = \frac{\mu_r}{1 + k_d(\mu_r - 1)} \tag{3.6}$$

where μ_r is the manufacturer-supplied relative permeability and k_d is the geometry-specific demagnetisation factor. The demagnetizing factor k_d for a core of length l_c and diameter

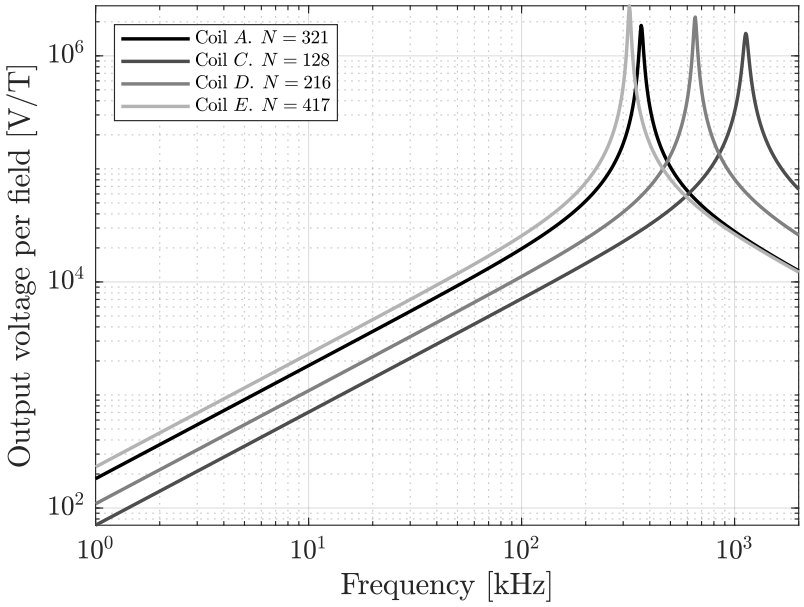

Figure 3.10: Behaviour of Coils A, C, D and E over frequency. Varying parameter: N.

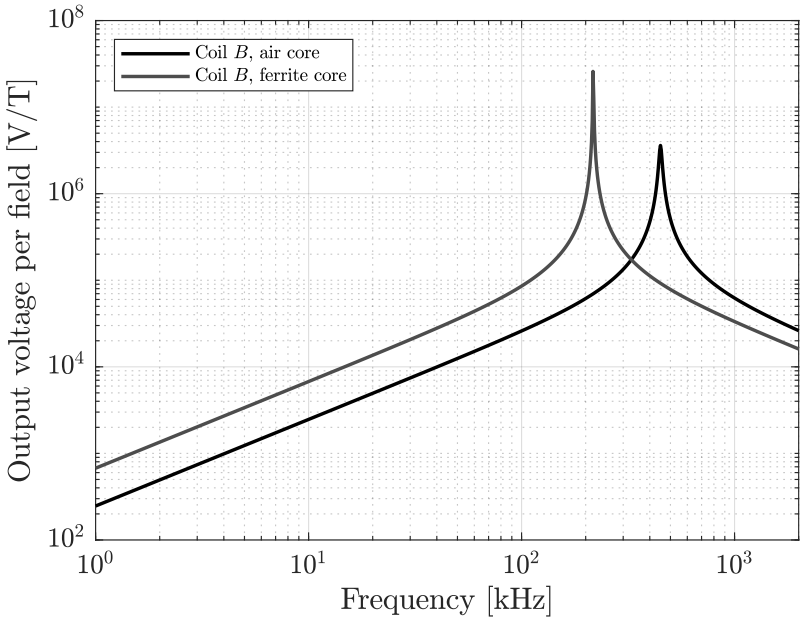

Figure 3.11: Behaviour of Coil B over frequency. Varying parameter: μ_a.

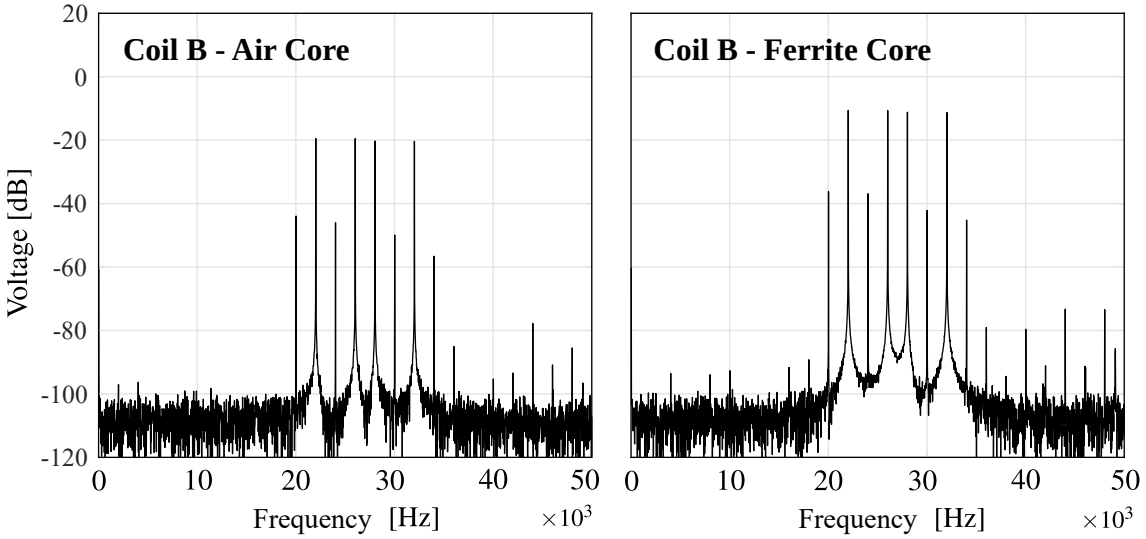

Figure 3.12: Discrete Fourier Transform of the sensed voltage in Coil B with air and ferrite cores. Voltage units are in decibels (dB) with respect to 1 Volt.

D_c may be estimated using Parker's equation [10]:

$$k_d \approx \frac{d_c^2}{l_c^2}\left(\ln\frac{2l_c}{d_c} - 1\right) \tag{3.7}$$

The longer the core is in relation to its diameter, the lower the demagnetisation factor. Closed magnetic structures such as toroidal cores have a demagnetisation factor of $k_d = 0$. Using the core dimensions and permeability reported in section 3.1, Equation 3.6 leads to an apparent magnetic permeability $\mu_a \approx 12.3$. Recent work [11] indicates that for $l_c/d_c \approx 2$, Parker's equation may significantly underestimate k_d and a value of 0.2 is correct. This would decrease the apparent magnetic permeability to $\mu_a \approx 5$.

The characterisation of Coil B with ferrite core provided a sensitivity increased by a factor of 2.73, showing that the formulas proposed by literature are not accurate for the coil sensors studied in this work. The same effect is also demonstrated in the results of Figure 3.12, which shows the Discrete Fourier Transform of the sensor voltage at a fixed position $(x, y, z) = (0, 0, 85)$ mm from the centre of the Anser EMT board described in section 1.3. Each voltage peak corresponds to the induced voltage due to one of the eight transmitting coils of the field generator. The plot shows that the ferrite core increased the sensor voltage by approximately 10 dB for the four transmitters located closest to the centre of the board.

The role of the ferrite core was measured with a gaussmeter (GM08, *Hirst Magnetic Instruments Ltd, Falmouth, United Kingdom* [12]). The core was placed at the centre of the custom Helmholtz coil used for characterisation, as shown in Figure 3.13. The Helmholtz coil was supplied with a steady DC current of 2.047 A, measured by the Fluke 45 multimeter

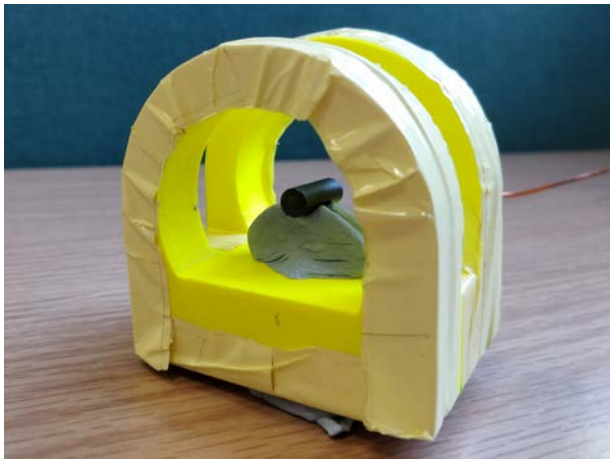

Figure 3.13: The apparent permeability μ_a was calculated by measuring the B field on the surface of the core placed inside the known H field generated by the Helmholtz coil.

[6]. From Equation 2.9, the H field at the centre of the coils was of:

$$H_z = \left(\frac{4}{5}\right)^{3/2} \frac{6\ (\text{turns})}{3{\times}10^{-2}\ (\text{radius [m]})} 2.047 = 292.9\ \frac{\text{A}}{\text{m}} \tag{3.8}$$

This value was also confirmed by measurement of the gaussmeter in the absence of the core and considering air permeability μ_0. With the ferrite core placed at the centre of the Helmholtz coil, the gaussmeter measured a magnetic field of approximately 10 G on the external surface of the core. This can be assumed to be equal to the field inside the core, being the normal component of the B field continuous across interfaces. The resulting apparent permeability is then given by Equation 3.9:

$$\mu_a = \frac{10{\times}10^{-4}}{\mu_0 292.9} = 2.72 \tag{3.9}$$

which corresponds closely with the value determined in paragraph 3.2.4 using sensitivity data.

Another way to calculate the increment of the apparent permeability is by the measurement of the inductance L. By definition, L is the flux linked to the coil generated by an unit current flowing in the coil itself. The addition of a ferromagnetic core increases the linked flux almost by the same factor both when the field is generated externally (*i.e.* by the Helmholtz coil) and when it is due to the current in the coil (in the second case the increment is slightly smaller, because of the presence of more flux lines that do not link all the turns).

The inductance of Coil B was measured with and without ferrite core. It resulted: $L_{air} = 786\,\mu\text{H}$ and $L_{ferrite} = 2102\,\mu\text{H}$, meaning that the insertion of the core increased the inductance L by a factor of 2.67. The correctness of the measured value of the air core inductance was confirmed by Wheeler's formula [13], already presented in Equation 2.19. With the measures of Coil B reported in Figure 3.14, Wheeler's formula gives $L_{air} = 778.4\,\mu\text{H}$.

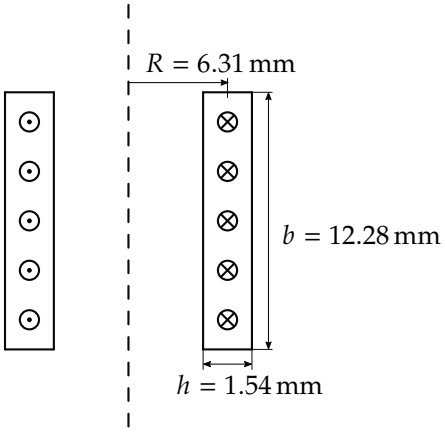

Figure 3.14: Measures of Coil B.

	air core	ferrite core	μ_a
Gaussmeter	292.9 A/m	10 G	2.72
Sensitivity	0.2468 V T^{-1} Hz^{-1}	0.6746 V T^{-1} Hz^{-1}	2.73
FFT	/	+10 dB	≈ 3
Measured L	786 µH	2102 µH	2.67
Simulated L	790 µH	1894 µH	2.49
Pugh *et al.* [11]	/	/	5

Table 3.2: Apparent permeability μ_a computed with different methods.

FEMM [14] was used to simulate the inductance of Coil B, with and without ferrite core, as it is shown in Figures 3.15 and 3.16. It resulted in $L_{air} = 790$ µH and $L_{ferrite} = 1894$ µH, meaning that the insertion of the core increased the inductance by a factor of 2.39. The value of $L_{ferrite}$ predicted numerically is slightly smaller than the measured value of 2102 µH, but the range is confirmed.

The results of the different methods used to investigate the effect of the ferromagnetic core are summarised in Table 3.2.

The presence of the core also increased the value of parasitic capacitances. From Figure 3.11, it can be noticed that the SRF of Coil B decreased from 449 (air core) to 217 kHz (ferrite core), such that:

$$\left(\frac{449}{217}\right)^2 = \left(\frac{f_{0\,air}}{f_{0\,ferrite}}\right)^2 = \frac{L_{ferrite}C_{ferrite}}{L_{air}C_{air}} = 2.67\frac{C_{ferrite}}{C_{air}} \tag{3.10}$$

where 2.67 is the measured ratio $L_{ferrite}/L_{air}$. Therefore, the parasitic capacitances increased by a factor of about:

$$\frac{C_{ferrite}}{C_{air}} = \left(\frac{449}{217}\right)^2 \frac{1}{2.67} = 1.6 \tag{3.11}$$

This is explained by the fact that the ferrite core can conduct current and so there is a new capacitance between the turns and the core, which adds up to the capacitance between the turns.

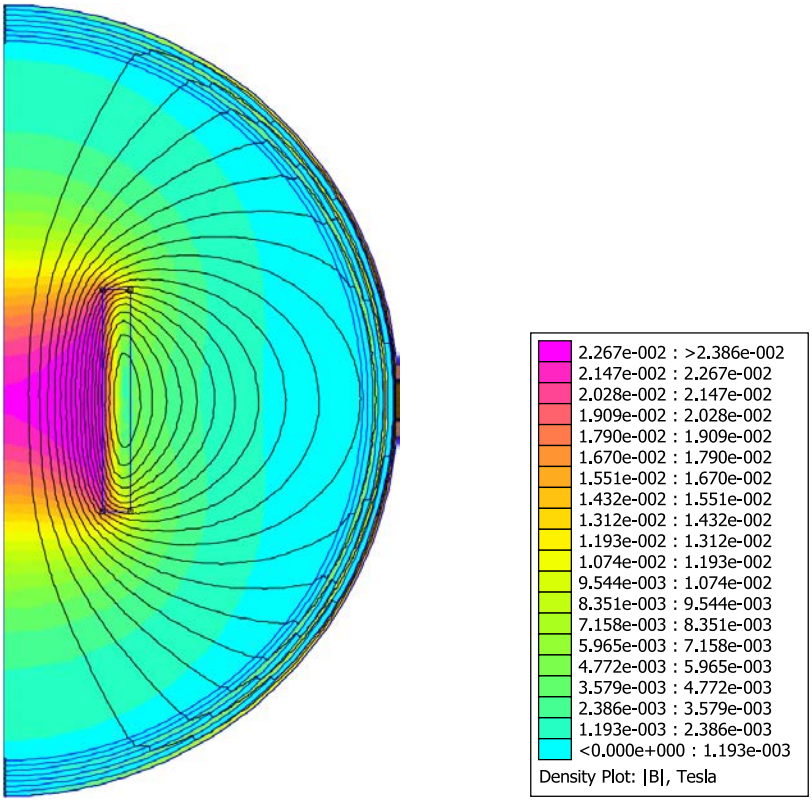

Figure 3.15: FEMM simulation of Coil *B* with air core.

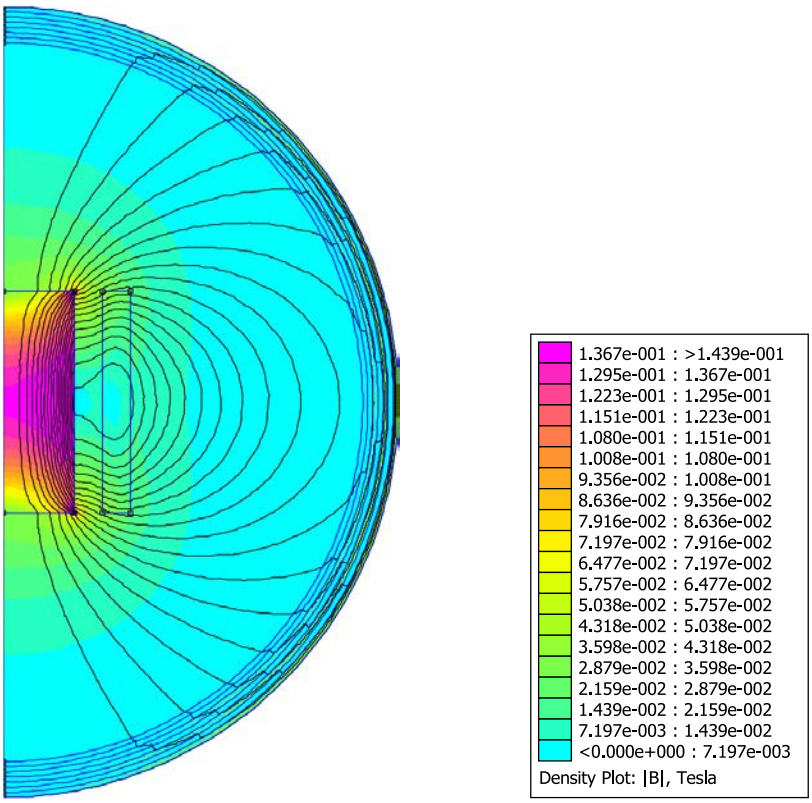

Figure 3.16: FEMM simulation of Coil *B* with ferrite core.

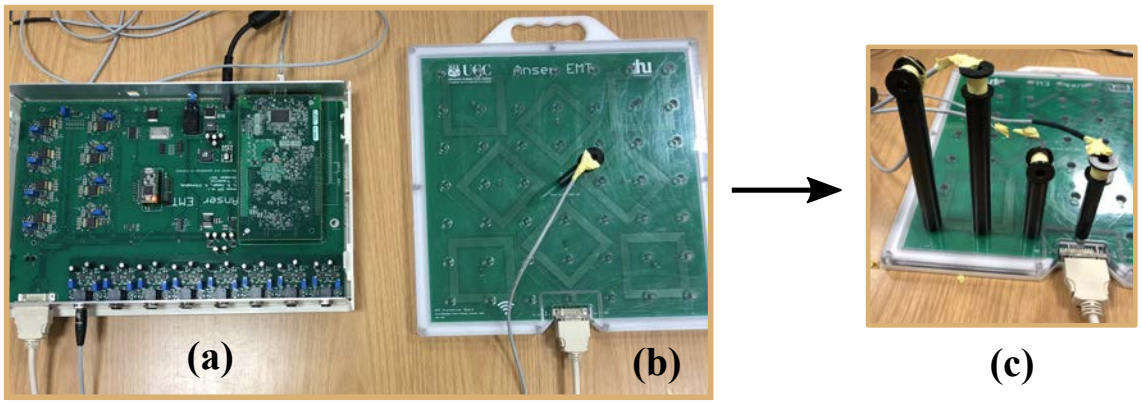

Figure 3.17: **(a)-(b)** Anser EMT base station and field generator used in experiments. To conduct static accuracy test, sensor coils were inserted in the equispaced holes of a 49 point grid. **(c)** Delrin formers of two heights were used in experiments. 49 position measurements were recorded with each former resulting in a total of 98 measurements per coil.

3.3 Static accuracy

The static accuracy test was performed by Oisín McVeigh[1]. With his permission, I used the data to draw the graphs of this section and to get some useful results in conjunction with the data presented in the previous section 3.2.

3.3.1 Sensor calibration

Each sensor was calibrated for use with the Anser EMT system, using the model-fitting routine described in section 1.3. For five degree of freedom sensors calibration, the coil is positioned at a fixed distance and orientation (z-oriented) relative to the transmitter, as shown in Figure 3.17. The measured sensor magnetic flux at each point is compared to the modelled flux to get a scaling constant κ, which minimises the error between the measured Φ_{meas} and the modelled Φ_{model} flux in the sensor in a least-squares sense, as given by Equation 3.12:

$$\min_{LS} \left\{ \frac{1}{\kappa} \cdot \Phi_{meas} - \Phi_{model} \right\} \tag{3.12}$$

3.3.2 Static accuracy test

The five coils and the NDI sensor were tested for static positional accuracy, following calibration. Each sensor coil was placed z-directed on the 49 points grid shown in Figure 3.17, at fixed heights of 85.6 and 152 mm above the field generator board, for a total of 98 points. The average error between the position reconstructed by the sensor measurement and the known position of the test points is an estimation of the accuracy and the precision of the sensor. In general, it can be expected that points further from the centre of the transmitting board will give rise to the largest errors in position accuracy. Indeed, the nearer the sensor is to the magnetic field source, the larger the magnetic flux and the

[1]University College Cork, Ireland. https://orcid.org/0000-0002-4794-897X

output signal are, increasing the signal-to-noise ratio, with a resultant improvement in accuracy.

Static accuracy was determined by calculating the standard deviation (SD) between the reported sensor positions and the absolute positions of the sensor above the field generator, *i.e.* the expected values. Equation 3.14, reported for σ_x but evaluated similarly for σ_y and σ_z, was used to calculate the volume-averaged RMS error along each axis of the reference system:

$$\Delta x^i = |x^i_{meas} - x^i_{ref}| \tag{3.13}$$

$$\sigma_x = \sqrt{\frac{1}{P}\sum_{i=1}^{P}(\Delta x^i)^2} \tag{3.14}$$

where x^i_{meas} is the measured x position, x^i_{ref} is the absolute x coordinate of the i^{th} point and $P = 98$ is the total number test-points. The volume-averaged total RMS error (E_{RMS}) was obtained by vector addition of the SD in each direction (Equation 3.15), equivalent to the SD of the total distance error between measured and reference positions at each experimental point (Equation 3.16), considering null the expected value of the error:

$$E_{RMS} = \sqrt{\sigma_x^2 + \sigma_y^2 + \sigma_z^2} = \sqrt{\frac{1}{P}\sum_{i=1}^{P}(r^i)^2} \tag{3.15}$$

where r^i is the total error made at point i, in the sense of distance:

$$r^i = \sqrt{(\Delta x^i)^2 + (\Delta y^i)^2 + (\Delta z^i)^2} \tag{3.16}$$

Figure 3.18 shows the total position error at each point r^i as a function of distance from the origin of the FG, for Coils A and B. The results are summarised in Table 3.3, which includes the different coil effective areas A_c available for flux linkage (as given by Equation 1.22 of paragraph 1.3.3). Each coil has approximately equal turn count as noted in Table 3.1 and these coils were used to investigate the effect of increasing A_c on positional accuracy. No ferrite cores were used with Coils A or B.

Figure 3.19 shows the total position error r^i for Coils C, D and E, in the absence of any ferrite core. The results are summarised in Table 3.4 which includes the different turn counts N. In this case, each coil has approximately equal core area A_c and the aim was to investigate the effect of increasing N on positional accuracy, in the absence of ferrite cores.

Figure 3.19 also shows the effect of inserting into Coils C, D and E the 3C90 ferrite core mentioned in section 3.1. For comparison, the NDI sensor was also tested for static accuracy (Figure 3.20). The results are summarised in Table 3.5.

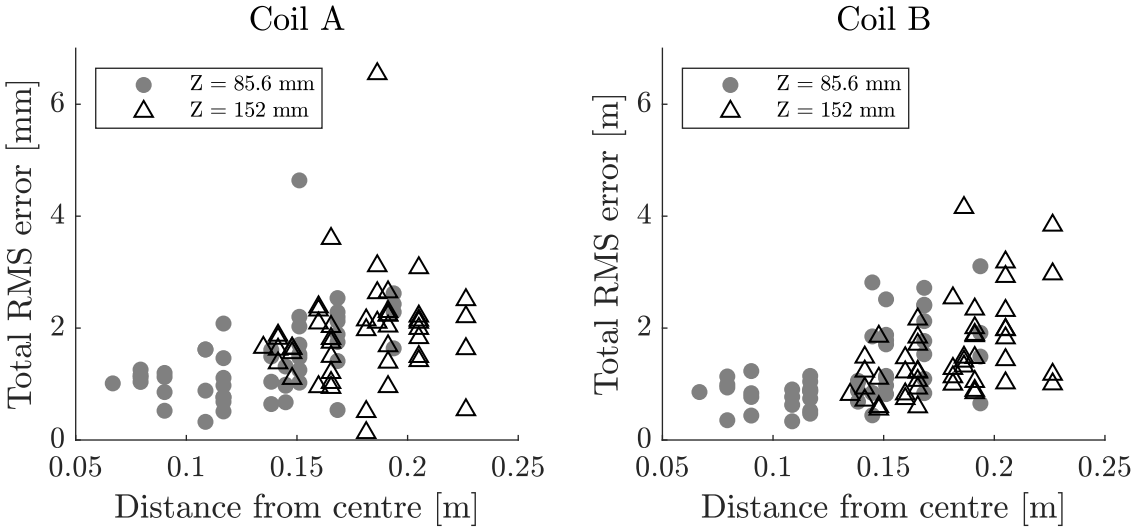

Figure 3.18: Error plots for coils A and B, at different distances from the centre of the transmitter board.

Coil	A_c [mm^2]	σ_x [mm]	σ_y [mm]	σ_z [mm]	E_{RMS} [mm]	$k_s \left[\frac{\text{V}}{\text{THz}}\right]$
A	90.7	1.05	1.23	0.97	1.89	0.1819
B	123.7	0.86	0.99	0.90	1.59	0.2468

Table 3.3: Static accuracy of coils A and B, with air-cores.

Coil	N	σ_x [mm]	σ_y [mm]	σ_z [mm]	E_{RMS} [mm]	$k_s \left[\frac{\text{V}}{\text{THz}}\right]$
C	120	1.57	1.50	1.52	2.48	0.0705
D	216	1.14	1.08	1.26	1.98	0.1090
A	321	1.05	1.23	0.97	1.89	0.1819
E	417	0.99	1.09	0.84	1.70	0.2310

Table 3.4: Static accuracy of coils C, D, A and E, with air-cores.

Coil	N	σ_x [mm]	σ_y [mm]	σ_z [mm]	E_{RMS} [mm]
C	120	1.04	0.89	1.31	1.90
D	216	1.13	0.73	0.91	1.62
E	417	0.86	1.04	0.81	1.58
NDI	/	1.19	1.12	0.73	1.79

Table 3.5: Static accuracy of coils C, D and E, with ferrite cores. Comparison with the NDI sensor. The number of turns of the NDI coil is unknown.

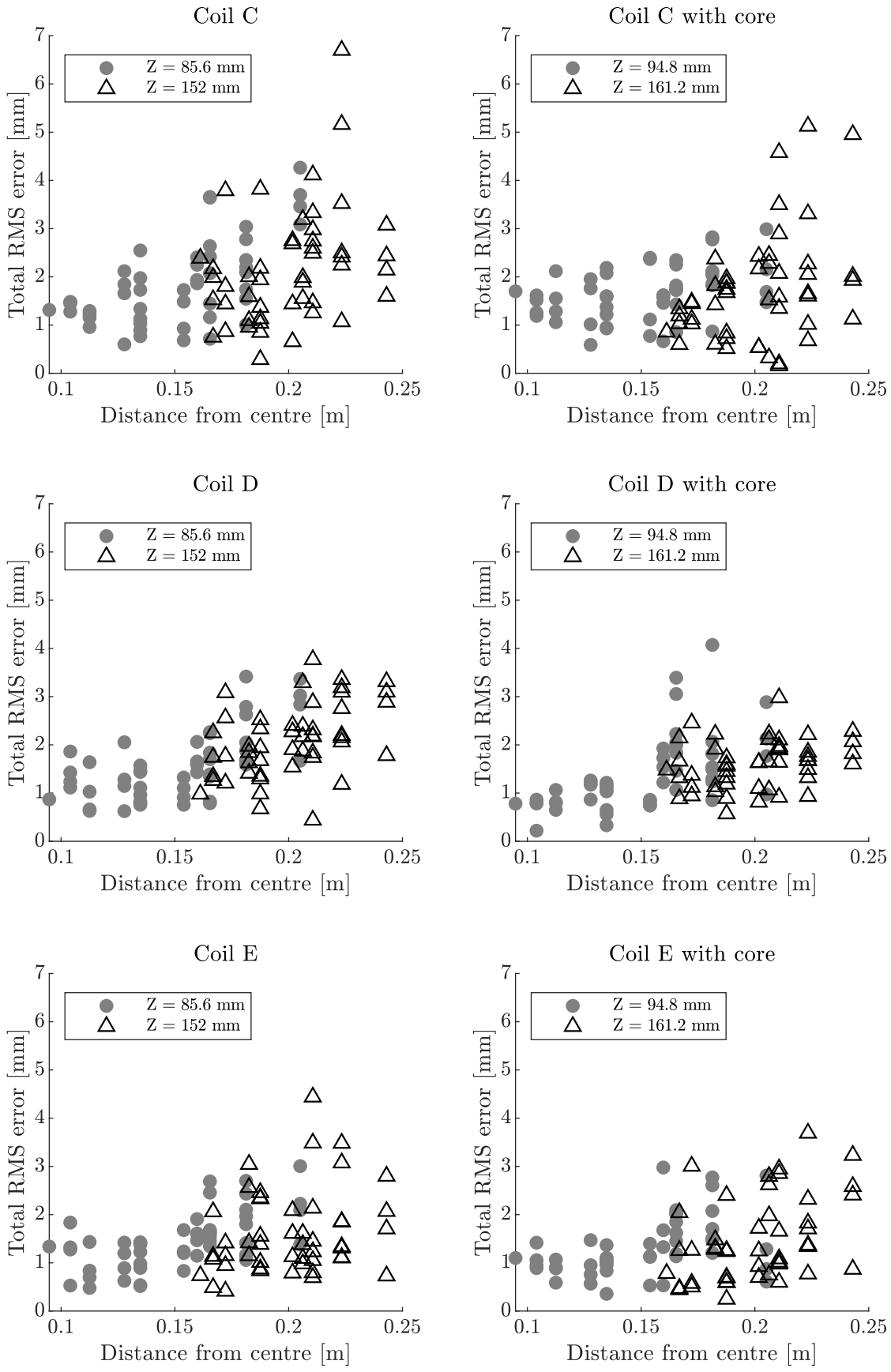

Figure 3.19: Error plots for coils *C*, *D* and *E* with and without ferrite cores, at different distances from the centre of the transmitter board.

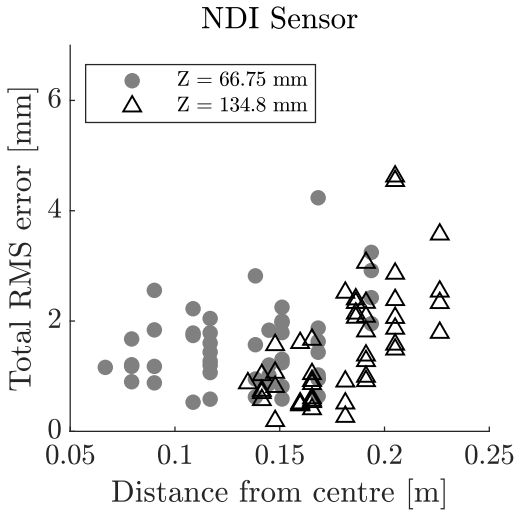

Figure 3.20: Error plots for the NDI coil, at different distances from the centre of the transmitter board.

3.3.3 Discussion

Static accuracy measurements were completed for each air-core coil and, in the case of Coils *C*, *D*, and *E*, the results were compared to the case with the addition of a ferrite core.

Table 3.3 details the effect of increasing the coil area A_c on total tracking error. A larger A_c results in a significant improvement of the total tracking accuracy, because the induced voltage increases and is measured more accurately. With respect to Coil *A*, the increment of area of Coil *B* is of 36.38 % and the sensitivity results increased of 35.68 %. Care needs to be taken in the numerical calculation of the expected *B* field through the sensor, to account for spatial variations across the area A_c.

The results of Table 3.3 show the effect of turn count N on tracking accuracy. As N increases, the total tracking error decreases. Considering Coil *C* as a baseline, with $N = 120$ and $k_s = 0.0705\,\mathrm{V\,T^{-1}\,Hz^{-1}}$, Coils *D*, *A* and *E* increased N of 80, 167 and 247 % respectively, yielding larger sensitivities of 54.61, 158 and 228 %. It should be noted that N also increases the value of the inductance and parasitic capacitances, lowering the bandwidth of the sensor, as given by Equation 3.2. Moreover, a longer winding wire has a larger resistance and this increases the thermal noise.

The addition of a magnetic core to the coil improved tracking accuracy in the case of all 3 coils. The comparison between Table 3.4 and Table 3.5 shows a reduction in the total RMS error of 0.58, 0.36 and 0.12 mm (*i.e.* 23.4, 18.2 and 7.1 %) for Coils *C*, *D* and *E* respectively, in the presence of the ferrite core.

To summarise, the increment of area, the addition of turns and the insertion of a ferrite core have all shown to decrease the total tracking error (Equation 3.15). This might be expected, because A_c, N and μ_a are all parameters that increase the sensor sensitivity, as given by Equation 3.1, and therefore the signal-to-noise ratio, with a resultant improvement in tracking accuracy. Figure 3.21 shows the plot of the total RMS error E_{RMS} of each coil versus the coil sensitivity k_s. While the dataset is too small to demonstrate correlation, k_s seems to be the main parameter that affects the static positioning accuracy.

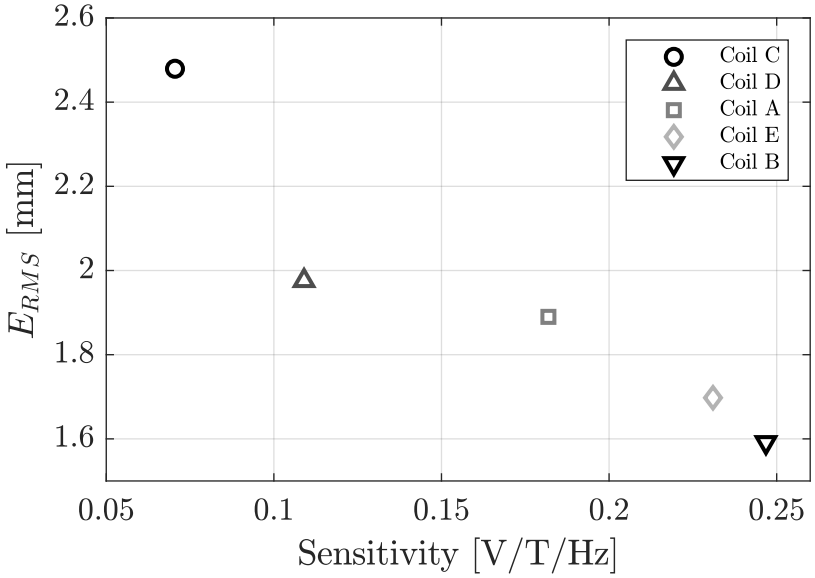

Figure 3.21: Relation between static accuracy (total error E_{RMS}) and sensitivity k_s.

3.4 Summary

This chapter represents the first investigation of bespoke sensor design for medical applications of electromagnetic tracking with reported RMS errors of 1.58 to 2.48 mm.

In the first part, hand-wound inductive coils were presented and were characterised over frequency. The results confirmed the excellent prediction of sensor sensitivity based on simple theoretical calculations (Figure 3.6).

In the second part, the coils were integrated in the Anser EMT system and tracking accuracy was investigated. As expected, tracking errors are decreased by the use of sensors with increased sensitivities: larger diameter coils, additional winding turns and the presence of a ferrite core (Figure 3.21).

The principles and experimental results indicate that the approach presented in this work can be easily used to produce highly-integrated sensors for instrument tracking. Future work might look to integrate such a sensor design within the instrument shaft, maintaining the instrument channel of the scope free for clinical investigations.

Bibliography

[1] Northern Digital Inc., *Aurora 5DOF Sensor 0.5 mm x 8 mm, Part Number: 610099*. [Online]. Available: https://www.ndigital.com/medical/products/tools-and-sensors/.

[2] FERROXCUBE, *ROD6/20-3C90*. [Online]. Available: https://www.ferroxcube.com/upload/media/product/file/MDS/3c90.pdf.

[3] Waveform, *Keysight Technologies 33500B Series Waveform Generators*. [Online]. Available: https://literature.cdn.keysight.com/litweb/pdf/5991-0692EN.pdf.

[4] Siglent, *Power Amplifier SPA1010*. [Online]. Available: https://www.siglent.eu/spa1010-10watt-power-amplifier.html.

[5] Aim, *I-prober 520*. [Online]. Available: http://resources.aimtti.com/datasheets/AIM-I-Prober_520_meter_data_sheet-Iss1A.pdf.

[6] Fluke-45, 'Users manual: Fluke 45 Multimeter', *Users manual: Fluke 45 Multimeter*, vol. 35, no. January 1989, pp. C–173–C–174, 1984. DOI: 10.1016/S0010-4655(84)82422-4. [Online]. Available: https://dam-assets.fluke.com/s3fs-public/45_____umeng0400.pdf.

[7] Agilent, *DSOX3024A Oscilloscope*. [Online]. Available: https://literature.cdn.keysight.com/litweb/pdf/5990-6619EN.pdf (visited on 10/06/2019).

[8] Neutrik, *RT5FC-B*. [Online]. Available: https://www.neutrik.com/media/10098/download/product-guide---section-xlr.pdf.

[9] S. Tumanski, 'Induction coil sensors - A review', *Measurement Science and Technology*, 2007, ISSN: 13616501. DOI: 10.1088/0957-0233/18/3/R01.

[10] R. J. Parker, *Advances in permanent magnetism*. Wiley, 1990, ISBN: 0471822930.

[11] B. K. Pugh, D. P. Kramer and C. H. Chen, 'Demagnetizing factors for various geometries precisely determined using 3-D electromagnetic field simulation', *IEEE Transactions on Magnetics*, vol. 47, no. 10, pp. 4100–4103, Oct. 2011, ISSN: 00189464. DOI: 10.1109/TMAG.2011.2157994. [Online]. Available: http://ieeexplore.ieee.org/document/6027575/.

[12] Hirst, *Gaussmeter GM08*. [Online]. Available: http://www.hirst-magnetics.com/downloads/gm07&gm08.pdf.

[13] H. A. Wheeler, *Inductor Sizing Equation*. [Online]. Available: https://www.allaboutcircuits.com/textbook/reference/chpt-1/inductor-sizing-equation/.

[14] D. Meeker, *Finite Element Method Magnetics (FEMM)*. [Online]. Available: http://www.femm.info/wiki/HomePage.

Chapter 4

AMR Sensor

This Chapter investigates the use of magnetoresistive sensors for electromagnetic tracking. This kind of sensors relies on a resistance that changes value depending on the magnetic field in which it is placed. They are active sensors that need an external supply to drive a current into the magnetoresistance. Their sensitivity is generally non-linear with frequency, unlike inductive sensors. On the other hand, they are well suited to be packaged in integrated circuits and they can operate also at DC.

First, a review of the magnetoresistive phenomenon and the main technologies based on it is given. Then, the anisotropic magnetoresistive (AMR) effect is explained in more detail. Finally, the measurements on the Sensitec AFF755B AMR sensor are presented.

4.1 Magnetoresistance sensors

The anisotropic magnetoresistive (AMR) effect was first observed by William Thomson in 1857, working on pieces of iron and nickel [1]. Magnetoresistance is the tendency of a material to change its resistance depending on its state of magnetisation. Since the magnetisation of the material can be changed by an externally applied magnetic field, it is possible to build magnetic field sensors that rely on this effect.

Magnetoresistive sensors are well suited for low and medium field strengths, as will be explained in section 4.2. They are usually manufactured in integrated circuits at small sizes and low costs.

A basic magnetoresistive effect has a geometrical origin and is due to Lorentz force acting on the charged particles q moving at velocity v that constitute the current:

$$\mathbf{F} = q(v \times \mathbf{B}) \tag{4.1}$$

The force deflects the path of the free charge carrier, resulting in an increase of the resistance, as shown in Figure 4.1a. It can be demonstrated that the change of the resistance depends on the square of the perpendicular magnetic field $\mathbf{B}_\perp$ and is bigger if the ratio l/w is small, where l is the length and w is the width of the plate in which the current flows [2]. A special geometry in which the effect is maximised, equivalent to a plate with $l/w \approx 0$, is the Corbino disc of Figure 4.1b.

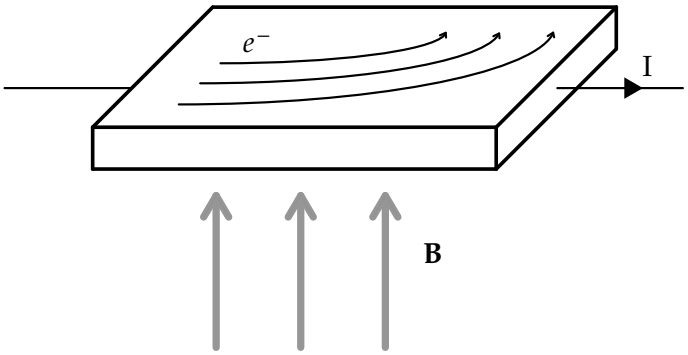

(a) The free charge carrier moves at a velocity v and, in the presence of an external magnetic field **B**, is subjected by the Lorentz force.

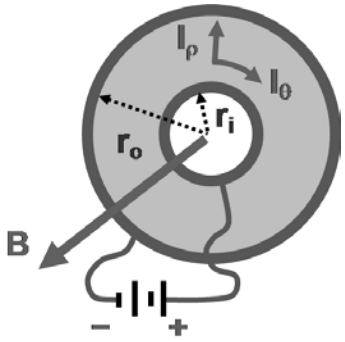

(b) The Corbino disc is the geometry that maximises the magnetoresistive effect due to Lorentz force. A magnetic field **B** along the axis of the disc (out of the page) curves the current lines along logarithmic spirals. *Image source: [3].*

Figure 4.1: Basic magnetoresistance effect due to Lorentz law: a longer path increases the resistance.

The phenomenon observed by Thomson was an example of AMR. In this case, the resistivity depends on the angle between the magnetisation and the direction of the current, hence the name *anisotropic* (Figure 4.2). The effect is explained by the simultaneous action of magnetisation and spin-orbit interaction and it occurs for small magnetic fields [4]. The relative change of the resistance is typically in the range of few percentages [5]:

$$\frac{\Delta R}{R} = f(B) \approx 3\%$$

There are many other magnetoresistive techniques used in sensors or other applications. Tunnel magnetoresistance (TMR) relies on the magnetic tunnel junction (MTJ) technology. Giant magnetoresistance (GMR) is a quantum mechanical effect. Colossal magnetoresistance (CMR) is a property of some materials. Extraordinary magnetoresistance (EMR) is a geometrical effect. In general, it is common to refer to a magnetoresistive effect as *xMR*, without specifying the actual technology.

Four xMR sensors were investigated for possible integration in the Anser EMT system. They are:

- Sensitec AFF755B [6]: based on AMR effect, integrates a Wheatstone bridge and a flip coil (see section 4.2 for more details), suited for the detection of weak magnetic fields (< 2 nT) including the Earth magnetic field, available in a SO8 package;
- Sensitec AFF756 [7]: almost the same as AFF755B with some small differences, such as a smaller bridge resistance, a smaller sensitivity, a bigger required flip current and availability in a LGA package;
- RedRock RR111 [8]: based on TMR technology, has an analog output linearly

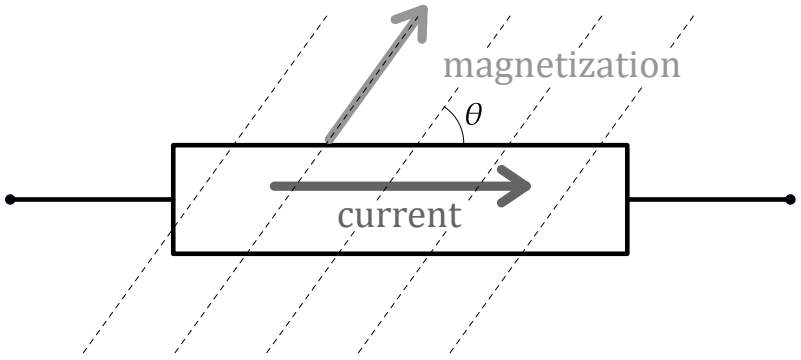

Figure 4.2: In an anisotropic magnetoresistive material the current is affected by the direction of the magnetisation, which can be caused by the orientation of the internal magnetic domains or by an external field.

Sensor	AFF755B	AFF756	RR111
Sensitivity	$13 \div 17\ \frac{\mathrm{mV/V}}{\mathrm{kA/m}}$ *(in range* $\pm 160\ \mathrm{A/m}$*)*	$8 \div 12\ \frac{\mathrm{mV/V}}{\mathrm{kA/m}}$ *(in range* $\pm 160\ \mathrm{A/m}$*)*	$-20\ \frac{\mathrm{mV/V}}{\mathrm{G}} = -251\ \frac{\mathrm{mV/V}}{\mathrm{kA/m}}$ *(in air)*
Sensing capability	$\pm 400\ \frac{\mathrm{A}}{\mathrm{m}}$	$\pm 800\ \frac{\mathrm{A}}{\mathrm{m}}$	$\pm 10\,\mathrm{G} = \pm 796\ \frac{\mathrm{A}}{\mathrm{m}}$ *(in air)*
Bandwidth	1 MHz	1 MHz	DC
Temperature range	$-40°\mathrm{C} \div +125°\mathrm{C}$	$-40°\mathrm{C} \div +125°\mathrm{C}$	$-40°\mathrm{C} \div +85°\mathrm{C}$
Electrical supply	5.0 V	5.0 V	3.0 V

Table 4.1: Specifications of the xMR sensors investigated.

proportional to the applied magnetic field, suited for DC fields, comes both in an SOT or in a LGA package;

- RedRock RR121 [9]: based on TMR technology, has a digital push-pull output, with operation point at 9 G (and −9 G) and release point at 5 G (and −5 G), with consequent hysteresis of 4 G. This kind of operation doesn't seem to be useful to EMT applications, so this sensor was not considered in the subsequent analysis.

The main specifications of the three xMR sensors are summarised in Table 4.1. The sensitivity is the ratio between the output voltage signal and the magnitude of the measured magnetic field. The sensing capability and the bandwidth are, respectively, the amplitude and the frequency ranges that can be measured. The temperature range defines the environment in which the sensor can operate. The electrical supply is the typical supply voltage, since all these devices are active sensors.

The RedRock RR111 operates with DC fields, but measurements demonstrated that it can give a good signal even up to 100 Hz, making it a possible candidate for a low frequency EMT application. One advantage to integrate xMR sensors in Anser EMT is their ability to measure low frequency fields, since inductive sensors are better suited

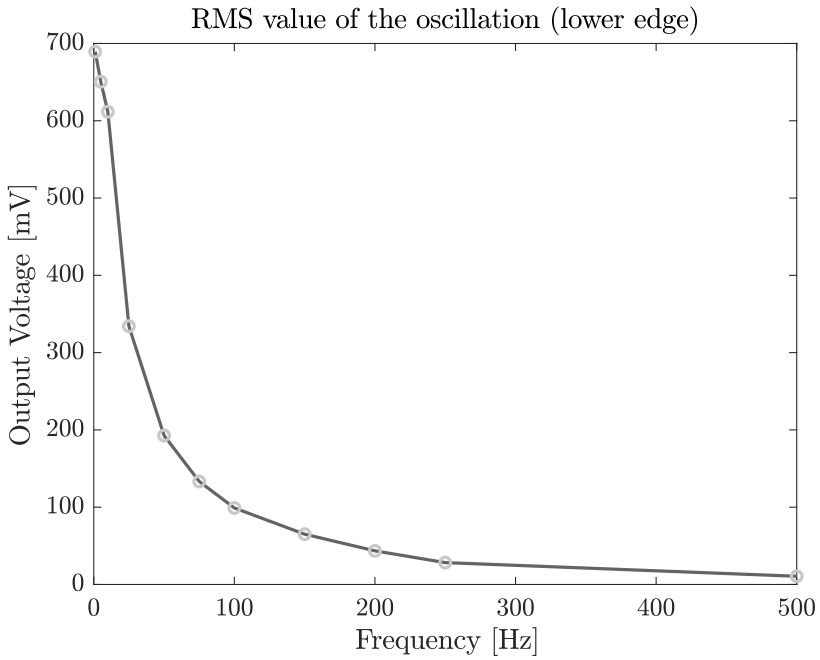

Figure 4.3: Amplitude of the oscillation of the lower edge of the RR111 quasi-square output signal.

(having enhanced sensitivity) for high frequency fields.

The output voltage of the RR111 is a quasi-square wave with a frequency of about 3.3 kHz, a peak value equal to the supply voltage (typically 3 V) and a minimum value varying with the magnetic field (Amplitude Width Modulation). The mean value of the quasi-square wave is proportional to the incident magnetic field. If the magnetic field is sinusoidal, the lower edge oscillates at the frequency of the field and the amplitude of the oscillation is more attenuated when the frequency increases. Figure 4.3 shows the RMS value of the oscillation over frequency.

The two Sensitec AMR sensors investigated have all the characteristics for possible integration in Anser EMT system, so it was chosen to further investigate their operation. Firstly, the AMR effect was deeper understood. Then, experimental work was performed on the AFF755B sensor.

4.2 AMR effect

For a thin ferromagnetic film, the current is affected only by the angle of the magnetisation and not by its direction: $R = R(\theta) = R(|\theta|)$, where θ is the angle between the current and the magnetisation, as shown in Figure 4.2. Therefore, the variation of the resistance due to AMR effect can be described by a sinusoidal law with period π (Equation 4.2) [10].

Equations 4.2-4.5 are equivalent:

$$\begin{aligned} R(\theta) &= R_t \sin^2(\theta) + R_l \cos^2(\theta) && (4.2)\\ &= R_t + (R_l - R_t)\cos^2(\theta) && (4.3)\\ &= R_l - (R_l - R_t)\sin^2(\theta) && (4.4)\\ &= \frac{R_l + R_t}{2} + \frac{R_l - R_t}{2}\cos(2\theta) && (4.5) \end{aligned}$$

Equation 4.3 is called Voigt–Thomson formula. In the following analysis, these equations are used as convenient and $\Delta R = R_l - R_t$ indicates the total range of variation of the resistance, while $R_{av} = \frac{1}{2}(R_l + R_t)$ is the average resistance.

4.2.1 Direction of external magnetic field

The AMR effect can be used in sensors to detect the direction of an external magnetic field. For this purpose, the resistance is a thin layer placed in an environment with no pre-magnetisation. In thin layers the magnetisation follows the direction of the external applied magnetic field, so the angle θ of Equation 4.5 is actually the angle between the current in Figure 4.2 and the external field. From the measurement of $R(\theta)$, knowing the values R_l and R_t, the angle of the field can be explicitly determined up to 180°:

$$\theta = \frac{1}{2}\text{acos}\left(\frac{2}{\Delta R}\left[R(\theta) - R_{av}\right]\right) + k\,\pi \tag{4.6}$$

In practice, AMR sensors are always built with four resistances arranged in a Wheatstone bridge (see for example the Application Note of Sensitec AA700 Family [11].) This configuration ensures an improved accuracy, because the measured signal is no longer proportional to the absolute change of the resistance $R + \Delta R$ but to the relative change $\Delta R/R$, which is normally around 3%, as indicated in section 4.1. Moreover, the offset of the resistance due to temperature is inherently eliminated.

Figure 4.4 shows the schematic configuration of the Wheatstone bridge. The four resistances can be assumed to be equal and covered by the same magnetic field since they are built in very small and highly reproducible integrated circuits. With reference to the angle θ defined in Figure 4.4 and following Equation 4.5, when the magnetic field is applied at an angle $\theta = 0°$, R1 and R2 are magnetised in the longitudinal direction and have so a higher resistance ($R_{0°}(0°) = R_l$) than R3 and R4, which are magnetised perpendicularly ($R_{90°}(0°) = R_t$). In general, for any angle θ, the resistances follow from Equation 4.7:

$$\begin{aligned} R_1 = R_2 = R_{0°}(\theta) &= R_{av} + \frac{1}{2}\Delta R\cos(2\theta)\\ R_3 = R_4 = R_{90°}(\theta) &= R_{av} - \frac{1}{2}\Delta R\cos(2\theta) \end{aligned} \tag{4.7}$$

$R_{0°}$ assumes its maximum value when $\theta = k\,\pi$, while in this condition $R_{90°}$ has its minimum value. The opposite happens when $\theta = \pi/2 + k\,\pi$.

Applying the voltage divider between the supply voltage V_{CC} and ground GND for

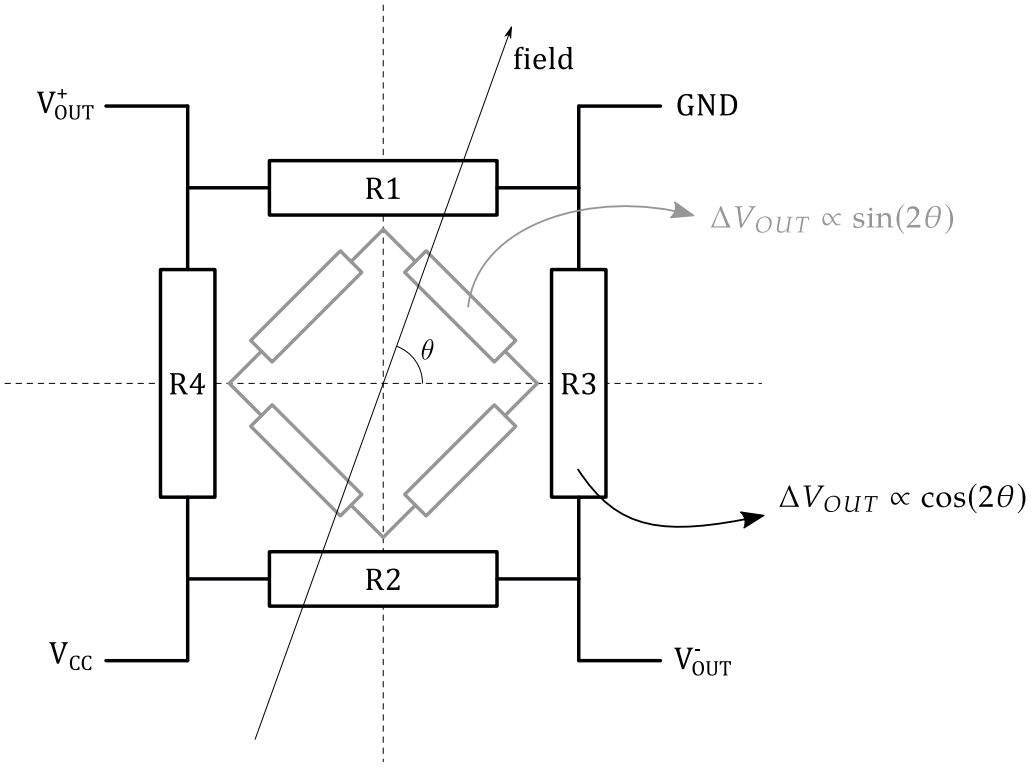

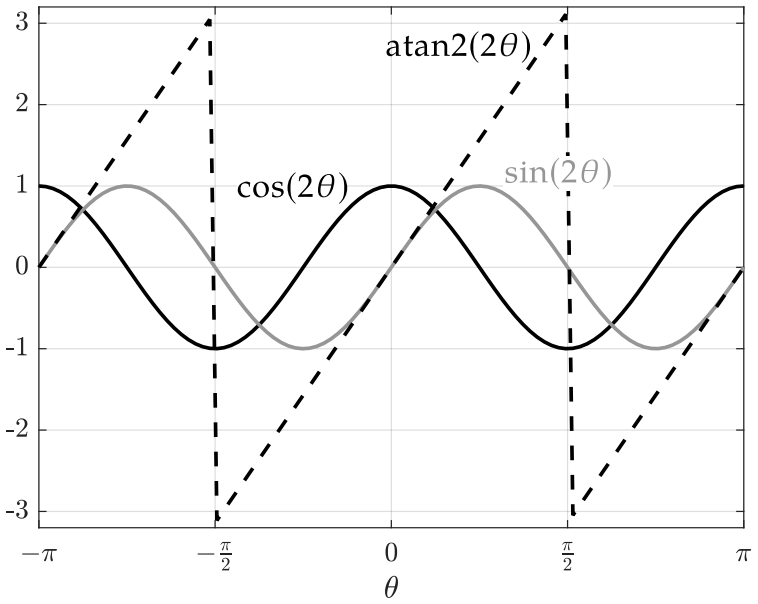

Figure 4.4: Wheatstone bridge configuration for xMR sensing. A second bridge (in gray) shifted of 45° can be added to accurately measure the angle of the external field.

the output voltages, Equation 4.8 is obtained:

$$V^{+}_{OUT} = \frac{R_{0^\circ}}{R_{90^\circ} + R_{0^\circ}} V_{CC}; \qquad V^{-}_{OUT} = \frac{R_{90^\circ}}{R_{90^\circ} + R_{0^\circ}} V_{CC} \tag{4.8}$$

Overall, the differential output voltage is given by:

$$V^{+}_{OUT} - V^{-}_{OUT} = \frac{R_{90^\circ} - R_{0^\circ}}{R_{90^\circ} + R_{0^\circ}} V_{CC} = \frac{\Delta R \cos(2\theta)}{2R_{av}} V_{CC} = \frac{R_l - R_t}{R_l + R_t} \cos(2\theta) V_{CC} \tag{4.9}$$

This method is not well conditioned when the field is aligned to the longitudinal axis, because in this case the cosine is very flat and small changes in the angle does not result in significant changes in resistance. Then, a second bridge is usually placed, as illustrated in Figure 4.4. The output voltage of the first bridge is proportional to the cosine of 2θ (Equation 4.9), while the second bridge is spatially delayed by $\pi/4$, so its output voltage is proportional to the sine of 2θ. Therefore the direction of the magnetic field is given by:

$$\theta = \frac{1}{2} \text{atan2} \left(\frac{\Delta V^{90^\circ}_{OUT}}{\Delta V^{0^\circ}_{OUT}} \right) + k\,\pi \tag{4.10}$$

4.2.2 Magnitude of external magnetic field

As seen, the AMR effect is directly used to measure the direction of a magnetic field. However, with a proper configuration it is possible to calculate the magnitude of the external applied magnetic field. This is obtained by pre-magnetising the resistance and by measuring the deflection of the magnetisation angle due to the external magnetic field. In the absence of external fields, the vector of magnetisation **M** is directed along the anisotropy axis (or *easy axis*). Following the notation of literature, this axis is denoted as y and the external field **H** is measured along direction x [10]. Refer to Figure 4.5 for the definitions of the angles and the axes.

The best approach to calculate the direction of the magnetisation vector **M** when a field is applied is to minimize the total free energy of the material. This is given by the equation proposed by Lev Landau and Evgeny Lifshitz in 1935 [12]:

$$E = E_{ext} + E_a + E_{ex} + E_m + E_\sigma \tag{4.11}$$

Refer to [13] for more details.

In the case of a thin ferromagnetic film, the magnetisation can be assumed to be uniform and rotating in unison. Therefore, it can be described by one single magnetisation vector **M** and the ferromagnet is essentially a single-domain. In this condition, the terms E_{ex}, E_m and E_σ of Equation 4.11 are null and the contributions to the free energy come only from the Zeeman energy E_{ext}, due to the external magnetic field, and the anisotropy energy E_a, which is lower if the magnetisation is along the easy axis. If the anisotropy is uniaxial, the system can be described by the Stoner-Wohlfarth model [14] and the energy is:

$$E = E_{ext} + E_a = -\mu_0 \mathbf{H_{ext}} \cdot \mathbf{M} + K_u \sin^2 \varphi \tag{4.12}$$

with $\mathbf{H} = (H_x, H_y)$, $\mathbf{M} = M_s \angle\varphi$ and K_u being the first anisotropic constant [5]. It is usual to define a theoretical anisotropy field H_k, related to K_u by:

$$H_k = \frac{2K_u}{\mu_0 M_s} \tag{4.13}$$

Then Equation 4.11 becomes:

$$E = -\mu_0 M_s \cos(\varphi) H_y - \mu_0 M_s \sin(\varphi) H_x + \frac{1}{2}\mu_0 H_k M_s \sin^2\varphi \tag{4.14}$$

and to get the angle φ that minimizes the free energy, the partial derivative with respect to φ is made equal to 0:

$$\frac{\partial E}{\partial \varphi} = \mu_0 M_s \sin(\varphi) H_y - \mu_0 M_s \cos(\varphi) H_x + \mu_0 M_s H_k \sin(\varphi)\cos(\varphi) = 0 \tag{4.15}$$

The correct operation of AMR sensors is assured when the external field is much smaller compared to the inner pre-magnetisation. Then the angle φ by which $\mathbf{M}$ is shifted from the easy axis is small:

$$\varphi \approx 0 \tag{4.16}$$

$$\cos\varphi \neq 0 \tag{4.17}$$

$$\sin\varphi \simeq \tan\varphi \tag{4.18}$$

Simplifying Equation 4.15 by the term $\mu_0 M_s \cos\varphi$, Equation 4.19 is obtained:

$$\tan(\varphi) = \frac{H_x}{H_k + H_y} \rightarrow \varphi = \operatorname{atan}\left(\frac{H_x}{H_k + H_y}\right) \tag{4.19}$$

In the following discussion, the normalised quantity $\frac{H_x}{H_k+H_y}$ will be denoted by h, for convenience.

It is possible to think at H_k as a pre-existent external field, generated by the magnetic domains, as shown in Figure 4.5. It has to be remembered that the phenomena at stake inside the material are far more complicated and this assumption is true only for small variations from the idle state.

As seen in paragraph 4.2.1, AMR effect can be used to calculate the angle θ between the current $\mathbf{I}$ and the total magnetisation $\mathbf{M}$. If α is the angle between $\mathbf{I}$ and the easy axis y, it is true that $\alpha = \varphi + \theta$.

Figure 4.6 shows how much the resistance changes with respect to its minimum value R_t, normalized by the maximum gap $\Delta R = R_l - R_t$, for different values of angle α, as a function of h. Around $h = 0$, that is when a small external field is applied, the behaviour for $\alpha = 0°, 90°$ shows a quadratic dependence and the behaviour for $\alpha = \pm 45°$ has a linear dependence. The curves are obtained from Equation 4.3, with $\theta = \alpha - \varphi$ and φ given by Equation 4.19:

$$\frac{R(\theta) - R_t}{\Delta R} = \cos^2\left(\alpha - \operatorname{atan}\frac{H_x}{H_k + H_y}\right) \tag{4.20}$$

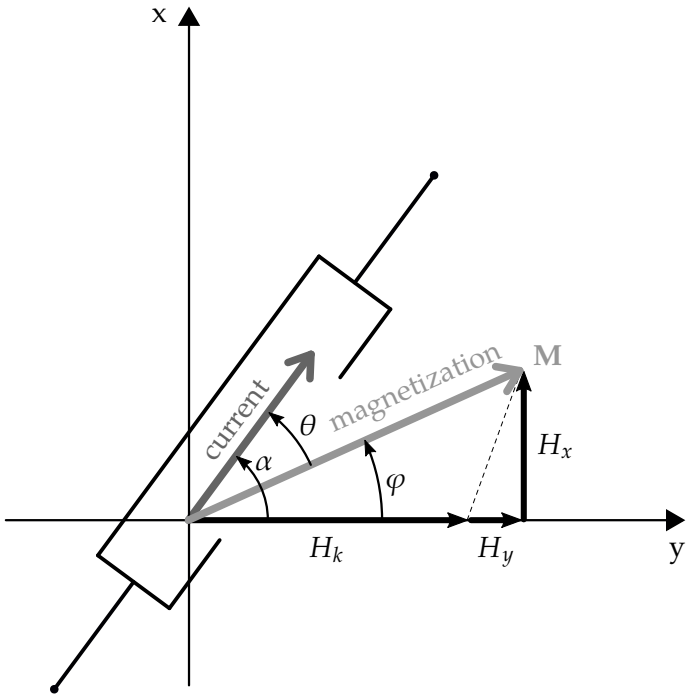

Figure 4.5: Direction of the current and of the magnetisation **M** when an external field **H** is applied. y is the *easy axis* and indicates the direction of **M** when **H** = 0. The representation of the pre-magnetisation as an external field H_z is true only for $H_x \ll H_k + H_y$.

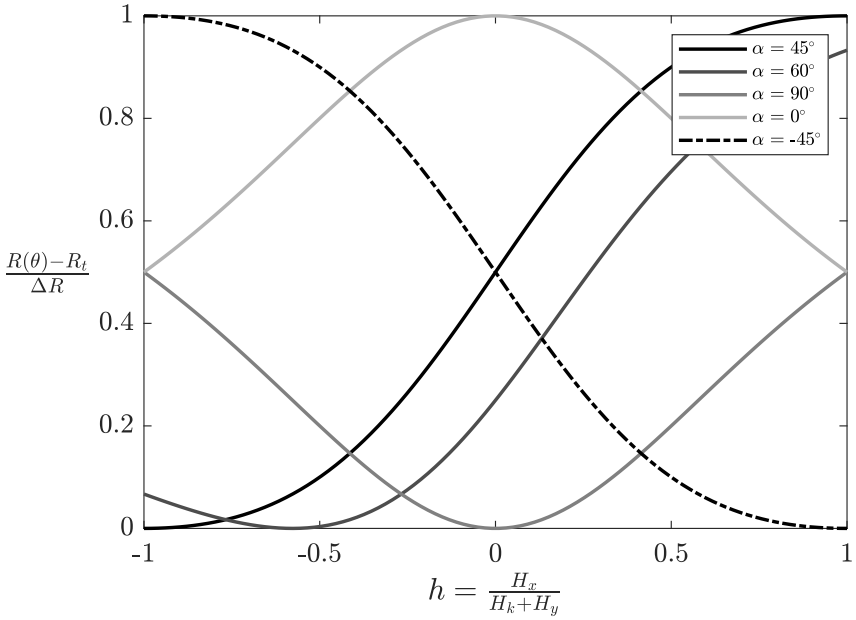

Figure 4.6: Relative change of the resistance in function of the quantity $h = {}^{H_x}/_{H_k+H_y}$, for different values of α. The curves are described by Equation 4.20, which is true only for $h \approx 0$. Otherwise there is not an explicit formulation. In particular, for $\alpha = \pm 45°$, the relationship is linear.

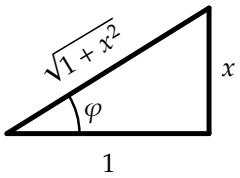

$$\varphi = \operatorname{atan}(x)$$

$$\cos(\varphi) = \frac{1}{\sqrt{1+x^2}} \qquad \sin(\varphi) = \frac{x}{\sqrt{1+x^2}}$$

Figure 4.7: Useful trigonometric formulas.

Equation 4.20 and Figure 4.6 are valid only for small values of φ, when the assumption of Equation 4.18 is true. This happens only for small h, when the external field is small compared to H_k, otherwise there is no dependence of $R(\theta)$ on h (see Equation 4.15). The cases $\alpha = 0°$ and $\alpha = 90°$ are analysed.

If $\alpha = 0°$, then $\theta = -\varphi$ and the variation of the resistance, given by Equation 4.3, is:

$$\begin{aligned} R_{0°}(\theta) &= R_t + \Delta R \cos^2(\theta) = R_t + \Delta R \cos^2(\varphi) \\ &= R_t + \Delta R \cos^2(\theta) \\ &= R_t + \Delta R \frac{h^2}{1+h^2} \end{aligned} \tag{4.21}$$

where the identity $\cos(\operatorname{atan} x) = x/\sqrt{1+x^2}$ was used (Figure 4.7).

As said, the pre-magnetisation is much larger than the field that is measured:

$$H_k \gg H_x \tag{4.22}$$

$$h^2 \ll 1 \tag{4.23}$$

$$\frac{h^2}{1+h^2} \simeq h^2 \tag{4.24}$$

and the field has to be measured along the x direction:

$$H_y \approx 0 \tag{4.25}$$

$$h \simeq \frac{H_x}{H_k} \tag{4.26}$$

then, from Equation 4.21, the variation of the resistance is almost proportional to the square of the external field H_x:

$$R_{0°}(\theta) - R_t \simeq \frac{\Delta R}{H_k^2} H_x^2 \tag{4.27}$$

If $\alpha = +45°$, then $2\theta = \frac{\pi}{2} - 2\varphi$. From Equation 4.5 the variation of the resistance is of:

$$R_{+45°}(\theta) = R_{av} + \frac{\Delta R}{2}\cos(2\theta) = R_{av} + \frac{\Delta R}{2}\sin(2\varphi) \tag{4.28}$$

Using the double-angle formula for the sine function and the second identity of Figure 4.7:

$$\sin(2\varphi) = 2\sin(\operatorname{atan} h)\cos(\operatorname{atan} h) = 2\frac{h}{1+h^2}$$

Since, as said, $h^2 \ll 1$ and $H_y \approx 0$, the resistance variation depends approximately linearly on the external field:

$$R_{+45^\circ}(\theta) - R_{av} \simeq \frac{\Delta R}{H_k} H_x \tag{4.29}$$

It is important to note that the case $\alpha = -45^\circ$ implies $\cos(2\theta) = -\sin(2\varphi)$. Then, following the same steps, Equation 4.30 is obtained:

$$R_{-45^\circ}(\theta) - R_{av} \simeq -\frac{\Delta R}{H_k} H_x \tag{4.30}$$

This property is clear also from Figure 4.6 and it states that opposite angles between the vectors of the current and of the total magnetisation cause the same change of the resistance but in opposite directions, if affected by the same field H_x. All commercial sensors take advantage of this phenomenon, connecting resistances oriented at +45° and −45° in a configuration similar to the one of Figure 4.4. In this way the output signal becomes differential, increasing the sensitivity and compensating the temperature errors. The output voltage is given by Equation 4.31 and obtained in the same way as for Equation 4.9:

$$V_{OUT}^{+} - V_{OUT}^{-} = \frac{R_{45^\circ} - R_{-45^\circ}}{R_{45^\circ} + R_{-45^\circ}} V_{CC} \simeq \frac{2\Delta R}{2R_{av}} \frac{H_x}{H_k} V_{CC} = 2\frac{R_l - R_t}{R_l + R_t} \frac{V_{CC}}{H_k} H_x \tag{4.31}$$

Several techniques can be used to achieve an angle $\alpha = \pm 45^\circ$ and obtain the linearisation and stabilisation of thin film magnetic field sensors. The most used is the *barber pole* structure [15]: Aluminium stripes are sputtered on the ferromagnetic film, slanted by an angle of 45° with respect to the easy axis. If the stripes are highly conductive, the direction of the current is deflected by 45°. Four of such elements are connected into a Wheatstone bridge.

4.2.3 Flip coil

The function of AMR sensors is based on the single-domain magnetisation of the ferrite film. However, at room temperature partial demagnetisation may occur and the magnetic domains no longer remain aligned. This is reflected in a loss of sensitivity.

Usually, integrated sensors include a flip coil on the chip which gives the possibility to re-magnetise the material through short current pulses. For example, for the AFF755B sensor under investigation, the manufacturer suggests a flip coil current of ±150 mA, with pulses of 1 µs on and 1 ms off. The voltage necessary for driving the required current is less than 0.5 V.

In general, a good technique is to flip the magnetisation in both the directions. In this way it is possible to correct sensor offsets, caused by small variations of the resistance of the ferrite film.

4.2.4 Cross-field error

From Equation 4.31, if the assumption of $H_y \approx 0$ is not true, or not known a priori, the more general Equation 4.32 is obtained:

$$\Delta V_{OUT} \simeq \frac{\Delta R}{R_{av}} \frac{H_x}{H_k + H_y} V_{CC} \tag{4.32}$$

It is clear that a component H_y of the field perpendicular to the sensing direction not only decreases the sensitivity of the sensor but also affects the output voltage in an unpredictable way, making the measurement unreliable. There are different possible techniques that can be used to overcome the cross-field error:

- Increase the magnitude of the pre-magnetisation H_k, so that the output signal is less sensitive to a small value of H_y. However, this also results in the sensor sensitivity decreasing and the signal-to-noise ratio increases.

- Some sensors implement a coil that can be used for feedback compensation of the measured field. In this kind of sensors, the output signal of Equation 4.32 is the input of a feedback PI controller that drives the current of the compensation coil, proportional to the measured component of the field H_x. A change in the constant of proportionality between ΔV_{OUT} and H_x does not affect the steady state value of the feedback current, but only the time constant of the control system. Forcing the component H_x to be null, larger fields can be measured still assuring $h \approx 0$, with the possibility to use the simplification of Equation 4.18, which is the condition for the linear dependence of Equation 4.31. Another advantage of this method is that it automatically corrects for possible offsets, the decreased sensitivity due to non ideal magnetisation of the ferrite domains and the influence of temperature. The main drawbacks are: increased complexity, possible non-linearity caused by the non homogeneous feedback field due to the small dimension of the compensation coil, increased power consumption and delay in the measurement.

- Use a flipping of the pre-magnetisation. If the external field H_y is much smaller than the ferrite magnetisation H_k, Equation 4.32 can be rewritten as:

$$\Delta V_{OUT} \simeq \frac{\Delta R}{R_{av}} \frac{H_x}{H_k \left(1 + \frac{H_y}{H_k}\right)} V_{CC} \overset{H_y \ll H_k}{\simeq} \frac{\Delta R}{R_{av}} \frac{H_x}{H_k} \left(1 - \frac{H_y}{H_k}\right) V_{CC} \tag{4.33}$$

  If the direction of H_k is flipped and a second measurement is taken, it is possible to suppress the dependence on H_y, as shown in Equation 4.34:

$$\Delta V_{OUT}^{+H_k} - \Delta V_{OUT}^{-H_k} = 2 \frac{\Delta R}{R_{av}} \frac{H_x}{H_k} V_{CC} \tag{4.34}$$

- Use a directional AMR sensor to measure the direction of the field to find the best fit for H_x and H_y of Equation 4.32, applied to a second AMR sensor measuring the magnitude. It is also possible to couple two (or more) AMR magnitude sensors

oriented in different directions and mathematically reconstruct the three components of the external magnetic field.

4.3 Characterisation over frequency

The behaviour of the AFF755B sensor over frequency was investigated. The measurement setup was the same described in paragraph 3.2.1, with the addition of a signal amplifier for the output of the sensor. The typical sensitivity declared by the manufacturer is of 15 $\frac{\mathrm{mV/V}}{\mathrm{kA/m}}$, as reported in Table 4.1. The sensor was supplied with $V_{CC} = 5\,\mathrm{V}$ and was surrounded by air, so that the sensitivity in $\mathrm{V\,T^{-1}}$ was:

$$\frac{15{\times}10^{-3} \cdot 5}{1{\times}10^{3} \cdot \mu_0} = 59.68\,\frac{\mathrm{V}}{\mathrm{T}} \tag{4.35}$$

Unlike inductive sensors, the output voltage of xMR sensors is not proportional to frequency. For example, considering the custom Helmholtz coil used to generate the field, the maximum field that it can produce is $B_z = 402\,\mu\mathrm{T}$ (see paragraph 2.4.1 for reference), resulting, from Equation 4.35, in a signal of 24 mV. With an increase in the frequency, the signal decreases further and it becomes difficult to measure it without noise.

4.3.1 Gain of the signal amplifier

The signal amplifier used (INA163, *Texas Instruments, Dallas, Texas* [16]) is the same device integrated in each input channel of the Anser EMT system (section 1.3). Before use, the amplifier was firstly characterized, to make sure it had a constant gain and sufficient bandwidth. The gain was set with a resistance of 2000 Ω to the value [16]:

$$\mathrm{G} = 1 + \frac{6000}{2000} = 4 \tag{4.36}$$

A sinusoidal wave with a constant amplitude of 200 mVpp (peak to peak) was applied to the input of the amplifier. The frequency was varied from 1 kHz to 1 MHz. The output was measured and the ratio between output and input voltages is plotted in Figure 4.8. The measured average gain is of 3.9147. With this gain and the above-mentioned input voltage, the bandwidth of the amplifier is over 1 MHz.

4.3.2 Characterisation of Sensitec AFF755B sensor

Power supply and signal amplification on a breadboard

A breadboard was used to host the circuits for the power supply of the sensor and for the signal amplification. The AMR sensor was supplied with 5 V and the INA amplifier with ±15 V, generated by an external voltage supply. Capacitors of 100 pF were placed between the supply voltages and ground, to stabilise the DC voltage. Two wires from the board to the sensor delivered 5 V and ground, while two wires carried the differential output signal to the input of the amplifier. A low-pass RC filter was placed on the output of the amplifier,

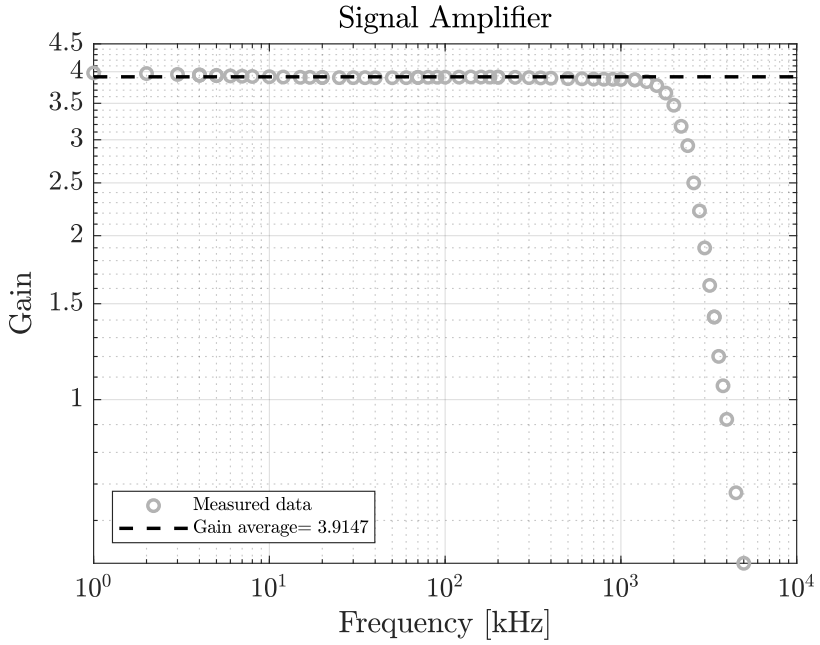

Figure 4.8: Bandwidth of the signal amplifier, for a gain of about 4 and an input sinusoidal signal of amplitude 200 mVpp.

with $R = 16\,\Omega$, $C = 100\,\text{pF}$ and a consequent cut-off frequency of $f_{RC} = 1/(2\pi RC) \approx 100\,\text{MHz}$. The amplified single-ended signal was displayed and measured by the oscilloscope. The sensor was placed at the geometric centre of the Helmholtz coil presented in chapter 2.

The inner ferrite film of the sensor was previously re-magnetised with a flip coil current driven by a pulsed voltage of 250 mV. Figure 4.9 shows the ratio between the output voltage [mV] and the incident magnetic field $\left[\frac{\text{kA}}{\text{m}}\right]$. The output voltage is normalized by the supply voltage of 5 V. At lower frequencies a sensitivity of 14.3081 $\frac{\text{mV/V}}{\text{kA/m}}$ can be seen, compared to the declared sensitivity of 13 to 17, with a typical value of 15 $\frac{\text{mV/V}}{\text{kA/m}}$ (Table 4.1). The bandwidth of the sensor is declared to be 1 MHz.

It can be seen that from about 100 kHz the sensitivity begins to increase linearly with the frequency. Also a phase shift between the measured signal and the input field was observed, starting from the same frequency. In general, the measurement of xMR sensors should be in phase with the magnetic field and not delayed of 90° as for inductive sensors. It was supposed that some unshielded loops of the power or signal wires were resulting in an inductive component, increasing and shifting the output signal of the sensor at higher frequencies.

Prototype board including the sensor and the amplifier

To investigate the possibility that unintended loops were affecting the measurement of the sensor, the same circuit described in the previous paragraph was miniaturised on a prototype board, which included the sensor and the amplifier, in order to minimise the length of the wires. The design of the circuit is displayed in Figure 4.10. The supply voltages (+5 V for the sensor and ±15 V for the amplifier) and the ground were all provided

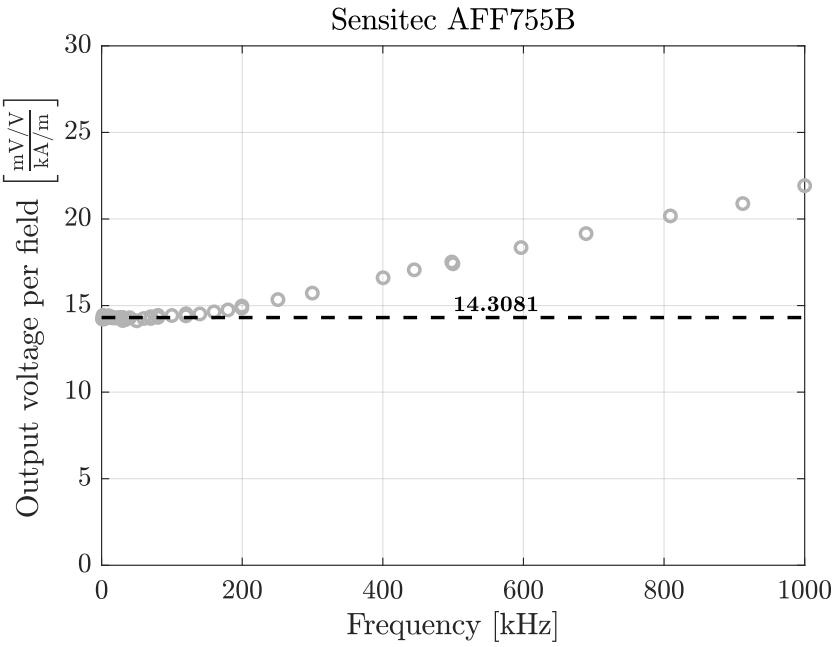

Figure 4.9: Sensitivity of AFF755B sensor, over the frequency.

by the Anser EMT board, through a shielded cable. From the sensor's specifications, the minimum flip current is 150 mA and the flip coil has a resistance of 1.5 Ω. An external resistance of 32 Ω was added in series to the flip coil pins, making it possible to drive the required flip current directly from the 5 V supply. The single-ended output voltage was also connected to a shielded cable and was terminated in a miniXLR connector, for possible use in the Anser EMT system. The final result is shown in Figure 4.11. In particular the photo of the back shows how all the wires were of minimum length. However, the new measurements gave almost the same result of Figure 4.9, indicating that the out-of-phase component was possibly not due to inductive phenomena.

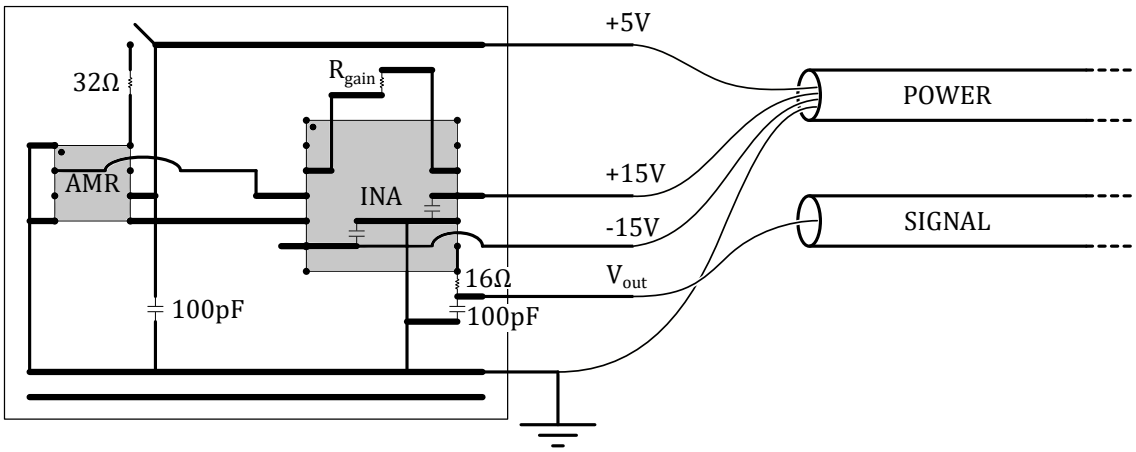

Figure 4.10: Sketch of the circuit soldered on the prototype board.

Figure 4.11: Prototype board used in the second set of measurements. Front: the sensor and the amplifier are integrated in the same circuit at small separation distance. Back: the length of the wires are minimised.

Analysis of the inphase component

Since the AMR sensor should always give a signal in phase with the field, the inphase component was extrapolated to inspect if the sensitivity due to that component was constant, of about 15 $\frac{\mathrm{mV/V}}{\mathrm{kA/m}}$. The function used to fit the sinusoids of the magnetic field and of the sensor output voltage, to get the amplitude and the phase and to separate the inphase and the quadrature components, makes use of the FFT. The main commands are reported in Listing 4.1. The typical result of the fitting is shown in Figure 4.12, for a specific frequency. The same procedure was applied for every frequency of the data points of Figure 4.9.

Figure 4.13 shows the sensitivity due to the inphase component only, for the measurements obtained with the breadboard setup and for the measurements obtained with the prototype board circuit. Both data show a net drop of sensitivity, starting from around 100 kHz in the first case and from around 200 kHz in the second case. The more likely hypothesis is that the quadrature component does not come from an external source of signal (*i.e.* inductive), but rather that there is a resonance in the circuit which shifts (and amplifies) the signal, originally in phase, coming from the AMR sensor.

Further investigation of these high frequency effects was not pursued since the Anser EMT system works at frequencies between 20 and 30 kHz, while the constant and predicted behaviour of the sensor under 100 kHz was adequately demonstrated.

Listing 4.1: MATLAB function to fit a sinusoidal wave.

```
data = readmatrix('directory\of\the\file.csv');
t = data(:,1);  % Time
s1 = data(:,2); % Current
s2 = data(:,3); % Vout
s1=s1-mean(s1); % removes a possible DC component
s2=s2-mean(s2);

L=length(t);
T=(t(end)-t(1))/L;          % Sampling period
Fs=1/T;                     % Sampling frequency
f = Fs*(0:(L/2))/L;         % Frequency range

%% Current
fft1=fft(s1)/L;  % 1/L in the sum is like dt in the integral
% Cosines have only positive frequencies and their Fourier coeff are
    the double
fft1 = fft1(1:L/2+1);
fft1(2:end-1) = 2*fft1(2:end-1);
P1 = abs(fft1);             % To get the amplitudes of cosines
% Max armonic, the one of the sinusoid that has to be fitted
k1=find(P1==max(P1));
a1=P1(k1);                  % Amplitude
f1=f(k1);                   % Frequncy
p1=angle( fft1(k1));        % Phase
% NOTE: the phase of the fft is referred to left corner, while
% the time has its 0 in the middle. If there is an odd number
% of periods (k-1, because the first term of the fft is the DC
% component) the 2 axis have a difference of half a period
if mod(k1-1,2) p1=p1+pi; end

%% Vout
fft2 = ...
...

%% Inphase and quadrature components of Vout
a2d = a2*cos(p1-p2);
a2q = a2*sin(p1-p2);
```

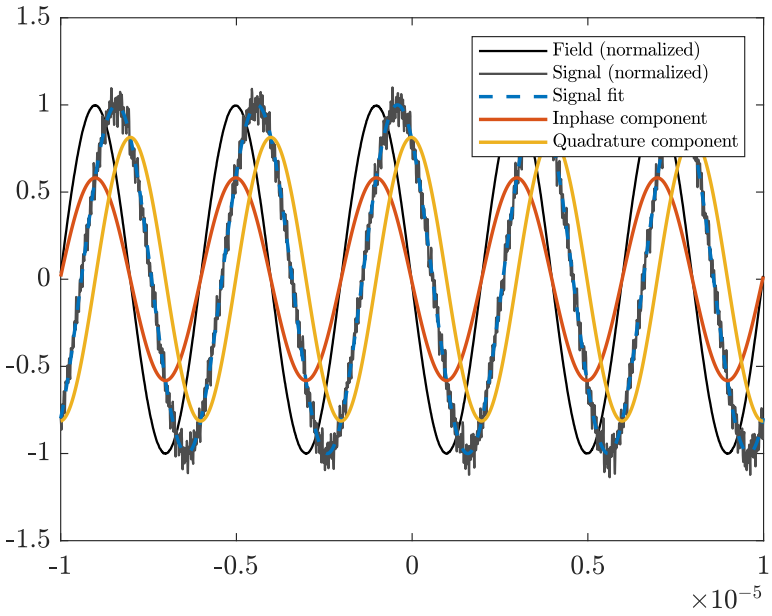

Figure 4.12: Fit of the sinusoids of the magnetic field and of the output signal, at 250 kHz. The incident field is normalized to 0.115 A m^{-1}, the voltage signal to 2.6 µV. The total sensitivity is 22.36 $\frac{\text{mV/V}}{\text{kA/m}}$, larger than the expected 15 $\frac{\text{mV/V}}{\text{kA/m}}$. The sensitivity due to the inphase component is 13.00 $\frac{\text{mV/V}}{\text{kA/m}}$.

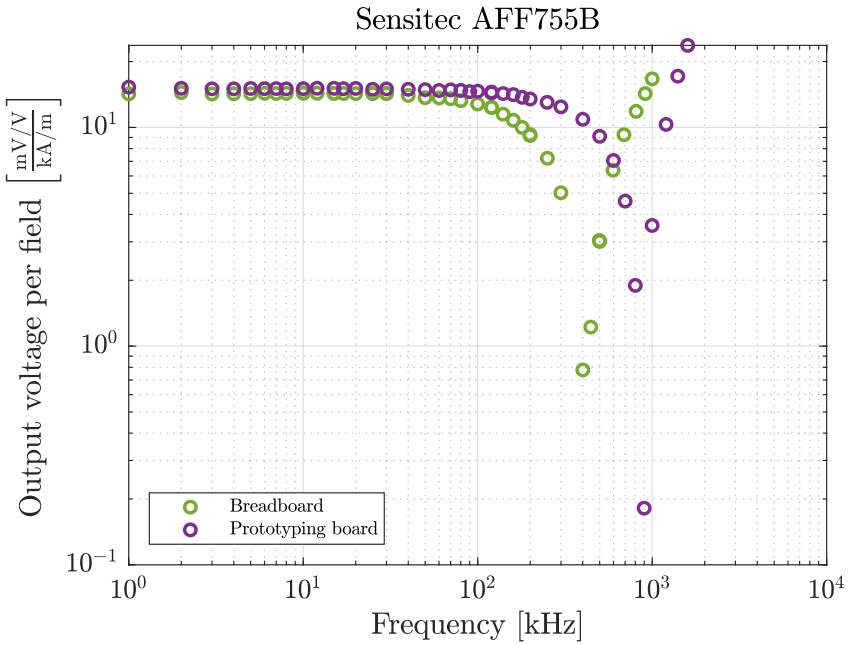

Figure 4.13: Output signal due to the inphase component of the two sets of measurements for the breadboard and the soldered prototype board.

4.4 Summary

This chapter presented the first investigation for integration of magnetoresistive sensors in Anser EMT. The study started with the comparison of the commercial xMR sensors listed in Table 4.1. This led to the selection of the Sensitec AFF755B, an anisotropic magnetoresistive (AMR) sensor.

The basic AMR effect was explained and the main configurations that allow stabilisation and linearisation of AMR sensors were described. The use of AMR sensors in magnetic tracking systems encounter certain difficulties, such as the need of active supplies for the magnetoresistance and for the flip coil current. Cross-field errors are another challenge to face when using AMR sensors within 3D magnetic fields, as explained in paragraph 4.2.4.

Experimental work provided expected results, confirming the constant manufacturer-declared sensitivity at the frequencies of interest for Anser EMT. Phase shift and signal amplification were observed at higher frequencies. Deeper circuit analysis may explain this behaviour.

Bibliography

[1] W. Thomson, 'XIX. On the electro-dynamic qualities of metals:—Effects of magnetization on the electric conductivity of nickel and of iron', *Proceedings of the Royal Society of London*, vol. 8, pp. 546–550, Jan. 1857, ISSN: 0370-1662. DOI: 10.1098/rspl.1856.0144. [Online]. Available: http://www.royalsocietypublishing.org/doi/10.1098/rspl.1856.0144.

[2] H.-J. Lippmann and F. Kuhrt, 'Der Geometrieeinfluß auf den Hall-Effekt bei rechteckigen Halbleiterplatten', *Zeitschrift für Naturforschung A*, vol. 13, no. 6, Jan. 1958, ISSN: 1865-7109. DOI: 10.1515/zna-1958-0608. [Online]. Available: https://www.degruyter.com/view/j/zna.1958.13.issue-6/zna-1958-0608/zna-1958-0608.xml.

[3] Wikimedia Commons, *Corbino disc*, 2008. [Online]. Available: https://commons.wikimedia.org/wiki/File:Corbino_disc.PNG (visited on 07/08/2019).

[4] T. McGuire and R. Potter, 'Anisotropic magnetoresistance in ferromagnetic 3d alloys', *IEEE Transactions on Magnetics*, vol. 11, no. 4, pp. 1018–1038, Jul. 1975, ISSN: 0018-9464. DOI: 10.1109/TMAG.1975.1058782. [Online]. Available: http://ieeexplore.ieee.org/document/1058782/.

[5] P. Ripka, 'Magnetic Sensors and Magnetometers', *Measurement Science and Technology*, vol. 13, no. 4, p. 645, 2002. DOI: 10.1088/0957-0233/13/4/707.

[6] Sensitec, *AFF755B*, 2015. [Online]. Available: https://www.sensitec.com/fileadmin/sensitec/Service_and_Support/Downloads/Data_Sheets/AFF700_800/SENSITEC_AFF755B_DSE_06.pdf.

[7] ——, *AFF756*, 2018. [Online]. Available: https://www.sensitec.com/fileadmin/sensitec/Service_and_Support/Downloads/Data_Sheets/AFF700_800/SENSITEC_AFF756_DSE_09.pdf.

[8] RedRock, *RR111*. [Online]. Available: https://cotorelay.com/wp-content/uploads/2018/02/RedRock-111TMR-Datasheet.pdf.

[9] ——, *RR121*. [Online]. Available: https://cotorelay.com/wp-content/uploads/2017/10/RedRock-121TMR-Datasheet.pdf.

[10] S. Tumanski, *Thin Film Magnetoresistive Sensors*. IOP Publishing Ltd, 2001, ISBN: 0750307021. DOI: 10.1887/0750307021. [Online]. Available: http://stacks.iop.org/0750307021.

[11] Sensitec, *AA700 Family. Application Note*, 2016. [Online]. Available: https://www.sensitec.com/service-support/download/file-category/product-information.

[12] L. Landau and E. Lifshitz, 'On the theory of the dispersion of magnetic permeability in ferromagnetic bodies', in *Perspectives in Theoretical Physics*, Elsevier, 1992, pp. 51–65. DOI: 10.1016/B978-0-08-036364-6.50008-9. [Online]. Available: http://dx.doi.org/10.1016/B978-0-08-036364-6.50008-9%20https://linkinghub.elsevier.com/retrieve/pii/B9780080363646500089.

[13] D. Wei, *Micromagnetics and recording materials*. Springer, 2012, p. 110, ISBN: 3642285767.

[14] E. Stoner and E. Wohlfarth, 'A mechanism of magnetic hysteresis in heterogeneous alloys', *IEEE Transactions on Magnetics*, vol. 27, no. 4, pp. 3475–3518, Jul. 1991, ISSN: 0018-9464. DOI: 10.1109/TMAG.1991.1183750. [Online]. Available: http://ieeexplore.ieee.org/document/1183750/.

[15] B. Schmitz, J. Köszegi, K. Alomari, O. Kugeler and J. Knobloch, 'Magnetometric mapping of superconducting RF cavities', *Review of Scientific Instruments*, vol. 89, no. 5, pp. 1–16, 2018, ISSN: 10897623. DOI: 10.1063/1.5030509. arXiv: arXiv:1804.03445v1.

[16] Texas Instruments, *INA163 Low-Noise, Low-Distortion Instrumentation Amplifier*, 2005. [Online]. Available: http://www.ti.com/lit/ds/symlink/ina163.pdf.

Chapter 5

Summary and future work

To complete the dissertation, this chapter proposes a list of possible topics and ideas to be investigated in the future, within the framework of the Anser EMT project.

Electromagnetic tracking and navigation is a promising technology for the future of image-guided interventions, but many challenges need to be solved before obtaining stable and reliable tool tracking. In the future, Anser EMT project will try to solve some of these problems.

The thesis ends with a final summary of the work performed and comments on the results achieved.

5.1 Proposals for future work

5.1.1 Six degree of freedom sensor

The magnetic flux through a classical coil sensor depends on the sensor position (x, y, z) and on the sensor orientation in terms of *pitch* angle θ and *yaw* angle φ. It does not depend on the *roll* angle ψ. See Figure 5.1 for reference. Thus, single coil sensors are five degree of freedom (5DOF) sensors.

In many medical applications it is important to know the roll angle of the instrument. For example, in the scenario of a tracking system used in conjunction to a endoscopic camera, it is useful to know the rotation of the image received.

A six degree of freedom (6DOF) sensor can be obtained with the addition of asymmetry on the coil, so that the magnetic field lines linked by the sensor will change when rotating the sensor around its axis.

The most common solution is the use of an oblique winding, as shown in Figure 5.2. In this configuration the unit vector normal to the winding $\mathbf{n_w}$ does not coincide with the direction vector $\mathbf{n}$ of the coil. The magnetic flux through the coil depends on the magnetic field perpendicular to the winding, proportional to the product $\mathbf{B} \cdot \mathbf{n_w}$. A rotation about the n-axis changes the direction of $\mathbf{n_w}$, which is then a function of θ, φ and ψ. It has to be noted that at least two evaluation points are needed, as shown in Figure 5.2c. Otherwise, a rotation about the n_w-axis does not change the modelled magnetic flux and the orientation of the sensor about the direction $\mathbf{n_w}$ becomes unknown.

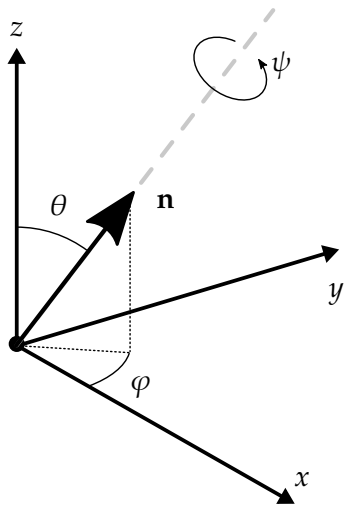

Figure 5.1: Definition of the pose angles: θ is the *pitch* angle, φ is the *yaw* angle and ψ is the *roll* angle.

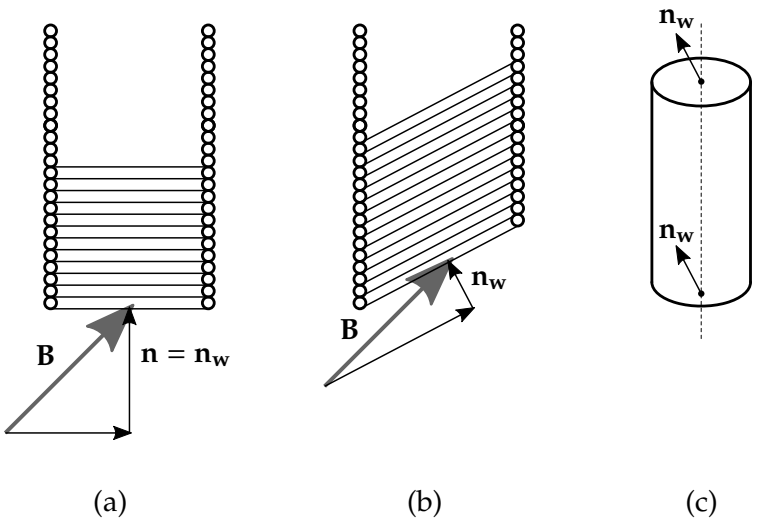

Figure 5.2: (a) In a classical 5DOF sensor the direction of the winding $\mathbf{n_w}$ coincides with the direction of the coil $\mathbf{n}$. (b) An oblique winding provides a displacement between $\mathbf{n_w}$ and $\mathbf{n}$, so a rotation around $\mathbf{n}$ will change the magnetic flux. (c) The model must consider at least two collocation points, otherwise a rotation around $\mathbf{n_w}$ will not affect the modelled magnetic flux.

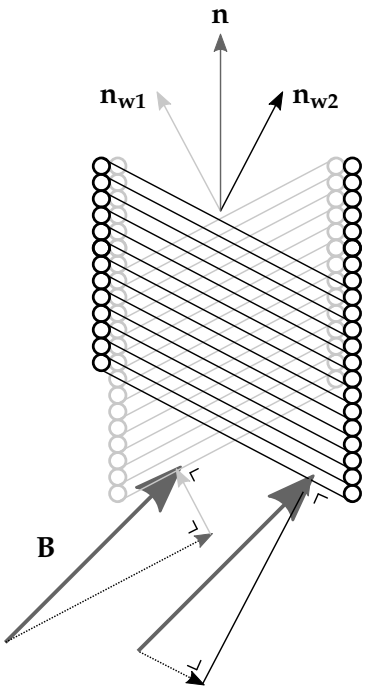

Figure 5.3: Two obliquely-wound concentric coils provide an accurate measurement of the roll angle. The main drawbacks are the need of two channels for the signals and the difficulties that arise from the more complex geometry.

An improvement of the oblique winding method makes use of two obliquely-wound concentric coils, as shown in Figure 5.3. $\mathbf{n_{w1}}$ and $\mathbf{n_{w2}}$ are the unit vectors normal to the two windings. The sum of the two voltage signals gives the contribution due to the magnetic flux parallel to the sensor, while the difference is related to the perpendicular component. In this case, the single point approximation of the sensor can be used, because a rotation around $\mathbf{n_{w1}}$ will change the direction of $\mathbf{n_{w2}}$ and vice versa. The roll angle is identified by the perpendicular direction of the cross product $\mathbf{n_{w1}} \times \mathbf{n_{w2}}$.

The resolution of roll angle can be obtained also by the combination of two classical coils with an angular displacement between their orientation vectors $\mathbf{n_1}$ and $\mathbf{n_2}$. Many commercial 6DOF sensors rely on this method, such as Aurora Mini and Aurora Micro 6DOF sensors (*Northern Digital Inc., Waterloo, Canada*). If compared to the solution with two oblique windings, the use of two coils increases the sensor diameter, but simplifies the manufacturing process. In both the methods, the sensitivity to the roll rotation is increased if the displacement is larger, leading to more manufacturing difficulties in the first case and to a larger sensor diameter in the second case.

Fully working 6DOF sensors have already been tested and implemented in the Anser EMT system. At the moment, all 6DOF sensors need two signal channels, both in the case of two obliquely-wound windings and in the case of two different coils. The position and orientation of the two 5DOF coils inside the sensor are solved independently and the information is used to find the sixth degree of freedom. The main ideas to be investigated in the future are:

- Implementation of a single obliquely-wound coil 6DOF sensor, for which only one

signal channel is needed.

- Realisation of double-winding/double-coil 6DOF sensors where the two signals are summed together and transmitted through the same channel. Implementation of a method to distinguish the signal related to each winding/coil.

- If two channels are used, there is no need to completely solve the position and orientation for each of the two 5DOF coils inside the sensor. Two independent directions give a set of 16 independent equations if eight field generators are used. Then, it is possible to halve the number of emitting frequencies, as well as to allocate four frequencies to each coil, accurately tuned to that frequency range. A narrower bandwidth yields a decreased noise and an increased signal-to-noise ratio (SNR).

5.1.2 Numerical improvements for larger area sensors

In paragraph 1.3.3, the case of tracking coil sensors with small area have been discussed. Using the point-based approximation, the voltage signal v_s of the sensor is related to the magnetic field $\mathbf{B}$ by Equation 1.20:

$$v_s(t) = -N \frac{d\mathbf{B}}{dt} \cdot \mathbf{n}\, A_c \tag{5.1}$$

with N number of turns, A_c sensor area and $\mathbf{n}$ sensor orientation. The position provided by the solver is assumed to indicate the axis of the sensor. The error recorded is at maximum as large as the coil radius, because the magnetic field varies over the area of the sensor and, as stated by the mean value theorem, the average value is equal to the field evaluated at a position inside the integration domain. The same consideration is true for the longitudinal direction, where the maximum error recorded on the longitudinal position of the tracking sensor is equal to half of the coil length.

Larger coil sensor can provide increased sensitivity, as demonstrated in chapter 3, but have decreased accuracy if a point-based approximation is used. Instead, the more general integral of Equation 5.2 may be considered:

$$v_s(t) = -\frac{d}{dt} \frac{N}{l_c} \int_{l_c} \oint_{A_c} \mathbf{B} \cdot \mathbf{n}\, dA\, dl \tag{5.2}$$

where l_c is the length of the coil.

Two numerical procedures which could improve the mathematical model and the computational time are here considered.

Numerical integration over the sensor area

At present, the MATLAB code of the position and orientation solver of Anser EMT approximates the integral of Equation 5.2 by a sum of elements. The area A_c is discretised in a number n of equal area square elements and the field at the centre of every element is considered. A stylised diagram of the procedure is shown in Figure 5.4. Every point is

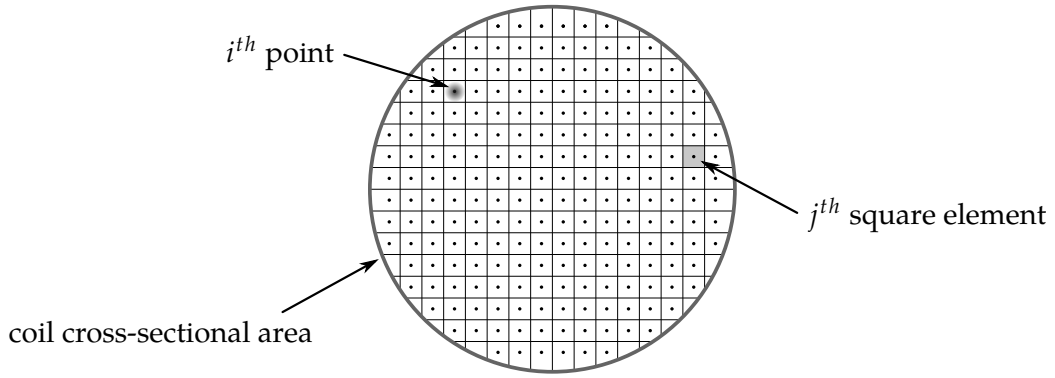

Figure 5.4: For large area sensors the variation of the magnetic flux density may be considered. At present, the code solves the integral of Equation 5.2 by discretising the area in n equal elements and by evaluating the field at the centre of each element.

equally weighted in the sum. The point-based approximation is a particular case of this method, where the area has only one element.

The voltage v_{si} due to the magnetic flux through the i^{th} element of the area is:

$$v_{si} \propto \mathbf{B}(x_i, y_i, z_i) \cdot \mathbf{n}(\theta, \varphi) \tag{5.3}$$

where (x_i, y_i, z_i) indicates the centre of the element and $\mathbf{B}$ is considered constant within the small area of the element. All the elements are coplanar and therefore are characterised by the same orientation unit vector $\mathbf{n}(\theta, \varphi)$.

The total voltage induced on the coil is given by the sum:

$$v_s = \sum_{i=1}^{n} v_{si}(x_i, y_i, z_i, \theta, \varphi) = f(x, y, z, \theta, \varphi) \tag{5.4}$$

The position (x_i, y_i, z_i) of each element is known with respect to the centre of the coil (x, y, z), so the final function is dependent on the five unknowns $(x, y, z, \theta, \varphi)$.

The solver algorithm is the same as that described in paragraph 1.3.6, which consists of a least-square minimisation with 5 unknowns and 8 constraints. However, in this case each of the 8 function needs the evaluation of the magnetic field at n different points. The field is calculated by the filamentary model formula of Equation 1.17.

The future work will seek to find and demonstrate the optimal way to place and weight n points inside the coil cross section. At this purpose, quadrature techniques, such as Gaussian quadrature [1][2], will be evaluated for the circular geometry of the sensor and for the specific space-varying magnetic field.

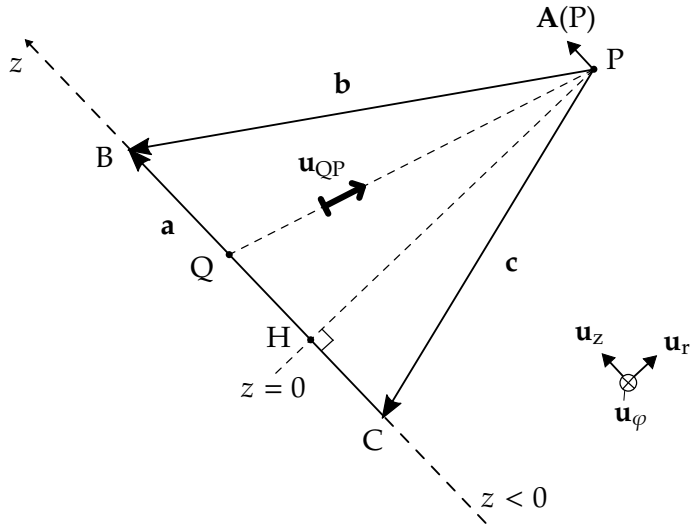

Figure 5.5: Magnetic vector potential **A** due to a straight filament.

Use of Magnetic Vector Potential approach

A novel approach to calculate the flux through a finite-area coil sensor can be used to decrease the number of elements needed to mesh the area of the coil.

The magnetic vector potential **A** is defined as:

$$\mathbf{B} = \nabla \times \mathbf{A} \tag{5.5}$$

Equation 5.5 specifies **A** except for the gradient of an arbitrary function ∇f, that may be fixed by a gauge condition.

For the Stoke's theorem, the magnetic flux through the area S of a loop can be expressed as the closed path integral of **A** along the boundary l of the loop:

$$\Phi = \int_S \mathbf{B} \cdot \mathbf{n}\, dS = \int_S \nabla \times \mathbf{A} \cdot \mathbf{n}\, dS = \oint_l \mathbf{A} \cdot \mathbf{u}_\mathrm{t}\, dl \tag{5.6}$$

with **n** unit vector normal to the infinitesimal surface dS and $\mathbf{u}_\mathrm{t}$ unit vector tangential to dl. When the area of the loop increases, the expression of the flux on the right-hand side of Equation 5.6 becomes computationally more convenient than the classical expression, since it is a line integral, while the classical formulation is a surface integral.

In paragraph 1.3.2 the field generated by a straight filament of current was analytically calculated. The magnetic vector potential **A** at a generic point P of the space is described by the Biot-Savart law for **A**, given by Equation 5.7:

$$\mathbf{A}(\mathrm{P}) = \frac{\mu_0}{4\pi} \int_{\mathrm{Q}\in\Gamma} \frac{I\, \mathbf{u}_t}{\overline{\mathrm{QP}}}\, dl \tag{5.7}$$

When the current path Γ is a segment CB, the integral of Equation 5.7 can be solved [3, Chap. 2]. With reference to Figure 5.5, the direction of the filament is $\mathbf{u}_z$, H is the projection of P on Γ and z is the integration variable, which moves from $-\overline{\mathrm{HC}}$ to $+\overline{\mathrm{HB}}$.

Then **A** has only a z-component and its value is:

$$A_z(\mathrm{P}) = \frac{\mu_0 I}{4\pi} \int_{z=-\overline{\mathrm{HC}}}^{z=+\overline{\mathrm{HB}}} \frac{1}{\sqrt{\overline{\mathrm{PH}}^2 + z^2}}\, dl \tag{5.8}$$

$$= \frac{\mu_0 I}{4\pi} \left[\log\left(z + \sqrt{\overline{\mathrm{PH}}^2 + z^2} \right) \right]_{z=-\overline{\mathrm{HC}}}^{z=+\overline{\mathrm{HB}}} \tag{5.9}$$

$$= \frac{\mu_0 I}{4\pi} \left[\log\left(\overline{\mathrm{HB}} + \overline{\mathrm{PB}} \right) - \log\left(-\overline{\mathrm{HC}} + \overline{\mathrm{PC}} \right) \right] \tag{5.10}$$

$$= \frac{\mu_0 I}{4\pi} \left[\log\left(\frac{\mathbf{a}\cdot\mathbf{b}}{|\mathbf{a}|} + |\mathbf{b}| \right) - \log\left(\frac{\mathbf{a}\cdot\mathbf{c}}{|\mathbf{a}|} + |\mathbf{c}| \right) \right] \tag{5.11}$$

where Equation 5.8 has a known solution [4, integral 200.01].

5.1.3 Sensor fusion

Positional tracking can take advantage of the use of multiple sensors and tracking algorithms. For example, it is possible to combine inertial tracking with magnetic tracking, to get a more accurate and more precise result [5][6]. Inertial tracking uses the data from accelerometers and gyroscopes. Starting from an initial state, the integration of the linear and the angular accelerations allows to obtain the final position and orientation.

The use of a Kalman filter to combine the information coming from the accelerometer and the magnetic sensor could substantially improve the performances of the tracking procedure. The basic idea behind a Kalman filter is expressed by Figure 5.6, where the estimation of a certain parameter p is given by two different methods, for example with an accelerometer (p_a) and with a magnetic sensor (p_m). Each measurement comes with uncertainty, *i.e.* a normal probability distribution with variance σ around the expected value. The role of the Kalman filter is to combine both the data to obtain a new estimation p_f of the parameter with a reduced uncertainty, stated by a smaller variance σ_f. In the case of a tracking system, the parameters that define the pose of the sensor are five (or six for a 6DOF sensor).

Another benefit of the presence of an accelerometer is the possibility to compute the instant velocity of the tracking sensor. The motion of a coil inside a magnetic field adds a motional component to the electromotive force. If the velocity is known, the model can take this into consideration and compensate the motional effect, to correctly isolate the transformer component, which is related to the time variation of the magnetic flux.

Finally, an additional reference for the sensor position could help to perform the calibration procedure and to compensate errors caused by magnetic field distortion, due to the medical instrument or to the presence of conductive materials within the field of operation.

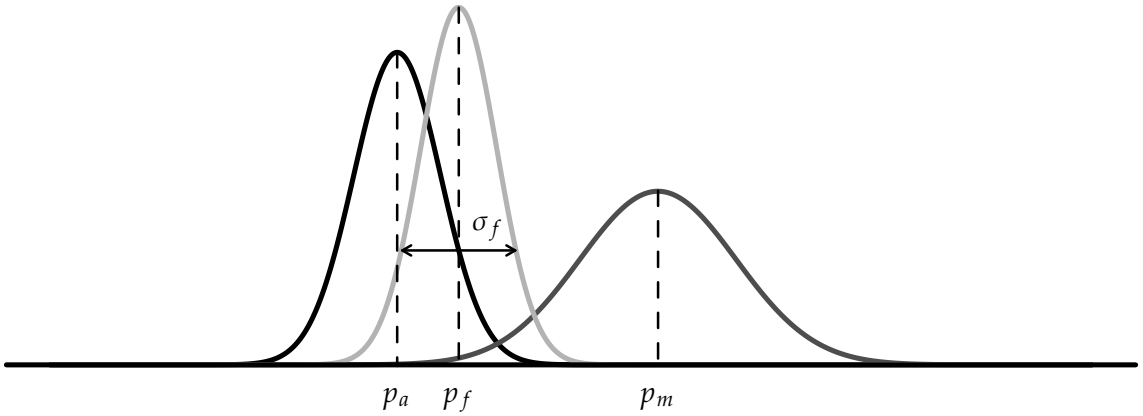

Figure 5.6: Simplified concept behind a Kalman filter. The accelerometer and the magnetic sensor provide two estimations of the parameter p: p_a and p_m. The fusion of the two data provides a new estimation p_f with a smaller variance σ_f.

5.1.4 Integrated circuit inductive sensor

Wound inductive coil sensors are physically limited by manufacturing technology, which cannot build coils smaller than a certain limit. Commercially available inductive sensors have a minimum diameter of 0.5 mm [7].

The realisation of an integrated circuit planar coil would bring benefits in terms of sensor dimensions and production costs. The reduction of the coil cross-sectional area will certainly decrease the sensitivity of the sensor, which can be partially recovered by increasing the number of turns with high density packing. Semiconductor technology allows the integration of analogue filters and signal amplifiers directly in the sensor integrated circuit [8].

5.1.5 Adaptive field generator

Many improvements of the field generator can be investigated, some regarding the nature of the magnetic field transmitted and others with respect to the physical geometry of the transmitting board.

A first problem which should be addressed is the regulation of the field intensity depending on the position of the tracking sensor. When the sensor is closer to the emitter coil, the induced signal is larger, so that the amplitude of the exciting field could be decreased without much impact on tracking accuracy. This yields a reduced power consumption and the reduction of non-linearities of the ferromagnetic core, if present, which arise when it is subject to a strong electromagnetic field. When the sensor moves further, the amplitude of the field will be modulated consequently, to always assure a strong signal.

Another possible research area is the intelligent selection of field generator frequencies based on the environment, to reduce field distortions. Typical distorters are ferromagnetic materials, which affect the spacial distribution of the magnetic field, and conductive materials, which cause induced eddy currents. Lower frequencies are appropriate to decrease eddy current effects.

At present, the generator board is planar and this can affect the field volume coverage. More ergonomic shapes should be considered, with focus on the optimum 3D array of the emitter coils to obtain a strong and highly space-variable field.

A novel idea is the realisation of a flexible substrate field generator. The eight emitter coils could be inserted in a pillow which adapts to any surface and to the body of the patient. The relative position of the coils can be obtained through the measurement of mutual inductances. In other words, each coil acts as a tracking sensor in the field generated by the other seven. The presence of different frequency components from each emitter leads to the voltage induced by the other coils. For this purpose, since the coils have large area and are composed of approximately straight-filament conductors, Equation 5.11 demonstrated in section 5.1.2 may prove useful.

5.1.6 Simplified calibration

Due to the variability of the operational environment, such as the temperature and the presence of field distorters, EMT systems require calibration in situ before use. At moment, the calibration process involves the pose of the tracking sensor at 49 test-points of known position, as described in paragraph 1.3.5. The whole procedure takes about 3 minutes and the sensor needs to be inserted in a calibration probe. Many commercial medical instruments, such as endoscopes or needles, have embedded sensors which cannot be parted from their parent structure. A more fast and flexible calibration routine may be developed.

A common method used to calibrate an EMT system is the adoption of a secondary tracking system. Optical tracking systems provide an absolute reference to the position of the sensor, in the place of known position test-points, as demonstrated in [9]. If developed, the inertial tracking system proposed in paragraph 5.1.3 could be used as well. Care must be taken to assure that the two (or more) tracking systems are synchronised. A delay in the position would give a wrong reference position.

A novel calibration technique may involve the use of machine learning, trained with data of previously calibrated sensors. A random set of points may give enough information to resolve the system calibration coefficients. Moreover, machine learning could be able to predict the sensor position without solving the magnetic field model. Each point in the tracked volume is characterised by a specific value of the magnetic field. If this data is previously registered and saved, the measurement of the sensor can be used as a *keyword* to look for the corresponding position inside the database. More complex geometries for the emitter coils can be adopted, since with this method there is no need to model and analytically know the magnetic field in the space. The feasibility of this possibility is to be demonstrated.

5.2 Conclusions

To summarise, the thesis focused on the research of new solutions for magnetic sensors for use in electromagnetic tracking (EMT).

The work started with an overview study of image-guided interventions and of EMT principles and commercial systems. In this context, the open-source Anser EMT project was deeper analysed and the operation of its main subsystems was understood.

The theory of Helmholtz coils was reviewed and electromagnetic simulations were performed in order to design and realise a custom Helmholtz coil. This instrument was subsequently used to generate the homogeneous magnetic field needed for the characterisation of magnetic sensors.

Large-area inductive coils were investigated and compared to commercial solutions. Experimental results demonstrated the correctness of the approach, based on simple theoretical calculations. This study provided useful methodologies for the design, optimisation and implementation of air-core and ferrite-core inductive sensors.

A general study of xMR sensors was followed by investigation of the possible integration of this kind of sensors in 3D tracking systems. Experimental work consisted in the construction of a circuit to make an AMR sensor work more efficiently and in the characterisation of the sensor. Results demonstrated the constant sensitivity expected. Unexpected phase shift and signal amplification were observed at higher frequencies, although these high frequency effects are of limited interest for Anser EMT.

Finally, open problems to be considered in future work were presented and innovative ideas were proposed. Electromagnetic for tracking and navigation is a promising technology for the improvement of image-guided interventions of the future and research on this field is still in progress.

Bibliography

[1] H. Kabir and S. A. H. H. Matikolaei, 'Implementing an Accurate Generalized Gaussian Quadrature Solution to Find the Elastic Field in a Homogeneous Anisotropic Media', *Journal of the Serbian Society for Computational Mechanics*, vol. 11, no. 1, pp. 11–19, Dec. 2017, ISSN: 18206530. DOI: 10.24874/jsscm.2017.11.01.02. [Online]. Available: http://www.sscm.kg.ac.rs/jsscm/index.php/volume-11-number-1-2017/180-paper-02-2017-1.

[2] L. Daruis, P. González-Vera and F. Marcellán, 'Gaussian quadrature formulae on the unit circle', *Journal of Computational and Applied Mathematics*, vol. 140, no. 1-2, pp. 159–183, Mar. 2002, ISSN: 03770427. DOI: 10.1016/S0377-0427(01)00410-1. [Online]. Available: https://linkinghub.elsevier.com/retrieve/pii/S0377042701004101.

[3] C. R. Paul, *Inductance*. Hoboken, NJ, USA: John Wiley & Sons, Inc., Dec. 2009, pp. 1–379, ISBN: 9780470561232. DOI: 10.1002/9780470561232. [Online]. Available: http://doi.wiley.com/10.1002/9780470561232.

[4] H. B. Dwight, 'Tables of Integrals and Other Mathematical Data.', *The Macmillan Company*, 1957, ISSN: 00063444. DOI: 10.2307/2333782. [Online]. Available: https://www.jstor.org/stable/2333782?origin=crossref.

[5] A. M. Franz, T. Haidegger, W. Birkfellner, K. Cleary, T. M. Peters and L. Maier-Hein, 'Electromagnetic Tracking in Medicine—A Review of Technology, Validation, and Applications', *IEEE Transactions on Medical Imaging*, vol. 33, no. 8, pp. 1702–1725, Aug. 2014, ISSN: 0278-0062. DOI: 10.1109/TMI.2014.2321777. [Online]. Available: http://ieeexplore.ieee.org/document/6810177/.

[6] A. Vaccarella, E. De Momi, A. Enquobahrie and G. Ferrigno, 'Unscented Kalman Filter Based Sensor Fusion for Robust Optical and Electromagnetic Tracking in Surgical Navigation', *IEEE Transactions on Instrumentation and Measurement*, vol. 62, no. 7, pp. 2067–2081, Jul. 2013, ISSN: 0018-9456. DOI: 10.1109/TIM.2013.2248304. [Online]. Available: https://ieeexplore.ieee.org/document/6481446.

[7] Northern Digital Inc., *Aurora 5DOF Sensor 0.5 mm x 8 mm, Part Number: 610099*. [Online]. Available: https://www.ndigital.com/medical/products/tools-and-sensors/.

[8] R. J. Baker, *CMOS: Circuit Design, Layout, and Simulation: Third Edition*. 2011, ISBN: 9780470881323. DOI: 10.1002/9780470891179.

[9] A. J. Chung, P. J. Edwards, F. Deligianni and G.-Z. Yang, 'Freehand Cocalibration of Optical and Electromagnetic Trackers for Navigated Bronchoscopy', in, 2004, pp. 320–328. DOI: 10.1007/978-3-540-28626-4_39. [Online]. Available: http://link.springer.com/10.1007/978-3-540-28626-4_39.